Modelling of Organic Thin Film Transistors incorporating Liquid Crystalline Metal Phthalocyanines

Tsegie Faris

Supervised by

Dr. George Fern

Prof. Chris Winscom

Department of Materials Processing

Wolfson Centre

Brunel University

Uxbridge, UK

April 5 2018

I

I

ACKNOWLEDGEMENTS

ABSTRACT

The aim of this project has been to characterise spin-coated "as-deposited" and annealed films of liquid crystalline mono- and bis metal phthalocyanines acting as p-type semiconductors in OTFT devices. Structural variations such as long-chain alkyl substituents at peripheral and non-peripheral positions, and aza nitrogen replacement, have been considered. The main quantity for this characterisation is the field-independent mobility of the organic semiconductor material.

The method by which this has been achieved involves extracting fundamental device parameters of the OTFT from experimental current-voltage (I-V data). An existing analytical model has been modified to describe charge transport of OTFT devices. In addition, source and drain contact resistances exhibiting possible Schottky behaviour, and bulk bypass resistance effects have been accounted for. A statistical modelling procedure, which simulated the experimental I-V data according to the defined model, has then been used to extract all the device parameters simultaneously,

The field-independent mobility is the key characteristic that has been measured. In substituted copper phthalocyanines this mobility increases from $3.91{\times}10^{-3} cm^2V^{-1}s^{-1}$ to $4.89{\times}10^{-3}$ $cm^2V^{-1}s^{-1}$ when an aza-N atom is replaced by CH. Also, the mobility of an as-deposited film of copper phthalocyanine with a short-chain alkyl substituent is found to be higher by two orders of magnitude compared with that having a long-chain alkyl substituent. Similarly, the mobility is lower for an as-deposited film of zinc phthalocyanine having substituents at non-peripheral positions compared with substituents at peripheral positions. In lead phthalocyanine the mobility for an as-deposited film is found to be $7.56{\times}10^{-4}cm^2V^{-1}s^{-1}$. This value increases significantly to $4.19{\times}10^{-2}cm^2V^{-1}s^{-1}$ as the film is annealed at 150 °C, where an improved film morphology with a lower number of grain boundaries is believed to occur. In general, the mobility of a bis-gadolinium phthalocyanine film is found to be smaller compared with all the mono-metal phthalocyanines examined so far.

LIST OF SYMBOLS

DC	direct current
DOS	density of states
dY	an element of the depth
D	Denominator
C_{ox}	capacitance per unit gate area
E	electric field
E_{cb}	conduction band level
E_{fm}	metal energy of the Fermi level
E_{fs}	semiconductor equilibrium Fermi energy level
E_{vb}	valence band energy level
E_i	intrinsic semiconductor Fermi energy level
E_F	Fermi energy level
L	channel length
J	current density
I_{ch}	current in the accumulation channel
I_0	current in an element of bulk having the same dimension as the accumulation channel
I_{DS}	drain to source current
μ_o $(cm^2\,V^{-1}s^{-1})$	field Independent mobility
μ $(cm^2\,V^{-1}s^{-1})$	electron mobility
μ_n $(cm^2\,V^{-1}s^{-1})$	electron mobility for crystalline semiconductor the mobility
μ_{eff} $(cm^2\,V^{-1}s^{-1})$	field dependent mobility
Y	material fitting parameters
k_B	Boltzmann constant
K	material parameter constant
K'	slope for equation (3.2.34)
M	material fitting parameter
MNE (meV)	Meyer–Neldel energy

N'(E)	no. of carriers that can contribute to current
N'(0)	density of localized states
n	total charge carrier concentration that contributes to the current flow
n_i	intrinsic carrier concentration
N_c	an effective density of states
F	an applied electric field
n_o	the free charge carrier density
n	the charge carrier concentration
$R_x(\Omega)$	Resistance
$R_o(\Omega)$	Resistance
$R_n(\Omega)$	resistance at Maximum
$R_D(\Omega)$	contact Resistance at Drain
$R_S(\Omega)$	contact Resistance at Source
$R_{ch}(\Omega)$	channel resistance
$R_B(\Omega)$	bulk resistance
V_T (V)	threshold Voltage
VB	valence band
V_{GT}	gate voltage - threshold voltage
V_{DS} (V)	drain to source voltage
V_D (V)	drain voltage
V_{GS} (V)	gate to source voltage
V_G (V)	gate voltage
W	channel width
Z	Depth
q	carrier charge
Q_o	Charge
Φ_o	the potential just beyond the accumulation region
Φ_s	the potential at the dielectric-semiconductor interface

Δ	the extent along the y-axis of the accumulation region
Δ	Delta
v_y	drift velocity
I_y	current flow in the y-direction
Dy	small element in the gate region
ε_o	permittivity of vacuum
ε_r	relative permittivity of dielectric constant of the substance

ABBREVIATIONS

N_D	nematic-discotic mesophase
N_{Col}	nematic-columnar mesophase
Col_h	columnar hexagonal mesophase
Col_r	columnar rectangular mesophase
LUMO	lowest unoccupied molecular orbital
HOMO	highest occupied molecular orbital
ZnPcR4	zinc phthalocyanines substituted at peripheral positions
6CuPc	copper phthalocyanines substituted at peripheral positions
6CuTBTAP	copper triazaporphyrins substituted at peripheral positions
10CuPc	copper phthalocyanines substituted at peripheral positions
10CuTBTAP	copper triazaporphyrins substituted at peripheral positions
MPc	metal phthalocyanines
ZnPc	unsubstituted zinc phthalocyanines
PbPc	unsubstituted lead phthalocyanines
C6PbPc	substituted lead phthalocyanines
$GdPc_2R_{16}$	gadolinium phthalocyanine
P-MOS	p-channel metal-oxide semiconductor
n-MOS	n-channel metal-oxide semiconductor
VRH	variable-range-hopping
MTR	multiple-trap-and-release
TFT	thin film transistor
OTFT	organic thin film transistor
SiO_2	silicon dioxide
MOSFET	metal-oxide-semiconductor field-effect transistor
MOS	metal-oxide-semiconductor
FET	field effect transistor
BJT	bipolar junction transistors
MIS	metal-insulator-semiconductor

x

1.   INTRODUCTION

Organic thin film transistor (OTFT) devices are becoming a sustainable piece of technology due to their low cost and large area electronic application; however physical and chemical behaviour issues which define the charge transport mechanism have not yet been resolved; ambiguities still exist.

In the late 20th century, OTFTs started to be fabricated using newly synthesised organic semiconductor materials with the help of modern techniques. Significant progress was achieved by replacing silicon based inorganic semiconductors with organic semiconductor materials. In the last few years the performance of OTFTs has gradually improved and their fundamental device parameter values approach those obtained from hydrogenated amorphous silicon devices [1, 2].

The general electrical behaviour of OTFTs strongly depends on the organic semiconductor (small molecule or polymer) active layer and its charge carrier concentration. Molecular stacking, where the conjugated π-electrons can interact between pairs of adjacent molecules, also influences the charge carrier transfer.

Recently, the performance of individual OTFTs has been shown to be comparable with amorphous silicon thin-film transistor counterparts; p-type base OTFTs involving polymer semiconductors have a leading hole field-effect mobility up to 43 $cm^2 V^{-1}s^{-1}$ [3] and for small molecule organic semiconductors, 3.16 $cm^2 V^{-1}s^{-1}$ [4]. Thin films of an active layer of well-aligned substituted triphenylenes, exhibiting columnar mesomorphism, were shown to have a charge carrier mobility of 1×10^{-5} $cm^2 V^{-1}s^{-1}$ [5]. These materials are similar in their stacking characteristics to the metallopthalocyanine class, which is that studied in this thesis.

One of the causes of lower mobility in OTFTs is the presence of line defects, either in the channel at the oxide / organic semiconductor interface, or in the bulk, near this channel. Such line defects at the grain boundaries in the channel region cause the active layer of the device to degrade, where the source of trap states is believed to reside. In addition to this, OTFTs are sensitive to ambient atmospheric conditions; the mobility becomes lower when the organic semiconductor absorbs water and oxygen from the environment [5]. However, such electrical properties can be enhanced by minimizing the number of the grain boundaries and by increasing the surface smoothness. Surface smoothness can be achieved via heat treatment which enhances the grain size of the material [5-7].

Large grain sizes hinder the diffusion of water and oxygen into the active channel. The mobility in the highly ordered crystal growth on the OTFT active layer surface increases as the grain boundary ratio decreases [7&8]. According to Breeze et al. [9], comparing an annealed with a non-annealed polymer layer film shows that the current density doubles and the average mobility increases by a half [9].

Various techniques and methods have been proposed for manufacturing OTFT devices. The most important consideration in maximising device efficiency is the method of synthesis of the organic semiconductor. Extra precautions during synthesis which reduce any related defects and other

unwanted impurities are a primary factor in achieving this goal. Another consideration is that film deposition in an open environment using a spin coater leads to the production of a non-uniform film of varying thickness. Furthermore, unwanted cracks in a film can occur during cooling when an annealed film is not allowed to cool gradually to lower temperatures, before taking electrical measurements. All of these effects are sources of structural irregularity in device materials, and will impede the flow of charge carriers which in turn will have an impact on the OTFT performance. Additional care is also needed during electrical measurements taking place in an open environment. Also, equipment settings must provide adequate digitisation of the experimental data to prevent distortion of the data being recorded.

The DC performance of an OTFT device is characterised by source to drain current (I) – voltage (V) curve, where linear and saturation regions are displayed. Analytical models are used to simulate the experimental I-V data obtained from OTFT devices; the extracted parameters from such models can be related to material characteristics, e.g. electrical mobility.

There are a large number of analytical models that have been proposed for OTFT devices. The initial assumptions of each model have similarities and most OTFT analytical models follow hypotheses describing the transport of charge carriers. This transport is governed by so-called multiple-trap-and-release (MTR) or variable-range-hopping (VRH) mechanisms. However, agreement on a consistent model has yet to be reached. Furthermore, agreement on how to apply modelling to all OTFT devices regardless of device geometry, and other device aspects, is needed. An important purpose of an analytical model is that it can be used as a simulator to provide a cost effective method to predict the performance of a device and allow its optimisation.

A MOSFET model - the so-called SPICE model [10] - is globally accepted, and used extensively for both academic and industrial purposes. It will be described in more detail in Chapter 2. One definition of this model, AIM-SPICE level 15 or 16 [10], is mostly used for OTFT simulation. However, these models require a high number of parameters. So-called "Accurate" models [11-14], are models developed for hydrogenated amorphous silicon transistors with channel lengths as small as 4μm and these models provide a method for parameter extraction. Unfortunately, the extracted values provide a poor fit, so that trial-and-error refinement is necessary to obtain final set parameters which fit acceptably. The parameters of these "accurate" models can be correlated with some of the input parameters that are required by AIM-SPICE level 15 or 16 model for device simulation. The disadvantage of this model is that it uses a large number of parameters, some of which are adjustment parameters with no physical meaning. This model does not provide a method to extract the field-independent mobility values from the experimental data. The "accurate" model is used to simulate non-crystalline and crystalline -TFT devices; it is an alternative to AIM-SPICE level 15 or 16 model, but it is not suitable as a statistical model due to the large number of parameters to be extracted.

The TFT generic charge drift / compact [15-18] model requires less parameters than the "accurate" model. This symmetrical model emphasises the voltage drop at the source contact where the contact

resistance is claimed to be higher than at the drain; this is extracted using the experimental data provided by the output curve.

The model of Natali, et al.[19], is a type of analytical model that follows a power law dependence, where the effective mobility depends on gate voltage. The method proposes two methods of extraction to obtain the mobility field-dependence parameter (γ) and threshold voltage (V_T), which involve differentiation of the data curves. The model also proposes two analytical expressions for the linear and saturation regions. One of the disadvantages of this analytical model is that it is applicable to only a small range of Gate-to-Source (V_{GS}) voltage, whilst a large range of V_{GS} cannot be handled. Noisy experimental data are not suitable for differential methods of parameter extraction. Discrepancy between experimental data and the modelled fit is high. In addition, the model ignores all data from the output curve.

The advantage of both TFT generic charge drift / compact model [17-19] and "accurate" models [11,12 and 14] over the Natali model[19], is that these models involve physically monitoring the entire experimental curve from output to transfer characteristics, including both the strong and weak inversion (sub-threshold) region. In contrast, in the Natali model, only a small voltage range is involved and the output characteristics are excluded. Constant drain- and source contact resistances are included in the model equations for both the TFT generic charge drift / compact model and "accurate" models, whereas in the Natali model the contact resistances are not constant and decrease with gate voltage.

In this research these different analytical models have not been overlooked but show some serious drawbacks to obtaining consistent and accurate device parameters. For these reasons it was decided to follow the Raja and Eccleston Model [20] which was clearly presented; the model defines the obvious baseline for describing an OTFT device, using the minimum number of parameters. The Raja and Eccleston Model formed a good starting point to develop a statistical modelling approach in which all parameters are optimised simultaneously.

The fundamental parameters of an analytical model are the field-independent mobility, μ_o, the field-dependent mobility parameter, m, and the characteristic temperature, T_C. These three parameters define the chemical and physical properties of the organic semiconductor active layer that include the morphology, trap states, electrical conductivity and the crystallinity. In this study, the I-V characteristics of OTFT devices, where the organic semiconductor layers were mono- and bis metal-phthalocyanines substituted at peripheral- or non-peripheral positions.

References

[1] Gundlach, D. J., Zhou, L., Nichols, J. A., et al. (2006) 'An experimental study of contact effects in organic thin film transistors' *J. Appl. Phys.*, **100**, **024509**, doi: http://dx.doi.org/10.1063/1.2215132.

[2] Necliudov, P. V., Rumyantsev,S. L., Shur, M. S. Gundlach, D. J., et al. (2000) '1/ f Noise in pentacene organic thin film transistors',*J. Appl. Phys.*,**88(9)**,**5395-5399,** doi: 10.1063/1.1314618.

[3] Yuan, Y., Giri,G., Ayzner, A. L., et al. (2014) 'Ultra-high mobility transparent organic thin film transistors grown by an off-centre spin-coating method' *Nat.Commun*, **5** ,**1**, doi: 10.1038/ncomms4005.

[4] Lim, B., Sun, H., and Noh, Y.-Y. (2017) 'Highly soluble small-molecule organic semiconductor with trihexylsilyloxy side chain for high-performance organic field-effect transistors with mobility of up to 3.10 cm^2 V^{-1} s^{-1} , *Dyes Pigm* ,**142**, **17,** doi: 10.1016/j.dyepig.2017.03.025.

[5] Eichhorn, H. (2000) 'Mesomorphic phthalocyanines,tetraazaporphyrins, porphyrins and triphenylenes as charge-transporting materials',*j. porphyr. phthalocyanines*, **4(1), 88**, doi:10.1002/(SICI)1099-1409(200001/02)4:1<88::AID-JPP208>3.0.CO;2-6.

[6] Jagar, S., Chan, M., Poon, M.C., et al. (1999) 'Single grain thin-film-transistor (TFT) with SOI CMOS performance formed by metal-induced-lateral-crystallization' IEDM doi: 10.1109/IEDM.1999.824154.

[7] Kumaki, D., Yahiro, M., Inoue, Y., and Tokitoa, S. (2007) 'Air stable, high performance pentacene thin-film transistor fabricated on gate insulator treated with–phenethyltrichlorosilane', *Appl. Phys. Lett.*, **9 ,133511**, doi: 10.1063/1.2717552.

[8] Klauk, H., Member, S., Gundlach ,D.J., et al. (1999) 'Pentacene Organic Thin-Film Transistors for Circuit and Display Applications', *IEEE Trans. Electron Dev.*, **46(6)**, **1258**, doi: 10.1109/16.766895.

[9] Breeze, A.J., Schlesinger.Z., Carter. S. A., et al. (2001) 'Charge transport in TiO2/MEH-PPV polymer photovoltaics', *Phys. Rev. B*, **64**, **125205 ,** doi: 10.1103/PhysRevB.64.125205.

[10] AIM-Spice, Circuit Simulation Program by AIMSoftware. (www.aimspice.com).

[11] Cerdeira,A., Estrada,M., Garcia,R., et al. (2001) 'New procedure for the extraction of AIMSpice level 15 a-Si:H TFT model parameters' IPN No. 2508, Apto. Postal 14-740, 07300 DF, México. E-mail: cerdeira@mail.cinvestav.mx.

[12] Cerdeira,A., Estrada,M., Garcia,R., et al. (2001) 'New procedure for the extraction of basic a-Si:H TFT model parameters in the linear and saturation regions ' *Solid-State Electron.*,**45 (7)** , **1077,** doi: 10.1016/S0038-1101(01)00143-5.

[13] Estrada, M., Cerdeira, A., Ortiz-Conde,A., et al. (2002) 'Unified extraction method for amorphous and polycrystalline TFT above threshold model parameters' Fourth IEEE International Caracas Conference on Devices, Circuits and Systems, Aruba, April 17-19, 2002.

[14] Estrada,M., Cerdeira, A., Puigdollers, J., et al. (2005) 'Accurate modeling and parameter extraction method for organic TFTs' *Solid State Electron*, **49**(**6**) ,**1009**, doi:10.1016/j.sse.2005.02.004

[15] Awawdeh, K. M., Tejada, J. A., Varo, López P., et al. (2013) 'Characterization of organic thin film transistors with hysteresis and contact effects' *Org Electron*, **14**(**12**),**3286**, doi: 10.1016/j.orgel.2013.09.034.

[16] Deen,M.J., Marinov, O., et al. (2009) 'Organic Thin-Film Transistors:Part II-Parameter extraction ' *IEEE Trans. Electron Dev.*, **56**(**12**) , **2962**, doi: 10.1109/TED.2009.2033309.

[17] Marinov, O., Deen,M.J., Zschieschang, U.,et al. (2009) 'Organic Thin-Film Transistors:PartI-Compact DC Modeling', *IEEE Trans. Electron Dev.*, **56**(**12**) ,**2952**, doi: 10.1109/TED.2009.2033308.

[18]Tejada, J.A. J., Awawdeh, K.M., Villanueva, J.A. L., et al. (2011) 'Contact effects in compact models of organic thin film transistors: Application to zinc phthalocyanine-based transistors', *OrgElectron.*,**12**(**5**),**832**, doi:10.1016/j.orgel.2011.02.010.

[19]Natali, D., Fumagalli, L., and Sampietro, M. (2007) 'Modeling of organic thin film transistors: Effect of contact resistances', *J. Appl. Phys.* ,**101**(**1**), **014501** ,doi: 10.1063/1.2402349.

[20] Raja,M. and Eccleston,W. (2011) 'Analytical device models for disordered organic Schottky diodes and thin-film transistors for circuit simulations', *IET Circuits, Devices & Systems,* **6**(**2**), **122**,doi: 10.1049/iet-cds.2011.0199.

2.   PHYSICAL INTERPRETATION OF THIN FILM TRANSISTORS

The scope of this chapter is to describe the thin film transistor (TFT) device. It will include a general background, describe the operation of the device, and explain why different mathematical models are needed to extend the interpretation of traditional inorganic TFTs to organic thin film transistors (OTFT's). Finally, recent theoretical approaches that provide a detailed explanation of the dependence of field-effect mobility on gate voltage in OTFT's will be presented.

2.1 The transistor

Transistors are essential modern day semiconductor devices; they are used in microelectronic circuits mainly for amplifying electrical signals and performing switching functions. William Shockley, John Bardeen and Walter Brattain [1] were the first to build a transistor in Bell labs on December 23, 1947. There are two categories of transistor: (i) bipolar junction transistors (BJT's) and (ii) field effect transistors (FET's) [1, 2].

2.2 Field effect transistors

Lilienfeld [3] was the first person to propose the principle of the FET in 1930. However, in 1959 Kahng and Atalla produced the first silicon-based metal-oxide-semiconductor (MOSFET) [4]. In 1962 a TFT based on FET principles was proposed by Weimer and his team for the first time [5]; in the same year they managed to develop polycrystalline inorganic semiconductor based transistors [5]. This idea led to an advance in transistor technology, and in 1980 the first OTFTs were reported [6, 7, 8].

Metal-Oxide-Semiconductor (MOS) capacitor devices and their band diagram are the best tools to understand the FET device. An insulator material, usually silicon dioxide (SiO_2) is used to separate metal (e.g. gold) from an n- or p-type semiconductor. Here, gold was used as the metal electrode and the work function of gold is about 4.83±0.02 eV[9], unfortunately the precise electron affinities of the given MPc semiconductor were not provided. However, the electron affinity of CuPc organic semiconductor is the range between 4.7-5.3 eV [10]. Assuming a pure organic semiconductor then at zero voltage the band diagram shows a flat portion, which means the MOS structure is at the equilibrium point, shown in figure 2.1 [4,11,12].
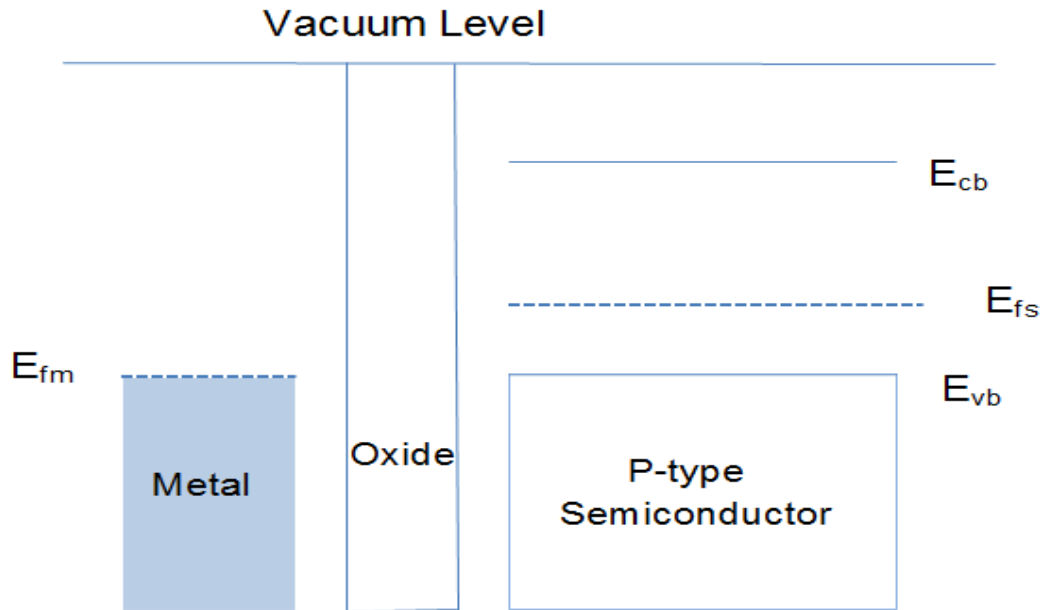
Figure 2.1 A slab of metal, oxide and p-type semiconductor where E_{fs} is the equilibrium Fermi level of p-type semiconductor, E_{cb} the conduction band level and E_{vb} the valence band level. E_{fm} is the energy of the Fermi level for the metal [11,12]. The Fermi level is the energy level of an electron which is held in material with the least tightly bonded within a solid material.

(a)   (b)
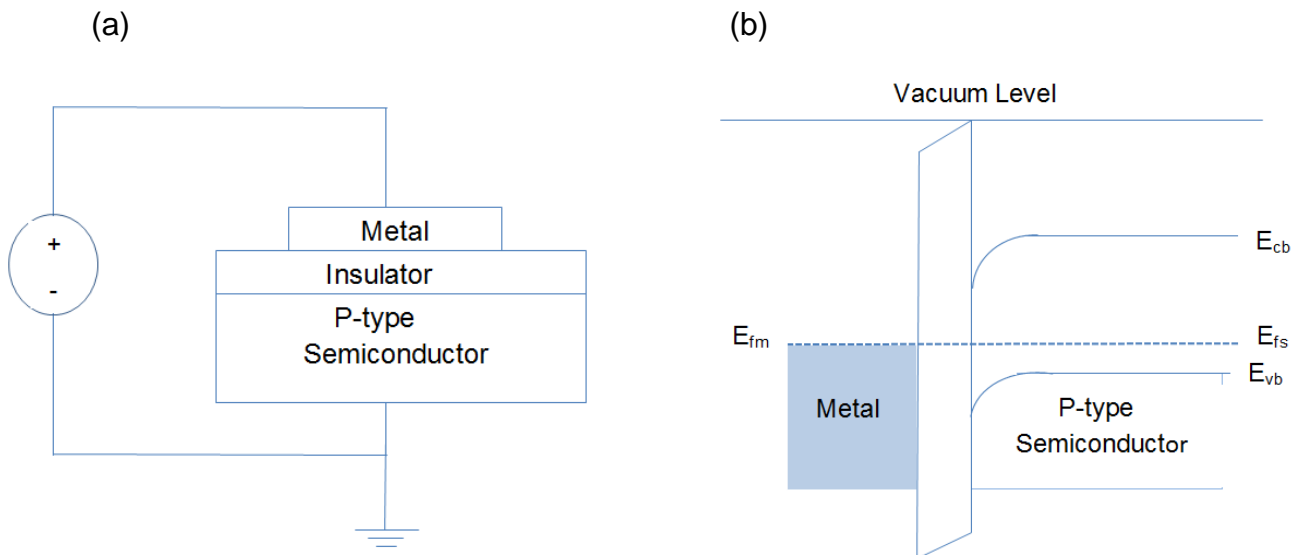
Figure 2.2. (a) The MOS Capacitor and (b) the band diagram at equilibrium, showing the modified work function at the metal-oxide interface and the modified work function at a p-type semiconductor-oxide interface.

As the metal, Oxide and the p-type semiconductor are brought together then the bands are bending down where the holes start to flow near the oxide-semiconductors interface. Since the electron affinity of the MPc organic semiconductor is larger than the gold work function hence, the energy barrier height is formed due to Schottky contact.

Based on an ideal metal-insulator-semiconductor (MIS) diode, figure 2.2.(a), the operation of the MOS capacitor can be explained with the help of a band diagram.

As voltage is applied to the MOS capacitor there will be a surface effect at the insulator-semiconductor interface. This surface effect can be described by a change in the energy-band diagram, with the band-positions bending either upward or downward depending upon the voltage applied and the nature of the channel material (n- or p-type). In many books and published papers the energy band of the insulator-semiconductor interfaces investigated has used n-type channel material whilst applying a negative or positive voltage [11, 12].

2.2.1 Formation of a depletion region

As can be seen in figure 2.3a, holes will deplete at the oxide/p-type semiconductor interface when a positive voltage is applied between the metal and p-type semiconductor. A net negative charge is produced at the surface which corresponds to a positive charge being deposited on the metal.

As a result of the applied positive voltage, the Fermi level of the metal moves up relative to Fermi level of the semiconductor in figure 2.3a, and the oxide conduction band (E_{cb}) bends down near the semiconductor surface with the result that E_i moves closer to E_{fs} at the semiconductor surface. Summarising, a negative charge in the p-type material arises as the hole concentration decreases in the depleted region near the p-type material surface [4, 11, 12].
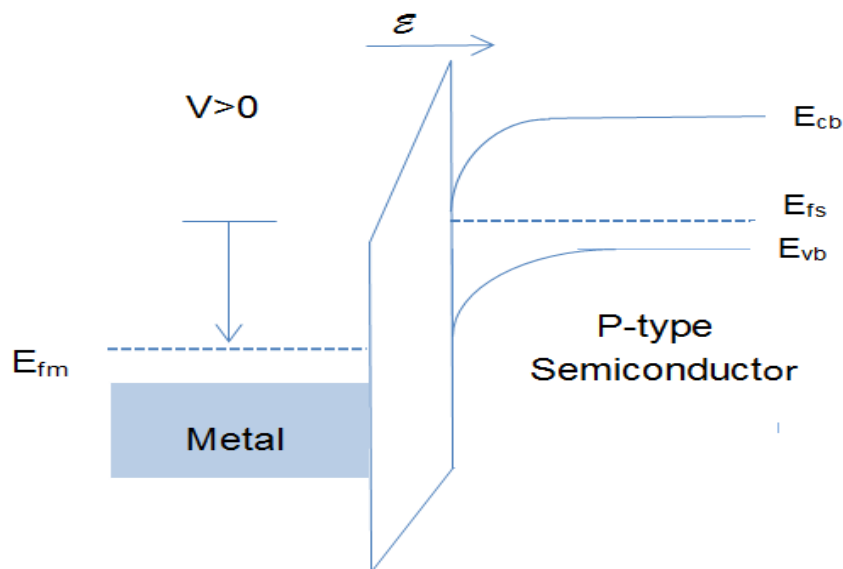

Figure 2.3a. Formation of the depletion region.

2.2.2 Formation of an inversion region

An inversion layer forms instead of depletion when more and more positive voltage is applied between the metal and the p-type semiconductor, as can be seen figure 2.3b. A large electron concentration formed in the interface due to a large positive voltage being applied causes the E_{cb} level to bend below the E_{fs} level near to the interface. This is due to the creation of a large electron concentration at the interface and the conduction band leads to the formation of an n-type surface layer by inversion of the original p-type character of the semiconductor [4,11,12].
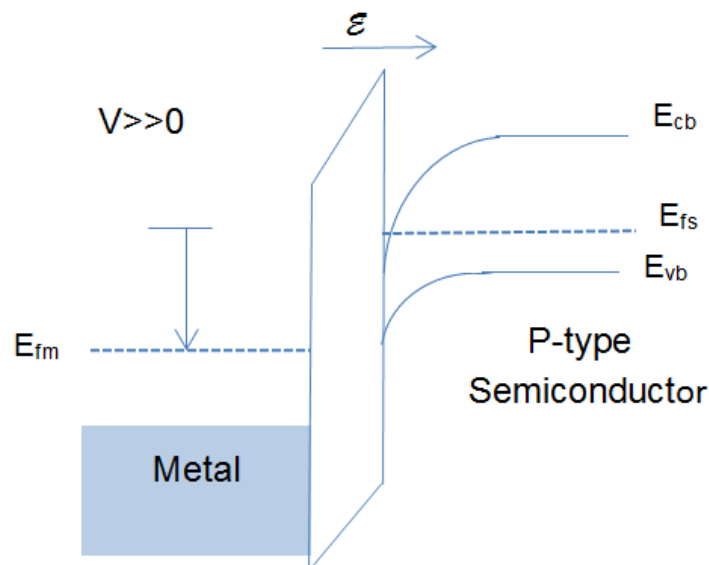
Figure 2.3b. Formation of the inversion region.

2.2.3 Formation of an accumulation region

When a negative voltage is applied between the metal and the p-type semiconductor, a negative charge resides on the metal. As a result of the applied negative voltage all E_i, E_c and E_v bands bend upward in order to allow the holes to accumulate closer to the oxide/p-type semiconductor interface. The effect of this electric field causes a net displacement of the oxide conduction band. The negative charge residing at the metal results in an equal net positive charge owing to the accumulation of holes at oxide/p-type semiconductor interface. A larger hole concentration arises, indicating that the semiconductor Fermi level, E_{fs}, has reached the same level as the energy of the metal valence band see figure 2.3c. Formation of such an accumulation layer at the interface thereby enhances positive charge carrier densities [4,11,12].
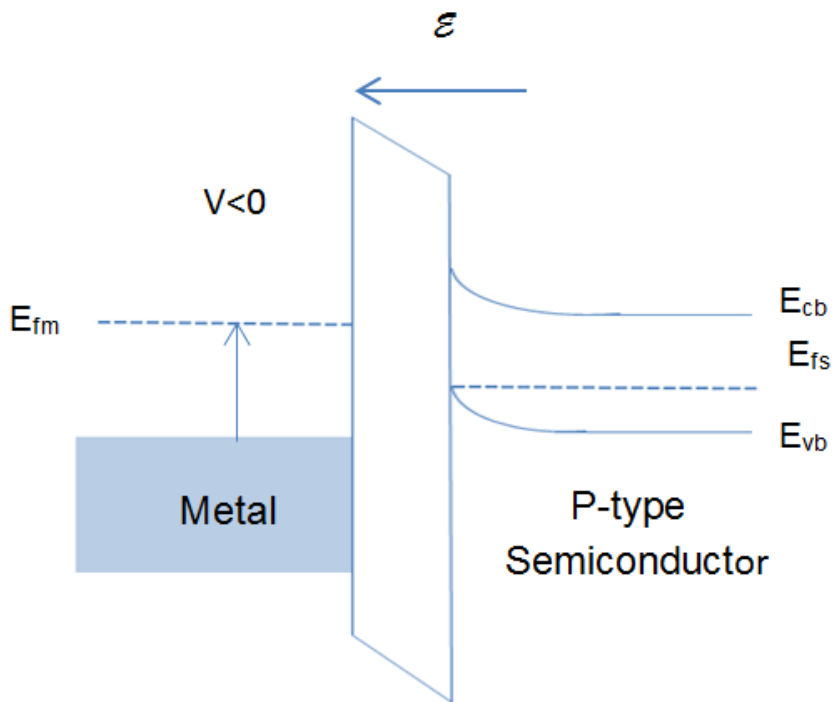
Figure 2.3c. Formation of the accumulation region.

2.3 MOS transistors and FET's

MOS transistors and FET's are formed by implementing a drain/source electrode arrangement as shown in figure 2.4 and doping the semiconductor to form n-type electrodes in the p-type body of a MOS capacitor [13].
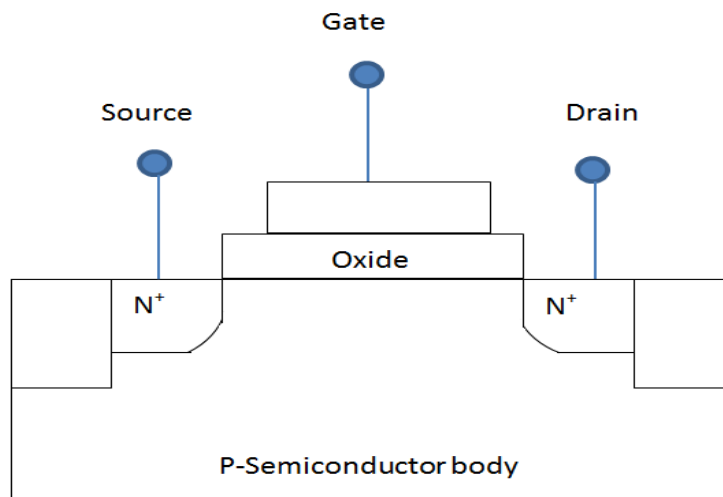
Figure 2.4. The basic silicon-based metal-oxide-semiconductor FET (MOSFET) structure.

In FET's charge carriers are involved in charge transport; in the n-type TFT electrons are the majority charge carriers while in p-type TFTs the majority charge carriers are holes. Like its bipolar transistor counterpart, the FET has three components: a gate, a source and a drain electrode. For example, in a p-type TFT, a negative gate voltage establishes an electric field in the direction of the p-type substrate; this may cause positive charge carriers to accumulate at the p-type substrate / oxide interface. The physical structure of TFTs is dependent on the sequentially deposited order of the semiconductor active layer, the insulator (dielectric) and the electrode layers [13].

OTFT's have the same features as the MOSFET structure, but OTFTs operate only in the accumulation region not in inversion. Structurally there are four common types of OTFTs that could be fabricated: either top- or bottom gated structures and either top- or bottom contact arrangements. Figure (5) schematically shows all four different TFT devices [14,15].
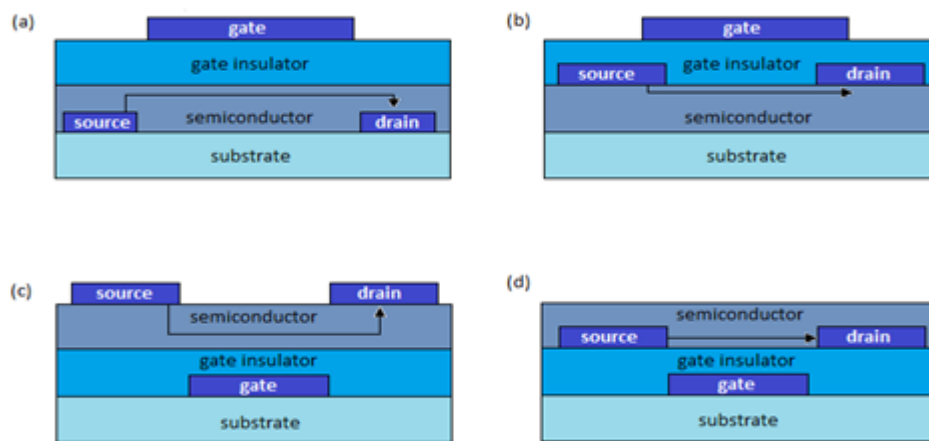
Figure 2.5. Representation of the four typical TFTs device structures: (a) top gate bottom-contact (b) top-gate top-contact, (c) bottom-gate top-contact and, (d) bottom-gate bottom-contact [14, 15].

2.4   Organic thin film transistors (OTFT's)

Almost all of my devices are p-channel organic OTFT's; here I explain the operation of p-type OTFTs, which is similar to that for MOSFET transistors. Figure (2.6) shows a simple structural configuration of top contact and bottom gate OTFTs. The source and the drain electrodes are separated by an organic p-type semiconductor and the gate electrode is separated from the (source & drain) electrodes by the substrate and an oxide insulator layer. The source contact is connected to the ground at all times.
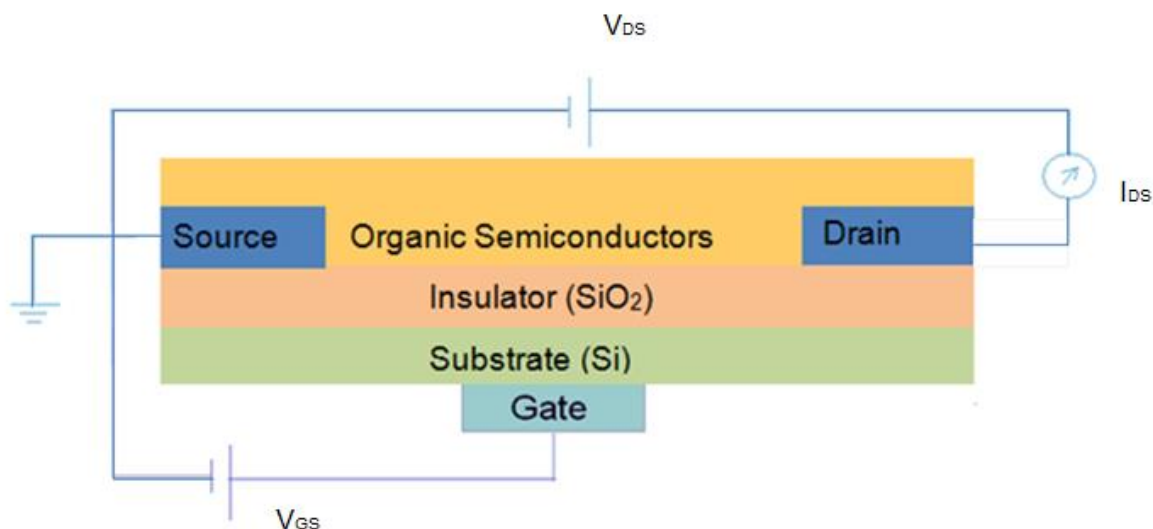
Figure 2.6. The essential connections to a top contact, bottom gate OTFT configuration.

At a simplified level, the transistor device is switched off at a gate voltage of zero. At this gate voltage there is no current flowing in the source-drain channel. For the p-channel to operate, the applied gate voltage has to be more negative than the negative drain voltage; by increasing the negative gate voltage the source-drain conduction pathway is enhanced. A negative gate voltage produces an electric field which attracts positive charge carriers in the semiconductor beyond the insulator layer. These carriers drift in the field and accumulate at the p-type organic semiconductor/insulator interface, thereby producing a channel of conduction. By applying a positive voltage at the gate, no output current is measured and hence the majority of p-type OTFTs only work in the accumulation mode [16,17].

In OTFTs the mechanism of conduction is clearly explained in refs.15 and 16; OTFT devices operate in the accumulation mode. Electronic charge carriers are accumulated in n-type semiconductors near the organic semiconductor/oxide interface when a positive gate voltage is applied. For p-type semiconductors and negative gate voltages, positive holes accumulate. In the organic semiconductors used in OTFTs, the lowest unoccupied molecular orbital (LUMO) level acts as the conduction band and the highest occupied molecular orbital (HOMO) level acts as valence band.

2.4.1 N-type OTFTs with electron accumulation

Applying a positive voltage between the gate and source electrode produces an electric field at the gate/insulator interface directly, and to the insulator/semiconductor interface. This electric field must be strong enough to affect the LUMO and HOMO levels; in n-type OTFT devices the LUMO energy approaches the work function of the source closely enough that the probability of charge transfers between the LUMO and the conduction band of the source becomes very high. In this way, electrons become injected as they start to flow from the source electrode into the LUMO of the semiconductor. The semiconductor molecules lying at the insulator interface can facilitate charge transport owing to

their proximity to one another (overlap, etc.) and closely similar LUMO energies. This causes a channel to be formed at the organic semiconductor/oxide interface via the accumulation of injected electrons. The electron current flowing in the channel can be measured by applying a drain-to-source voltage and gate-to-source voltage that exceeds a threshold for the onset of accumulation to occur [17, 18].

2.4.2   P-type OTFTs with hole accumulation

In p-type OTFT devices the applied gate to source voltage is negative; this causes the HOMO and LUMO levels to move upwards in energy. In p-type OTFT devices the HOMO energy must match the work function of the source material to increase the probability of electron transfer from the HOMO to the source. In p-type devices, this is equivalent to holes being injected into the semiconductor and accumulating at the organic semiconductor/oxide interface. Similar to n-type OTFTs, in the P-type OTFTs a device channel output current now occurs as a result of negative drain-to-source and gate-to-source voltages [17,18].
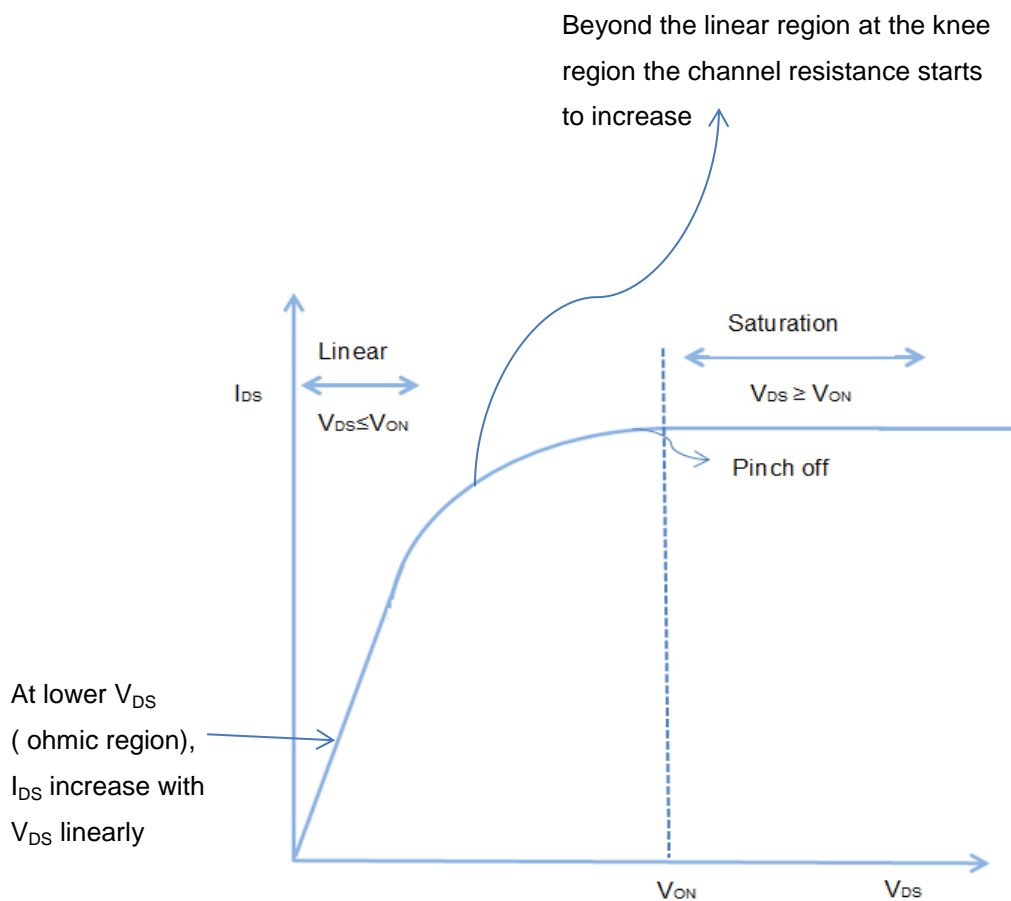
Figure 2.7. The different operating regimes of an OTFT at constant gate voltage, V_{GS}.

The gate voltage at which the onset of current flows in the accumulation region is defined as the threshold voltage, V_T. Once current-flow operates in the accumulation region (when $V_{GS} > V_T$) then a conduction channel has formed between the drain and the source. In field effect transistors there are two operational regimes (see figure 2.7). In the linear regime the current flowing within the channel is almost directly proportional to drain voltage; here the drain voltage is low and $V_{DS} \ll V_{GS} - V_T$. As the source-drain voltage increases further, i.e. beyond the "pinch off" point at $V_{DS} = V_{GS} - V_T$ the device enters its saturation regime. In the saturation regime the current flow from the source to the drain is apparently constant where $V_{DS} \gg V_{GS} - V_T$ [19, 20, 21].

2.5.1 The Square Law I_{DS} -V_{DS} relationship

The gate electrode and the channel layer are separated by an insulating oxide, and so these two parallel layers can act as a capacitor. As a gate voltage is applied, an electric field is produced between these two layers. As a result of this electric field, charge carriers accumulate at the semiconductor/oxide interface. As a voltage is applied between the drain and source electrodes, a lateral field causing the accumulated carriers to drift with a given velocity from source to drain occurs. The flow of total current in the channel can be expressed as follows:

Current is the rate flow of charge; a flow of electronic charge past specified per second can be expressed by the current equation:

$$I = \frac{charge}{time} = \frac{dQ}{dt}$$
(2.5.1.1)

A typical MOSFET is a 3-dimensional device, so the gate capacitors, channel length and width need to be included through equations (2.5.1.2) & (2.5.1.3):
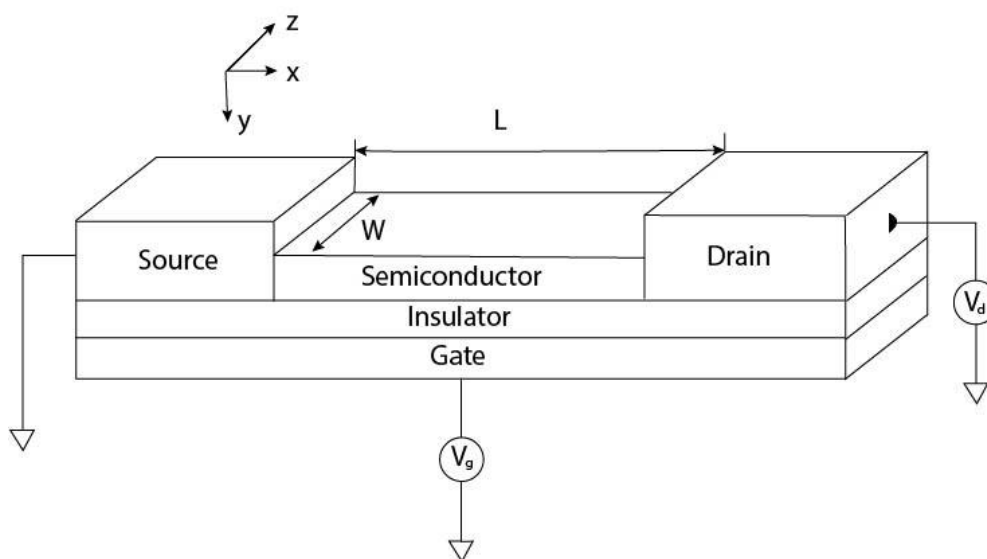
Figure 2. 8. Three dimensional arrangement of a MOSFET, current flows in x-direction.

14

A flow of electronic charge passing the location of an elemental section, dx, along the channel length, L, with drift velocity, v_x, produces a current (I) as a function of (V_G,V_T). I can be expressed as:

$$current(I) = charge\ density\ \times\ drain\ electrode\ area\ \times\ drift\ velocity(\ v_x\ )$$

(2.5.1.2)

The charge per unit gate area, Q_x, is given by:

$$Q_x = capacitance\ per\ unit\ gate\ area\ (C_{ox})\ \times\ voltage\ difference$$

(2.5.1.3)

so that an elemental electric charge, dQ_x, for a small voltage element, dV, is expressed by:

$$dQx\ =\ Capacitance\ per\ unit\ gate\ area\ (C_{ox})\ \times\ dV$$ (2.5.1.4)

Considering an infinitesimal small element of dx in the gate region the capacitance is expressed as:

$$charge = capacitance\ per\ unit\ gate\ area\ (C_{ox})\ \times\ the\ area\ of\ small\ element \times dV$$

(2.5.1.5)

The electric charge stored in a small element, dx

$$Q = C_{ox} \times\ W\ \times\ dx \times dV$$ (2.5.1.6)

The channel voltage varies as a function of x depending on the location in the channel. Hence the voltage V_x at the location of a small element (dx) is included in the effective voltage as:

$$voltage = effective\ voltage\ = (V_{GS} - V_T - V_x)$$ (2.5.1.7)

Consider the charge induced in the channel per unit area of oxide at the point x. For the elemental section, dx, the total charge is given as:

$$Q_x =\ C_{ox} \times\ W\ \times dx\ \times\ (V_{GS} - V_T - V_x)$$ (2.5.1.8)

and its velocity at location dx is given by:

$$v_x =\ \frac{dx}{dt} = electron\ mobility\ (\ \mu)\ \times\ electrical\ field\ (E)$$ (2.5.1.9)

where

$$E =\ -\frac{d\ V_x}{dx}$$ (2.5.1.10)

The electrons drift toward the drain in the direction indicated by the potential gradient, whilst the electric field along the direction of x takes the opposite sign, so that:

$$v_x = \mu_n \left(-\frac{dV_x}{dx}\right) \tag{2.5.1.11}$$

where μ_n is electron mobility of the channel. I_x can therefore be written as:

$$I \, dx = -C_{ox} \times W \times dx \times (V_{GS} - V_T - V_x) \times \mu_n \times \frac{dV_x}{dx} \tag{2.5.1.12}$$

where dx represents the position of an elemental slab. The current integration is carried out over the total channel length from source (x=0) to the drain (x=L), and similarly the voltage integration is from zero at the source to V_{DS} at the drain.

$$\int_0^L I_{DS} \, dx = \int_0^{V_{DS}} \mu_n \, C_{ox} W \left[V_{GS} - V_x - V_T\right] dV_x \tag{2.5.1.13}$$

$$I_{DS} \, L = W \mu_n C_{ox} \left[(V_{GS} - V_T)V_{DS} - \frac{1}{2}V_{DS}^2\right] \tag{2.5.1.14}$$

Therefore in the triode or linear region, the current I_{DS} is given by:

$$I_{DS} = \frac{W}{L}\mu_n C_{ox} \left[(V_{GS} - V_T)V_{DS} - \frac{1}{2}V_{DS}^2\right] \tag{2.5.1.16}$$

The highest amount of current going through the MOSFET is achieved when $V_{DS}=V_{GS}-V_T$. Above the pinch–off region, where the magnitude of $V_{DS} > (V_{GS}-V_T)$, the current reaches a saturation value where the apparent value of $V_{DS}=(V_{GS}-V_T)$. The extended current equation becomes:

$$I_{DS} = \frac{W}{L}\mu_n C_{ox} \left[(V_{GS} - V_T)(V_{GS} - V_T) - \frac{1}{2}(V_{GS} - V_T)^2\right] \tag{2.5.1.17}$$

$$= \frac{W}{L}\mu_n C_{ox} \frac{1}{2} \left[2(V_{GS} - V_T)^2 - (V_{GS} - V_T)^2\right]$$

$$= \frac{W}{L}\mu_n C_{ox} \frac{1}{2} \left[(V_{GS} - V_T)^2\right]$$

$$I_{DS} = \frac{W}{2L}\mu_n C_{ox} \left[(V_{GS} - V_T)^2\right] \tag{2.5.1.18}$$

The transistor equations (2.5.1.16) and (2.5.1.18) derived above are for devices with a crystalline active semiconductor layer, and are often referred to as the Square Law relationship [22,23]. They assume almost no leakage current. The electric field will be uniformly distributed, and the HOMO-LUMO band structure of the organic semiconductor will be optimal. Therefore, for a transistor device with a crystalline semiconductor the mobility (in cm^2 V^{-1}s^{-1}) is expected to be constant. For polycrystalline or amorphous semiconductor films, however, uniform intermolecular interactions will

only exist over a much shorter range. Charge transport theories are then proposed based on the organic semiconductor morphology which is characterised as polycrystalline or amorphous.

2.5.2 Charge transport in organic semiconductor materials

Organic semiconductor layers tend to exhibit only a short-range order owing to structural defects or degradation. Each defect may act as a trap state. The effect of these traps is to influence the field distribution within a device. The presence of a non-uniform lateral electric field as a result of the inhomogeneous morphology of the semiconductor film disrupts charge transport. As result, different analytical models have been developed to explore the effect of trap states that can significantly influence charge carrier mobility of OTFTs. Successful models must explain a mobility exhibiting a non-linear field effect dependence on gate-source voltage.

Raja & Eccleston [24] have demonstrated a simple but more fundamental analytical model compared with the original square law derivation [22,23]. Their initial assumption is that conduction in the disordered organic semiconductor layer occurs when charge carriers hop between discrete energy states. These discrete energy states act as traps; and as a result the conduction in OTFT devices particularly takes place via a variable range hopping (VRH) mechanism [24].

The defect region containing the traps that hinder charge carrier mobility are considered to occur in the energetic locality of HOMO–LUMO band gap. Electrons, or holes temporarily trapped in these states are assumed to contribute to overall charge transport. Hence, electrons/holes in band-tail states are added to the description of the transport model and allowing new model equations for OTFTs devices to be derived. As clearly seen in figure 2.9, the shaded regions depict localized trap energy states where electrons/holes are most likely to be trapped.
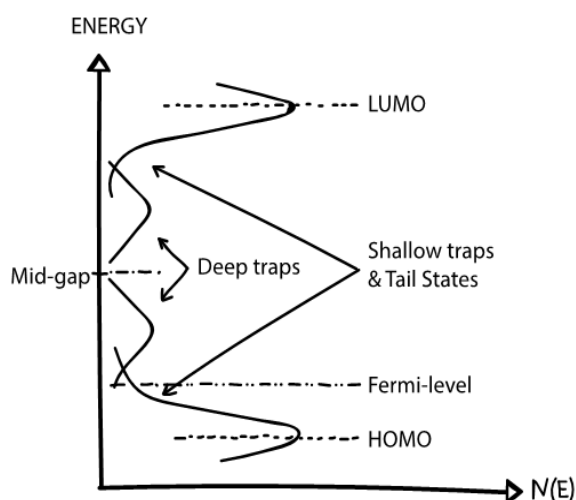
Figure 2.9. The concept for p-type organic semiconductor of Gaussian distributions of density of states and trap levels for trapped charges [26, 27].

17

This area is associated with a distribution of such states within an exponential tail; this is commonly referred to as a Gaussian tail density of states (Gaussian tail DOS) [25].The carrier density for a distribution of traps in terms of a characteristic temperature can be expressed as:

$$N'(E) = N'(0)exp(\frac{E}{k_B T_C})$$

(2.5.2.1)

N'(E) = *no. of carriers that can contribute to current*

N'(0) = *the density of states when the energy E relative to E_i is zero*

T_C = *the characteristic temperature defining the energy width of the distribution of traps.*

Assuming the fraction of states occupied is expressed by Maxwell–Boltzmann statistics; carriers below the Fermi level (E_F) are trapped and effectively static. The concentration of carriers above the Fermi level (E_F) exists in much shallower traps and can then contribute significantly to conduction. This fraction is given by:

$$f(E) = exp\left[-\left(\frac{E-E_F}{k_B T}\right)\right]$$

(2.5.2.2)

By adopting these two assumptions, the probability of increasing the rate of hopping to enhance the carrier's concentration can be derived. The majority carrier's concentration with energy above E_F is those carriers which contribute to the current flow, and are estimated by integrating the region from E_F to infinity. The total charge carrier concentration that contributes to the current flow then becomes:

$$n = \int_{E_F}^{\infty} N'(E)f(E)\,dE$$

(2.5.2.3)

Substituting equations (2.5.2.1) & (2.5.2.2) into (2.5.2.3) and rearranging, one obtains:

$$n = N'(0)exp(\frac{E_F}{k_B T}) \int_{E_F}^{\infty} exp(-\frac{E}{k_B T})exp(\frac{E}{k_B T_C})\,dE$$

(2.5.2.4)

Equation 2.5.2.4 expresses a distribution of the carriers in terms of a characteristic temperature (T_0), T_0 = the characteristic temperature defining the distribution of carriers which contribute to current and defined

$$\frac{1}{T_0} = \frac{1}{T} - \frac{1}{T_C}$$

(2.5.2.5)

Rearranging equation (2.5.2.4) using equation (2.5.2.5), one obtains:

$$n = N'(0)exp(\frac{E_F}{k_B T}) \int_{E_F}^{\infty} exp(-\frac{E}{k_B T_0})\,dE$$

(2.5.2.6)

After integration, the total carrier concentration is obtained

$$n = N'(0)k_B T_0 exp(\frac{E_F}{k_B T})exp\left(-\frac{E_F}{k_B T_0}\right)$$

(2.5.2.7)

The total carrier concentration can also be described in terms of the characteristic temperature (eq. 2.5.2.4), so that:

$$n = N'(0)k_B T_0 exp(\frac{E_F}{k_B T_C})$$

(2.5.2.8)

Of course, it is impossible to synthesize an organic semiconductor without introducing some level of contamination which could act as a dopant. However, if the organic semiconductor is assumed to be just an intrinsic semiconductor, then E_F in eq. (2.5.2.8) becomes E_i to form the intrinsic carrier concentration n_i, represented by:

$$n_i = N'(0)k_B T_0 exp(\frac{E_i}{k_B T_C})$$

(2.5.2.9)

Upon applying an electric field to a disordered system, the current density, J, can then be expressed as:

$$J = N'(0)k_B T_0 exp(\frac{E_F}{k_B T_C})q\mu_{eff}F$$

(2.5.2.10)

where

F= an applied electric field

μ_{eff}= field dependent mobility

Similarly, at an electric field, F, the current density can be expressed as

$$J = N_C exp(-\frac{E_C - E_F}{k_B T_C})q\mu_0 F$$

(2.5.2.11)

where

N_c= an effective density of states

E_c= conduction band edge

μ_o= field independent mobility

Combining the equations (2.5.2.10) and equation (2.5.2.11), μ_{eff} becomes:

$$\mu_{eff} = \mu_0 \frac{N_C}{N'(0)k_B T_0} exp\left(-\frac{(E_C - E_F)}{k_B T}\right) exp\left(-\frac{E_F}{k_B T_C}\right)$$

(2.5.2.12)

Rearranging equation 2.5.2.12, one obtains:

$$\mu_{eff} = \mu_0 \frac{N_C}{N'(0)k_BT_0} exp\left(-\frac{E_C}{k_BT}\right) exp\left(\frac{E_F}{k_BT}\right) exp\left(-\frac{E_F}{k_BT_C}\right) \qquad (2.5.2.13)$$

Noting that:

$$exp\left(\frac{E_F}{k_BT}\right) = exp\left(\frac{T_C}{T} \times \frac{E_F}{k_BT_C}\right) = \left(exp\left(\frac{E_F}{k_BT_C}\right)\right)^{\left(\frac{T_C}{T}\right)} \qquad (2.5.2.14)$$

Therefore equation (2.5.2.12) can then be rewritten as:

$$\mu_{eff} = \mu_0 \frac{N_C}{N'(0)k_BT_0} exp\left(-\frac{E_C}{k_BT}\right) \left(exp\left(\frac{E_F}{k_BT_C}\right)\right)^{\left(\frac{T_C}{T}\right)-1} \qquad (2.5.2.15)$$

From equation (2.5.2.8),

$$\frac{n}{N'(0)k_BT_0} = exp\left(\frac{E_F}{k_BT_C}\right)$$

so that:

$$\mu_{eff} = \mu_0 \frac{N_C}{N'(0)k_BT_0} \left(\frac{n}{N'(0)k_BT_0}\right)^{\left(\frac{T_C}{T}\right)-1} exp\left(-\frac{E_C}{k_BT}\right) \qquad (2.5.2.16)$$

,and finally

$$\mu_{eff} = \mu_0 \frac{N_C}{(N'(0)k_BT_0)^{\left(\frac{T_C}{T}\right)}} exp\left(-\frac{E_C}{k_BT}\right) (n)^{\left(\frac{T_C}{T}\right)-1}$$

$$= \mu_0 \frac{N_C exp\left(-\frac{E_C}{k_BT}\right) (n)^{\left(\left[\frac{T_C}{T}\right]-1\right)}}{\{(N'(0)k_BT_0)\}^{\left(\frac{T_C}{T}\right)}}$$

$$= K\, n^{\left[\left(\frac{T_C}{T}\right)-1\right]} \qquad (2.5.2.17)$$

where
$$K = \mu_0 \frac{N_C}{(N'(0)k_B T_0)^{\left(\frac{T_C}{T}\right)}} \quad exp\left(-\frac{E_C}{k_B T}\right)$$

Defining

$$m = \left(\frac{T_C}{T}\right) - 1 \qquad (2.5.2.18)$$

Then

$$\mu_{eff} = K \, n^m \qquad (2.5.2.19)$$

Various theories link the trapped charge concentration with a gate-voltage dependent mobility. Models by Natali, et al. [28], and Cerdeire et al. [29] both consider gate voltages and conclude that a gate induced charge offers a smaller contribution to the current flow compared with trapped charge. Charge carriers which exist in shallow traps able to contribute to conduction cause the mobility (μ_{eff}) to become field-dependent according to the empirical law[28]:

$$\mu_{eff} = \mu_\circ (V_{GS} - V_T)^\gamma \qquad (2.5.2.20)$$

where

$$\gamma = 2\left(\frac{T_C}{T} - 1\right) = 2\frac{T_C}{T_o} - 1 \qquad (2.5.2.21)$$

Comparing equations (2.5.2.18) and (2.5.2.21). one finds that γ and m are related by:

$$\gamma = 2m \qquad (2.5.2.22)$$

More rigorously, Raja and Eccleston [24] and Horowitz et al [4] have derived the explicit connection between equations (2.5.2.18) and (2.5.2.21). The expression for μ_{eff} in terms of its dependency on gate-source voltage becomes:

$$\mu_{eff} = \mu_\circ ((V_{GS} - V_T)^{2m} \qquad (2.5.2.23)$$

2.6   Summary

In this chapter the general features of transistor devices have been described, in particular the operation of OTFTs. In OTFTs, the mobility is affected by the internal field; it varies with gate voltage and depends on a carrier concentration hopping between localized states. Localised states trapping charge carriers are more likely to contribute to charge flow if they lie above the Fermi level. This is in

contrast to inorganic semiconductors, which are crystalline, and where field effect mobility is constant. In OTFT's, the effective mobility, μ_{eff}, can be expressed as a non-integer power law dependence on a voltage providing a transverse field. The principal parameter, m, (or γ) is related to the non-crystallinity of organic semiconductor materials.

References

[1] White, M. A. (1999) 'Properties of Materials' New York .Oxford, Oxford University Press, pp.250-251.

[2] Callister, W.D. (2007) 'Material Science and Engineering an Introduction (seventh edition)', United States of America, John Wiley & Sons, pp. 696-698.

[3] Lilienfeld, J. E. (1930) 'Method and apparatus for controlling electric current', Jan. 28, 1930, U.S Patent 1 745 175.

[4] Atalla, M. M. et al. (1959) 'Stabilization of silicon surfaces by thermally grown oxides', *Bell Syst. Tech. J.*, **38** (**3**), **749**-**783**, doi: 10.1002/j.1538-7305.1959.tb03907.x.

[5] Weimer, P.K. (1962) 'The TFT a new thin-film transistor' *Proc. IRE*, **50**(**6**), **1462**-**1469**,doi: 10.1109/JRPROC.1962.288190.

[6] Clarisse,C., Riou, M.t., Gauneau, M., et al (1988) 'Field-effect transistor with diphthalocyanine thin-film' *Electron. Lett.* , **24**(**11**), **674**-**675**, doi: 10.1049/el:19880456.

[7] Kudo, k., Yamashina, M and Moriizumi,T. (1984) 'Field-effect measurement of organic-dye films'*J. Appl. Phys.,* **23**(**1**), **130**, doi: 10.1143/jjap.23.130.

[8] Tsumura, A., koezuka, H., Ando, T., et al. (1986), 'Macromolecular electronic device - field-effect transistor with a polythiophene thin-film', *Appl. Phys. Lett.,*(**49)18**, **1210**-**1212**, doi: 10.1063/1.97417.

[9]Anderson,P.A. (1959) 'Work Function of Gold', *Phys. Rev.,***115**(**3**),**553**, doi:10.1103/physrev.115.553.

[10] Kwong, C.Y., Djurisic, A.B., Chui, P.C., et al. (2003) 'Improvement of the efficiency of phthalocyanine organic Schottky solar cells with ITO electrode treatment', *Appl Phys A Mater Sci Process*, **77**(**3**), **555,** doi: 10.1007/s00339-002-1493-6.

[11] Goda, T. and Miyahara, Y. (2011) 'DNA Biosensing using Field Effect Transistors', *Curr Phys Chem*,**1**(**4**),**276**, doi: 10.2174/1877946811101040276.

[12] Trager, F. (2012) 'Springer hand book of lasers and optics', 2nd edn., Springer-Verlag Berlin Heidelberg , pp. 582-589, doi:10.1007/978-3-642-19409-2.

[13] Smith, R. J. and Dorf, R. C. (2009) 'Circuits, Devices And Systems 5th edn.', *John Wiley* & *Sons*, *Inc* (*Wiley*), Canada, pp. 368-379, ISBN: 8126511036, 9788126511037.

[14] Xu, Y., Liu, C., Khim, D. and Noh, Y-Y. (2015) 'Development of high-performance printed organic field-effect transistors and integrated circuits',*Phys.Chem.Chem.Phys.*,**17**(**40**),**26553**, doi: 10.1039/c4cp02413c.

[15] Lee, W, H. and Park, Y. D. (2014) 'Organic Semiconductor/Insulator Polymer Blends for High-Performance Organic Transistors' , *Polym. J.*,**6** (**4**),**1057**, doi:10.3390/polym6041057.

[16] Brondijk, J. J., Spijkman, M., Van Seijen, F., et al. (2012) 'Formation of inversion layers in organic field-effect transistors', *Phys. Rev. B* , **85** (**16**),**165310**, doi:10.1103/PhysRevB.85.165310.

[17] Dimitrakopoulos, C. D. and Malenfant, P. R. L. (2002) 'Organic Thin Film Transistors for Large AreaElectronics',*Adv.Mater.*,**14**(**2**),**99**,doi:10.1002/1521-4095(20020116)14:2<99::aid-adma99>3.0.co;2-9.

[18] Newman, C.R., Frisbie, C.D., et al. (2004) 'Introduction to Organic Thin Film Transistors and Design of n-Channel Organic Semiconductors', *Chem. Mater.*,**16**(**23**),**4436** , doi: 10.1021/cm049391x.

[19] Schoiswohi,J. (2017) 'Linear Mode Operation and Safe Operating Diagram of Power-MOSFETs', 81726 Munich, Germany, Infineon Technologies AG, Application note v1.1, pp.1-13, WWW.infineon.com (Schoiswohi,J. (2017), 'MOSFET linear mode operation and SOA power MOSFETs' Version 01-00 , 2017-05-05, pp:1-13 , WWW.infineon.com.

[20] Wie, C.R. (2010) 'Nonsaturating Drain Current Characteristic in Short-Channel Amorphous-Silicon Thin-Film Transistors', *IEEE Electron Devices Society*,**57**(**4**),**846**-**854**,doi: 10.1109/TED.2010.2040935.

[21] Park,S. (2008) 'Review: MOSFET Modeling and CMOS Circuits' Institute for Real-Time Computer Systems   Technische Universität München, park@rcs.ei.tum.de.

[22] Kagan, C. R. and Andry, P. (2003) 'Thin-film transistors', IBM T.J.Watson Rsearch Center Yorktown heights, New York USA, taylor & francis e-library, pp.1-47, ISBN 0824747542, 9780824747541.

[23] Lee, T. H. (2002) 'A Review of MOS Device Physics', rev. September 26, 2002; p:**1-33**, https://web.stanford.edu/class/archive/ee/ee214/ee214.1032/Handouts/HO2.pdf.

[24] Raja, M. and Eccleston, W. (2011) 'Analytical device models for disordered organic Schottky diodes and thin-film transistors for circuit simulations', *IET Circuits Devices Syst.*,**6**(**2**),**122**,doi: 10.1049/iet-cds.2011.0199.

[25] Ruhstaller,B., Knapp, E., Perucco,B., et al. (2011) 'Advanced Numerical Simulation of Organic Light-emitting Devices', Zurich University of Applied Sciences, Institute of Computational Physics, 8401 Winterthur and Fluxim AG, 8835 Feusisberg Switzerland, p:**433**-**459**, doi: 10.5772/14626·

[26] Ruhstaller,B., Knapp, E., et al. (2014) 'Advanced Numerical Simulation of Organic Light-emitting devices',p:434-**458**,doi:10.5772/14626·Source:InTech, www.intechopen.com.

[27] Carr, J. A. and Chaudhary, S. (2013) 'The identification, characterization and mitigation of defect states in organic photovoltaic devices: a review and outlook ', *Energy Environ. Sci.*, **6**(**12**),**3414** , doi: 10.1039/c3ee41860j.

[28] Natali, D., Fumagalli, L., and Sampietro, M. (2007) 'Modeling of organic thin film transistors: Effect of contact resistances' *J. Appl. Phys.*, **101**(**1**), **014501,**doi: 10.1063/1.2402349.

[29] Cerdeira,A., Estrada,M., Garcia,R., et al. (2001) 'New procedure for the extraction of basic a-Si:H TFT model parameters in the linear and saturation regions ' *Solid-State Electron.*, **45**(**7**) **1077** doi: 10.1016/S0038-1101(01)00143-5.

3. OTFT MODELS AND ANALYSIS PROCEDURES

Various mathematical expressions have been proposed for the accurate modelling of OTFT devices. The models distinguish themselves mainly by their handling of the organic semiconductor active layer. Identification of the correct model for OTFT's is therefore crucial. This chapter focuses on the development of different analytical models and their theoretical basis; they include essential transistor parameters and semiconductor properties, such as threshold voltage and mobility. The application of mathematical modelling techniques for OTFTs can be a challenge owing to a poor understanding of the effect of the organic semiconductor layer's structure or geometry within the device. Nevertheless, the theoretical interpretations of the physical and chemical behaviours underpinning the proposed models have similarities.

At an early stage, one research group [1] recognised that the transistor parameters are over-estimated if extracted via the conventional crystalline equation [1], also known as the square law equation (see chapter 2). This equation derives from c-si mosfet devices; the theory was created by assuming that the field is uniformly distributed throughout the semiconductor material which exhibits a constant mobility. However, realistic organic semiconductors with larger trap depths cause the charge to be transported in a dispersive manner [2]. Distributed trap charge densities are more likely to occur at grain boundaries within the depth of the organic semiconductor film [2,3]. Additionally, OTFT's will have a contact resistance at the metal / semiconductor interfaces for both the source- and drain electrodes. There, the organic semiconductor in contact with the metal interface will introduce other chemical and physical defects [1,2,4]. For these reasons, as well as supporting morphological evidence, realistic organic semiconductor materials must be considered to be polycrystalline, or amorphous, rather than crystalline [2,5,6]. Consequently, extracted mobilities using the square law equation results in over-estimation.

3.1 Analytical models

The analytical models used are based on the transportation of charge carriers in polycrystalline or amorphous organic-semiconductor materials. Models are generally based on trap-and-release charge carrier mechanisms [7]. In most publications the derived analytical expression values are in an excellent agreement with experimental data. However, using multiple analytical models for each individual organic semiconductor device was challenging and time-consuming. Early studies looking at the behaviour of OTFT devices noted that the electron- or hole charge carriers are transported in a dispersive way[1,2], and that the mobility increased when the gate voltage increased [1,2,8,9]. In what follows, theories that describe a carrier mobility dependence on gate voltage are the focus of attention. This dependence may be associated with traps in the device and/or charge carriers hopping between localised states [7, 9]. Another possible reason is that active-semiconductors in OTFT's can

be polycrystalline and the electron or hole charge carriers become trapped at the boundary between crystals. These trapped electron/hole barrier heights are reduced as the applied gate voltage increases [2].

The starting point for researchers to develop new physical models was the crystalline equation theory:

Linear region

If $V_{GS}-V_T > 0$ and $V_{DS} < V_{GS}-V_T$ then the crystalline equation for P-MOS in linear region

$$I_{DS} = -\mu_{eff} \; C_{ins} \frac{W}{L} (V_{GS} - V_T)V_{DS} \qquad (3.1.1)$$

where C_{ins} is the capacitance to the insulated gate.

Saturation region

If $V_{GS}-V_T > 0$ and $V_{DS} > V_{GS}-V_T$ then the crystalline equation for P-MOS in saturation region

$$I_{DS} = -\frac{1}{2}\mu_{eff} \; C_{ins} \frac{W}{L} (V_{GS} - V_T)^2 \qquad (3.1.2)$$

Model by Hamilton et al. & Shea et al.

This model [1, 2] assumes that the transport of charge through the bulk of the organic thin film occurs by a scattering process (see previous section). Hence, above the threshold voltage on the graph showing I_{DS} as a function of V_{GS} for linear region, there is not always a perfect linear behaviour. Likewise, for the saturation region, the best straight line fit for $\sqrt{I_{DS}}$ as a function of V_{GS} does not cover a broad range of V_{GS} [1, 2].

These researchers believed that this mechanism of carriers transport is the reason for the nonlinearities observed from both the linear and saturation transfer characteristic curves, and results from the amorphous nature of organic semiconductors. To overcome this nonlinearity, Hamilton et al. [1] modified the existing MOSFET equations. They introduced a variable called γ into the MOSFETs original equation to accommodate the dependence of mobility on gate voltage. If the organic semiconductor in the device has a long range order with high crystallinity, then the γ values are more likely to be close to zero. Their studies confirmed that with identical devices, the γ values may be affected by different processing techniques and conditions [1, 2]. Note that the empirical γ defined by these authors differs from that used in equations 2.5.20 to 2.5.23.This is often referred to as a non-linear curve-fitting model.

Linear region

$$I_{DS} = -\mu_o \ C_{ins} \frac{W}{L} (V_{GS} - V_T)^\gamma V_{DS}$$ (3.1.3)

where μ_o is modified field-effect mobility and γ is fitting parameter for a power–law dependence. This dependence was thought to arise from " ... the charge carrier transit time between two points." [2]. Both γ and the constant factor $C_{ins}(W/L)\mu_o$ are extracted by nonlinear curve fitting; then μ_{eff} is evaluated using Eq. (3.1.4).

$$\mu_{eff} \ = \mu_o(V_{GS} - V_T)^{(\gamma-1)}$$ (3.1.4)

 Saturation region:

$$I_{DS} = \mu_o C_{ins} \frac{W}{L(\gamma+1)} \ (V_{GS} - V_T)^{(\gamma+1)}$$ (3.1.5)

Similar to the linear region, once the γ and the constant terms are extracted from nonlinear curve fitting, μ_{FE} is then evaluated using Eq. (3.1.5).

$$\mu_{eff} = \mu_o(V_{GS} - V_T)^{(\gamma-1)}$$ (3.1.6)

One of the deficiencies of this nonlinear curve fitting model was the non-inclusion of the contact resistance at the drain and source terminals.

Model by Natali et al.

The analysis model Natali et al [8] had two main hypotheses: one was that in organic semiconductor devices, mobility increases with gate voltage. Their second hypothesis was that contact between the organic semiconductor and the source- or the drain gold electrodes at their interfaces is not ohmic but more likely to be a Schottky type contact. However, their analytical model was based on the inclusion of ohmic contact resistances only.

Natali et al noted that two possible explanations are reported in the literature. One involves the multiple trapping and release transport model,(MTR) [9] where only a fraction of the gate induced charge contributes to the current flow, the remaining part being trapped in an exponential tail of trapping states. Alternatively, in the variable range hopping model (VRH),[10] carriers contribute to current flow only when they are excited to a so-called transport energy level: at higher carrier concentrations. In both models mobility follows a power law dependence $\mu = \mu_0 (V_{GS}\text{-}V_T)^m$.

The contact resistance at the source terminal could be presented as R_S and the potential is raised by the amount of $R_S.I_{DS}$. As the current flows through R_S, this suggests that the applied gate voltage (V_G) will not be equal to gate-to-source voltage (V_{GS}) therefore V_{GS} expressed as: $V_{GS} = V_G - R_S.I_D$. Similar to the V_{GS} expression, V_{DS} is expressed as follows: $V_{DS} = V_D - R_{SD}I_D$.

The drain to source voltage (V_{DS}) is not equal to the applied drain voltage (V_D), V_{DS} is connected to V_D through R_D and this time both contact resistances, R_D and R_S, were involved at the drain terminal as $R_{SD}=R_S+R_D$. Expressions for the linear and saturated regimes assumed that the source terminal is not grounded, and also consider the nonlinear effect to be due to the amorphous semiconductor layer of the OTFTs. Their other observations were that the total contact resistance in the linear region decreased with increasing gate voltage, but in the saturation region, the contact resistance is constant. In the saturated region, only R_S is considered because the contact resistance at the source was claimed to be higher than that at the drain.

Due to limitations of their method, the extracted device parameters were based on small intervals of gate-to-source voltage; both differential and integration techniques are needed to extract device parameters. These techniques lead to considerably higher errors in the extracted parameters.

Model by Estrada et al.

One model category comprises the so-called "Accurate" models [12], where the initial device parameters are extracted by the Unified-Model–and-parameter-Extraction-Method (UMEM). This type of model was first established for amorphous silicon TFT (a-Si TFT)[13] and was later reused for the dc-electrical characteristics of OTFT devices. The model was expanded by introducing an additional hypothesis in order to calculate the characteristic temperature and energy distribution of localized states as a density of states (DOS) in the active semiconductor layer [14].

Common to all OTFT devices, a non-zero drain current at zero drain source voltage in the characteristic output curves, is observed. Yingping and his colleagues [15] extended the "Accurate" models to reveal the cause of this non-zero drain current point at zero source-drain voltage. To do this they used an equivalent circuit combined with "Accurate" models; their findings showed that this non-zero-current was due to large contact resistance and small gate resistance [15].

Unlike the model by Natali et al., their hypotheses involved physically monitoring the entire experimental curve from the output to transfer characteristic in both the strong and weak inversion (sub-threshold) regions. However, some of the parameters have no physical meaning. In addition, the model places no limitation on both the empirical fitting parameter (γ) and channel length modulation (λ) use to calculate the knee region for the output curve. Both can be positive or negative, whereas most research groups believe these empirical fitting parameters to be positive. Also, an extra parameter is arbitrarily added to control the sharpness of the transition ("knee") between the linear and saturation regions. Furthermore, in this model it is not clearly explained why the default fitting parameter (band mobility, μ_0) was taken as twice the μ_{eff} values of the saturation region square law

equation [15]. Finally, the total contact resistance is extracted at maximum gate voltage using the linear region current. In their procedure, model parameters such as γ and V_T were first extracted using the experimental transfer characteristic data in the linear region at a low value of V_{DS}, and an integration technique was used [13,16,17,18,19]. However, this approach uses a model having an excessive number of parameters and relies on the selective use of a small number of data points, which in any event are not noise-free. The errors can be extremely high and lead to poor conclusions. Similar drawbacks were observed in the model of Natali et al. [8].

AIM & SPICE Modelling

Automatic Integrated Circuit Modeling (AIM) [20] and Simulation Program with Integrated Circuit Emphasis (SPICE) [21] refers to a standard circuit simulator and is well accepted for industrial and academic purposes. The AIM-SPICE models level 15 were initially created for a-Si:H and polysilicon TFTs, respectively [21]. A modified Level 15 model is also used to characterise OTFT's [12], but more than 18 parameters are needed [13]. Nguyen et al [22] were reported that 10% errors in fitting are considered acceptable, leading to the ambiguities within the model, and extremely unreliable parameters. Models by Z. Xie et al. [23] and Shur [24] also used AIM-SPICE models to analyse OTFT components.

Model by Xie, Z et al.

A computer based model [22] was developed for polymer based OTFTs device by Xie, Z et al, Their model incorporated both leakage current and contact resistance at the drain and source contacts. These models were implemented in SPICE.

Model by Necliudova and Shur

Necliudov et al. [25] extended Xie et al's work, using an equivalent circuit which is composed of a linear contact resistance joined at the source and drain terminals, followed by a pair of anti-parallel leaky Schottky diodes. According to their theory, the Schottky diodes obtain symmetric current-voltage characteristics, the ideality factors of the diodes are governed by the steepness of the current–voltage characteristics and the overall model was suitable for nonlinearity measurement. This model was used to examine both bottom contact and top contact TFT devices, and the model used the whole I-V characteristics of an experimental curve, including above and below the V_T regimes. The model was found to be suitable for TC pentacene OTFTs.

Model by Baeseller
The so-called Gaussian disorder model proposed by Baeseller [26], is an extension of the Variable Range Hopping (VRH) model mentioned above. It has been used to explain mobility in disordered semiconductors using the time-of-flight measurements, and is believed to be the most successful theory in explaining charge transport in disordered organic materials.

His model accounts for two types of disorder. Firstly, diagonal disorder which involves a distribution of the energies of the carriers on the hopping sites, is assumed to be Gaussian with variance σ. Secondly, off-diagonal disorder which represents the variation of intersite electronic wave function overlap arising from both positional and orientational disorder of nonspherical molecules attached to each site, is also assumed to be Gaussian with variance Σ. Here, mobility is dependent on temperature, charge-density, electric field and disorder.

Unfortunately, contact resistance effects are neglected so application of this model to analysis the OTFT faces many challenges. In addition, thorough analysis involves Monte Carlo simulations, which are computationally time-consuming. Such simulations generally involve extra arbitrary parameters, and would not be accurate for extracting the relevant OTFT parameters. Attempts to extract mobility values from OTFT measurements have relied either on the linear region of transfer experiments [27], or the linear region of output experiments[28], by using early "square law" expressions. Berliocchi [29] notes that this procedure, however, could underestimate or overestimate the real mobility value because it is extracted with the implicit hypothesis of constant mobility.

Model by Raja & Eccleston

The Raja & Eccleston model is based on the variable range hopping (VRH) model, but generalizes the dependence of mobility on a Universal Mobility Law, which leads to the familiar expression $\mu = \mu_0 (V_{GS}-V_T)^m$. The theory of Raja et al. [7] provides a model based on bulk trapping which assumes that electron/hole mobility depends on carrier concentration. As the carrier concentration increases, carriers are spaced closer together but in higher energy states. This is thought to enhance the probability of carriers hopping and thus improve mobility. The development of the entire model was based on an MOS-crystalline device approach. In light of the difficulties described above in relation to the Baesseler model, it was decided to adopt the Raja and Eccleston approach, and tackle the more practical issues regarding contact resistance - including Schottky effects – in the parameter extraction procedure.

Among research groups in general, a common agreement has not yet been reached on how to achieve more accurate analytical models for an OTFT device. However, all agree that the extracted parameters of OTFT devices are over-estimated via the square law MOS-crystalline TFT equation, since the nature of OTFT devices is quite different in terms of semiconductor crystallinity.

The research described in this thesis endeavours to provide a different analytical model to extract accurate transistor parameters. Working together with C.J.Winscom, we have come to a conclusion that the model by Raja & Eccleston is the most reasonable to follow. Their model is clearly presented and contains the smallest number of physically-meaningful parameters. It provides a sound starting

point to easily upgrade, compared with the above well-known models. However, in common with all models described in the last two decades, sign information relating to the drain current, the drain-source voltage and the gate-source voltage has been casually neglected. Electronic common sense requires that the drain current has the same sign as the drain–source voltage, particularly in the saturation region (see e.g. equation 3.2).

In the next section the extended Raja & Eccleston model is presented. The model was first modified, then passive contact resistance effects at drain and source terminals were introduced. This provides a sound 4-parameter model on which to base a statistical modelling approach for parameter extraction. This basis was then further extended to include passive-to-Schottky-diode contact effects, passive contributions from the bulk semiconductor beyond the gate dielectric region, and passive leakage current effects from the gate to the adjacent semiconductor in the gate dielectric region.

3.2 Modified analytical method

Raja & Eccleston's model [7] was developed for the operation of n-channel top-gated OTFTs in accumulation mode. Assuming carrier density depends on the depth of the semiconductor's accumulation layer, their two-dimensional approach also includes the channel length for finite gate and drain voltages with respect to the source. Unlike Raja & Eccleston's model, here the model's operation is described for a p-type semiconductor channel. Figure 3.1(a) shows the main dimension-definitions and axes in relation to the source, gate and drain electrodes. Figure 3.1b shows a 2-dimensional cross-section of the accumulation layer, and the transverse (V_y) and lateral (V_x) fields produced by the gate potential, and the source-to-drain potential difference, respectively. Figure 3.1(c) is similar to (b), but illustrates a small segment where under conditions of saturation $V_{GT} \leq V_D$ the potential at the dielectric surface is not sufficient to produce accumulation. For brevity, $V_{GT} = V_G - V_T$.
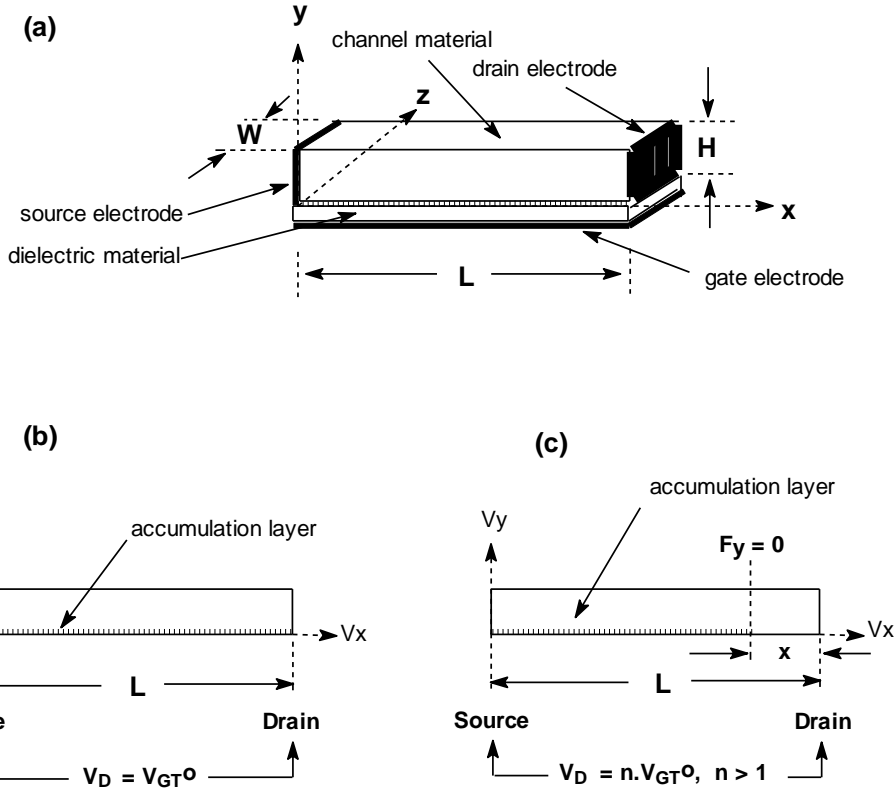
Figure 3.1. (a) Simplified source-drain-gate arrangement of an OTFT showing axes definitions and dimensions of the organic material channel, and the accumulation layer at the interface of the semiconductor and gate dielectric, (b) the 2-dimensional representation of operation in the linear regime, showing the carrier-density enhanced surface conduction within the channel, when $V_D = V_{GT}{}^0$, and (c) the 2-dimensional representation of operation in the saturated regime, with $V_D = n.V_{GT}{}^0$, n>1.

For n-type semiconductors, and with a positive gate bias, i.e. the voltage V_{GS} relative to the source electrode, the total accumulated charge at the semiconductor / oxide interface is expressed in terms of the charge(Q_o) per unit area as follows:

$$Q_o \;=\; n\,q\,dy \;=\; -C_0\,(V_{GS} - V_x) \qquad\qquad (3.2.1)$$

where q is the unit carrier charge, n is the charge carrier concentration, dy is an element of the depth normal to the dielectric surface, C_0 is the capacitance/unit area across the gate dielectric and V_x is the potential as a function of distance in the lateral (x) direction between the source and drain.

For example, positive charge carriers will start to flow from the source to the drain electrode as a negative voltage (V_{DS}) is applied; and *vice-versa* for negative charge carriers. The total current density (J) can be expressed as

$$J = nq\mu_{eff}F_x \qquad\qquad (3.2.2)$$

32

where F_x is the electric field in the x-direction between the source and drain, and μ_{eff} is the effective mobility. However, for a disordered active layer, μ_{eff} varies strongly with carrier concentration, and is known as the Universal Mobility Law [7]:

$$\mu_{eff} = K\, n^m \tag{3.2.3}$$

where one should assume 0 < m < 1.

Thus J can be expressed:

$$J = qKn^{m+1}F_x \tag{3.2.4}$$

Furthermore, due to the transverse potential at the dielectric surface that arises when a negative voltage is applied to the gate, the carrier concentration varies in a so-called accumulation layer lying close to this surface. If n_i is the enhanced carrier density in the accumulation region, it is related to *n,* the carrier density in the bulk, through the surface potential (φ) by:

$$n = n_i exp(\frac{q\phi}{k_B T_C}) \tag{3.2.5}$$

where φ defines the difference between the Fermi levels of the semiconductor in these two regions and T_C is the characteristic temperature associated with the distribution of the traps (see expression 2.5.2.4 and 2.5.2.5).

Therefore, the current density can be expressed as:

$$J = qK\, n_i^{m+1} \left[exp\left(\frac{q\phi}{k_B T_C}\right) \right]^{m+1} F_x \tag{3.2.6}$$

Notice that equations 3.2.1 to 3.2.6 take the same steps as Raja & Eccleston's derivation, but here only an element, δI, of the total current in the accumulation region from an element δy of the cross-section in the y-direction, is considered. Raja & Eccleston's, equation. (30) can be written as:

$$\delta I = (W\delta y. q. K\, n_i^{m+1}) \left\{ exp(\frac{q\phi}{k_B T_C}) \right\}^{m+1} F_x \tag{3.2.7}$$

The scalar surface potential (Φ x,y,z) at the interface surface does not depend on the z-axis depth in the channel between source and drain. The consideration here in Φ thus reduces to the dimension of x and y only.

However, the derivatives with respect to x and y give the respective components of the electric field. A change in potential with respect to x is also accounted for by the F_x-term present in equation 3.2.7. Note that the sign of δI is dependent only on F_x; all other quantities are positive.

Let S represent the sign of $\frac{d\phi}{dy}$; the solution of Poisson's equation then gives:

$$F_Y = -\frac{d\phi}{dy} = -S\left[\left(\frac{2qn_i}{\varepsilon_o\varepsilon_s}\right)\left(\frac{k_BT_C}{q}\right)\right]^{1/2} \ exp(\frac{1}{2}\frac{q\phi}{k_BT_C}) \tag{3.2.8}$$

Clearly, when V_{GT} is positive, then $d\Phi/dy < 0$ for the situation shown in figure 3.1 and equation 3.2.8 is correctly written. However, when V_{GT} is negative, as may well be the case when studying OTFT's e.g. under transfer conditions, then $d\Phi/dy > 0$, and the RHS of equation 3.2.8 changes sign.

The accumulation layer is the thin layer of thickness Δ at the dielectric-organic semiconductor's interface, where carrier density is enhanced. For a small element dy

$$dy = \frac{+S.d\phi}{\left[\left(\frac{2n_ik_BT_C}{\varepsilon_o\varepsilon_s}\right)\right]^{1/2} \ exp(\frac{1}{2}\frac{q\phi}{k_BT_C})} \tag{3.2.9}$$

so that substituting in (3.2.7)

$$\delta I = \left[\left(\frac{+S.W.d\phi}{\left[\left(\frac{2n_ik_BT_C}{\varepsilon_o\varepsilon_s}\right)\right]^{1/2} \ exp(\frac{1}{2}\frac{q\phi}{k_BT_C})}\right)\right] qK \ n_i^{m+1} \left\{exp(\frac{q\phi}{k_BT_C})\right\}^{m+1} \tag{3.2.10}$$

which becomes:

$$\delta I = W \ . \ qK\left[\frac{\varepsilon_o\varepsilon_s}{2k_BT_C}\right]^{\frac{1}{2}}.(n_i)^{m+\frac{1}{2}} \quad . \ F_x.\left\{exp(\frac{1}{2}\frac{q\phi}{k_BT_C})\right\}^{2m+1} .S.\delta\phi \tag{3.2.11}$$

which can be integrated over the accumulation channel dimensions to give:

$$\int_{Y=0}^{Y=\Delta} dI = \left[W.q.K.(n_i)^{m+\frac{1}{2}}\right]\left[\frac{\varepsilon_o\varepsilon_s}{2k_BT_C}\right]^{\frac{1}{2}} F_x \int_{\phi=\phi_s}^{\phi=\phi_0} S \ exp\left[\frac{1}{2}\frac{q\phi}{k_BT_C}\right]^{2m+1} d\phi$$

$$\tag{3.2.12}$$

Here Δ is the extent along the y-axis of the accumulation region, Φ_s is the potential at the dielectric-semiconductor interface (y=0), and Φ_o is the potential just beyond the accumulation region. In what follows, a coarse approximation in which Δ has a finite cut-off and Φ_o is approximately that in the semiconductor bulk (y=∞) at zero transverse field.

The integration over dΦ becomes:

$$\int_{\phi_s}^{\phi_0} S \ exp\left[\frac{1}{2}\frac{q\phi}{k_B T_C}\right]^{2m+1} d\phi = -\frac{k_B T_C}{\left(m+\frac{1}{2}\right)q}\left[S \ exp\left(\left(m+\frac{1}{2}\right)\frac{q\phi_s}{k_B T_C}\right) - \right.$$
$$\left. S \ exp\left(\left(m+\frac{1}{2}\right)\frac{q\phi_0}{k_B T_C}\right)\right] \qquad (3.2.13)$$

The total current involves two terms:

$$I = I_{ch} - I_O \qquad (3.2.14)$$

where I_{ch} is the contribution from the accumulation channel, and I_0 is the normal bulk it replaces. The current of the element of bulk is:

$$I_0 = -S\left\{\left(\frac{W.K}{2m+1}\right)\left[\varepsilon_o \varepsilon_s \ 2k_B T_C\right]^{\frac{1}{2}}\left(n_i^{m+\frac{1}{2}}\right) \ F_x \ exp\left(\left(m+\frac{1}{2}\right)\frac{q\phi_0}{k_B T_C}\right)\right\} \qquad (3.2.15)$$

And the "accumulation" current at the interface is:

$$I_{ch} = -S\left\{\left(\frac{W.K}{2m+1}\right)\left[\varepsilon_o \varepsilon_s \ 2k_B T_C\right]^{\frac{1}{2}} \ n_i^{m+\frac{1}{2}} \ F_x \ exp\left[\left(m+\frac{1}{2}\right)\frac{q\phi_s}{k_B T_C}\right]\right\} \qquad (3.2.16)$$

The contribution from I_0 is considered negligible, so only the I_{ch} is considered further.

If Gauss's law is applied between the interface of the oxide and semiconductor, and the drain current is expressed in terms of applied voltages instead of the surface potential, then the drain current is expressed as follows:

$$\varepsilon_o \varepsilon_s F_Y = C_0(V_{GT} - V_x) \qquad (3.2.17)$$

Replacing F_Y by

$$F_Y = -S\left(\frac{2n_i k_B T_C}{\varepsilon_o \varepsilon_s}\right) \ exp(\frac{1}{2}\frac{q\phi}{k_B T_C}) \qquad (3.2.18)$$

Now taking account of the sign, S, and substituting in equation 3.2.17 this gives:

$$-S\left\{\varepsilon_0 \varepsilon_s \left[\left(\frac{2qn_i}{\varepsilon_o \varepsilon_s}\right)\left(\frac{k_B T_C}{q}\right)\right]^{1/2}\right\} exp(\frac{1}{2}\frac{q\phi}{k_B T_C}) = C_0(V_{GT} - V_x) \qquad (3.2.19)$$

$$\left\{ exp\left(\frac{1}{2}\frac{q\phi}{k_B T_C}\right) \right\} = -S \ \frac{C_0(V_{GT}-V_x)}{[2n_i\varepsilon_o\varepsilon_s k_B T_C]^{1/2}} \qquad (3.2.20)$$

and

$$\left[exp\left(\frac{1}{2}\frac{q\phi}{k_B T_C}\right)\right]^{(2m+1)} = \left[-S \ \frac{C_0(V_{GT}-V_x)}{[2n_i\varepsilon_o\varepsilon_s k_B T_C]^{1/2}}\right]^{(2m+1)} \qquad (3.2.21)$$

$$I_{ch} = -S\left\{\left[\left(\frac{WK}{2m+1}\right)[\varepsilon_o\varepsilon_s\ 2k_B T_C]^{\frac{1}{2}}\ n_i^{m+\frac{1}{2}}\right]\cdot\left[\left[-S\frac{C_0(V_{GT}-V_x)}{[2n_i\varepsilon_o\varepsilon_s k_B T_C]^{1/2}}\right]^{(2m+1)}\right]\right\}F_x$$

$$\qquad (3.2.22)$$

which simplifies to:

$$I_{ch} = -S\left\{\left(\frac{WK}{2m+1}\right)\right\}\left[\frac{C_0{}^{2m+1}}{[2\varepsilon_o\varepsilon_s k_B T_C]^m}\right]\ [-S(V_{GT}-V_x)]^{(2m+1)}F_x \qquad (3.2.23)$$

Remembering that V_x=0 at x=0 then F_x = dV_x/dx. Substituting in 3.2.23 obtains:

$$I_{ch} = \left\{-S\left[\left(\frac{WK}{2m+1}\right)\left[\frac{C_0{}^{2m+1}}{[2\varepsilon_o\varepsilon_s k_B T_C]^m}\right]\right][[-S(V_{GT}-V_x)]^{(2m+1)}]\right\}\frac{dV_x}{dx} \qquad (3.2.24)$$

Rearranging and integrating over the channel length:

$$\int_0^L I_{ch}dx = -S\left\{\left(\frac{WK}{2m+1}\right)\left(\frac{C_0^{2m+1}}{(2\varepsilon_o\varepsilon_s\ k_B T_C)^m}\right)\right\}\int_0^{V_{DS}}\{[-S(V_{GT}-V_x)]^{(2m+1)}\ \}dV_x$$

$$\qquad (3.2.25)$$

$$I_{DS}(L-0) = -S\left\{\left(\frac{WK}{2m+1}\right)\left(\frac{C_0^{2m+1}}{(2\varepsilon_o\varepsilon_s\ k_B T_C)^m}\right)\right\}\int_0^{V_{DS}}\{[-S(V_{GT}-V_x)]^{(2m+1)}\ \}dV_x$$

$$\qquad (3.2.26)$$

$$I_{DS} = -S\frac{1}{L}\left\{\left(\frac{WK}{2m+1}\right)\left(\frac{C_0^{2m+1}}{(2\varepsilon_o\varepsilon_s\ k_B T_C)^m}\right)\right\}\int_0^{V_{DS}}\{[-S(V_{GT}-V_x)]^{(2m+1)}\ \}dV_x$$

$$\qquad (3.2.27)$$

Linear regime

For n-type semiconductors where $V_{GT} \geq V_D \geq 0$, the limits of integration require S = –1. Remembering that S is the sign of dΦ/dy (equation.3.28), and that it is governed by (V_{GT} -V_x) through the Gauss equation 3.2.17,so that the expression for I_{DS} can be written:

$$I_{DS} = -S\left(\frac{W}{L}\right)\left\{\frac{KC_0^{2m+1}}{[2m+1][2\varepsilon_o\varepsilon_s\,k_BT_C]^m}\right\}\int_0^{V_{DS}}\{|(V_{GT} - V_x|)^{2m+1}\}\,dV_x \qquad (3.2.28)$$

Here, the absolute value | V_{GT}- V_x | now covers the general case (i.e. also p-type semiconductors with $0 \geqslant V_D \geqslant V_{GT}$ that –S (V_{GT}-V_x) is always positive. If this were not the case, there would be problems with non-integer exponents.

$$I_{DS} = -S\left(\frac{W}{L}\right)\left\{\frac{K\,C_0^{2m+1}}{(2m+1)[2\varepsilon_o\varepsilon_s\,k_BT_C]^m}\right\}.$$

$$\left[\frac{1}{2m+2}\{(|V_{GT}|)^{2m+2} - (|V_{GT} - V_{DS}|)^{2m+2}\}\right] \qquad (3.2.29)$$

since S=-1 for V_{GT} ≥ V_D ≥ 0, I_{DS} can be written as:

$$I_{DS} = \left(\frac{W}{L}\right)\left\{\frac{K\,C_0^{2m+1}}{(2m+1)(2m+2)[2\varepsilon_o\varepsilon_s\,k_BT_C]^m}\right\}\{(|V_{GT}|)^{2m+2} - (|V_{GT} - V_{DS}|)^{2m+2}\}$$

$$(3.2.30)$$

Alternatively, V_{GT} ≤ V_D ≤ 0, the limits of integration require S = +1, so that:

$$I_{DS} = -S\left(\frac{W}{L}\right)\left\{\frac{K\,C_0^{2m+1}}{[2m+1][2\varepsilon_o\varepsilon_s\,k_BT_C]^m}\right\}\int_0^{V_{DS}}\{(|V_{GT} - V_X|)^{2m+1}\}\,dV_x \qquad (3.2.31)$$

which gives:

$$I_{DS} = -\left(\frac{W}{L}\right)\frac{K\,C_0^{2m+1}}{(2m+1)(2m+2)[2\varepsilon_o\varepsilon_s\,k_BT_C]^m}\{(|V_{GT}|)^{2m+2} - (|V_{GT} - V_{DS}|)^{2m+2}\}$$

$$(3.2.32)$$

Both situations, i.e. V_{GT} ≥ V_D ≥ 0, or V_{GT} ≤ V_D ≤ 0 can be expressed succinctly in terms of the polarity of V_D as:

$$I_{DS} =$$

$$+\left(\frac{W}{L}\right)\frac{K\,C_0^{2m+1}}{(2m+1)(2m+2)[2\varepsilon_o\varepsilon_s\,k_BT_C]^m}\{(|V_{GT}|)^{2m+2} - (|V_{GT} - V_D|)^{2m+2}\}.\,sign(V_D)$$

$$(3.2.33)$$

$$K' = \left(\frac{W}{L}\right)\frac{K\,C_0^{2m+1}}{(2m+1)(2m+2)[2\varepsilon_o\varepsilon_s\,k_BT_C]^m} \qquad (3.2.34)$$

Saturation regime

We now consider the cases which occur in the saturation regime. Firstly, we define V_{GT}^0 to be the point at which $V_{DS} = V_{GT}$. This point is covered by the linear regime, so that the sign of I_{DS} is that of

V_{DS}. The explanation of the behaviour in the saturation regime is essentially an exercise in potential division, so the V_{DS} and I_{DS} sign relationship will be retained throughout this regime. Returning to equation (3.2.28):

$$I_{DS} = -S\left(\frac{W}{L}\right)\left\{\frac{KC_0^{2m+1}}{[2m+1][2\varepsilon_o\varepsilon_s\,k_BT_C]^m}\right\}\int_0^{V_{DS}}\{(|V_{GT} - V_x|)^{2m+1}\}\,dV_x \qquad (3.2.28)$$

The integration must be split into 2 parts 0 - V_{GT} and $V_{GT} - V_{DS}$:

$$I_{DS} = -S\left(\frac{W}{L}\right)\left\{\frac{K\,C_0^{2m+1}}{[2m+1][2\varepsilon_o\varepsilon_s\,k_BT_C]^m}\right\}\int_0^{V_{GT}}\{-S(|V_{GT} - V_x|)^{2m+1}\}\,dvx +$$

$$\int_{V_{GT}}^{V_{DS}}\{-S(|V_{GT} - V_x|)^{2m+1}\}\,dVx \qquad (3.2.35)$$

In figure 1(b), let R_0 = the bulk resistance of the material through the whole channel, and R_{ch} be the resistance of the surface conduction layer at the onset of saturation when $V_{DS}=V_{GT}{}^0$:

$$I_{DS} = \frac{V_{GT^O}}{\left(\frac{1}{R_0}\right)+\left(\frac{1}{R_{ch}}\right)} = \frac{V_{GT^O}.R_0.R_{ch}}{(R_0)+(R_{ch})} \qquad (3.2.36)$$

since in general R_0 is at least 2 orders of magnitude larger than $R_{ch.}$ and that portion of R_0 replaced by the accumulation channel, is neglected.

In fig. 1(c), with reference to the integration limits in equation. 3.2.28, when V_{DS} is increased to a multiple of $V_{GT}{}^0$, the carrier–density enhancement terminates at a point L-x where V_{DS} (L-x)/L = $V_{GT}{}^0$. x is determined by the potential drop, such that:

$$\frac{V_{GT^O}}{nV_{GT^O}} = \frac{\frac{L-X}{L}\left(\frac{R_0R_{ch}}{R_0+R_{ch}}\right)}{\left(\frac{L-X}{L}\right)\frac{R_0R_{ch}}{R_0+R_{ch}}+\left(\frac{X}{L}R_0\right)} \qquad (3.2.37)$$

where δ =x/L

$$\frac{1}{n} = \frac{(1-\delta)\left(\frac{R_0R_{ch}}{R_0+R_{ch}}\right)}{(1-\delta)\frac{R_0R_{ch}}{R_0+R_{ch}}+(\delta R_0)} \qquad (3.2.38)$$

and rearranging equation 3.2.38, n can be expressed in terms of δ as :

$$n = 1 + \frac{\delta}{(1-\delta)}\left[\frac{(R_0+R_{ch})}{R_{ch}}\right] \qquad (3.2.39)$$

so that

$$\delta = (n-1)\left[\frac{R_{ch}}{R_0 + nR_{ch}}\right]$$

(3.2.40)

Furthermore,

$$I_{DS} = \frac{nV_{GT^o}}{\left\{\left[(1-\delta)\left(\frac{R_0 R_{ch}}{R_0 + R_{ch}}\right)\right] + (\delta)R_0\right\}}$$

(3.2.41)

substituting for δ (equation 3.2.40) gives :

$$I_{DS} = \frac{\frac{V_{GT^o}}{R_{ch}}}{\left[\frac{R_O}{R_O + nR_{ch}}\right]}$$

(3.2.42)

which simplifies to :

$$I_{DS} = I_{DS}{}^{sat}\left(1 + n\left(\frac{R_{ch}}{R_O}\right)\right)$$

(3.2.43)

Thus, provided $R_0 \gg R_{ch}$ and $1 < n < 10$ then for $V_{DS} > V_{GT}{}^0$,

$$I_{DS} \approx I_{DS}{}^{sat}$$

(3.2.44)

Moreover, in the general case which includes n-type semiconductors, the sign of I_{DS} is still determined by Vd, so that in the saturation regime:

$$I_{DS} = K'\{|V_{GT}|\}^{2m+2} sign(V_{DS})$$

(3.2.45)

3.3 Contact resistances

Contact effects at the electrode materials is one of the factors that affect the transistor's performance by reducing essential electrical parameters such as overall charge transport and on/off ratio and increasing V_T. This makes the analysis of electrical measurements difficult. Ideally, field effect transistors require ohmic contact. However, organic based electrical devices have shown non-ohmic source contact and non-ohmic drain contact resistances i.e. electrode–semiconductor interfaces form a Schottky contact. This non-ohmic contact is due to the inefficient transfer of injected charge carriers from metal electrodes to semiconductors, and in the reverse sense.

Inefficient carrier injection causes trapped charge at the interface; in fact carriers are most likely to flow back into the metal [8]. According to Silveira et al., [30] those trapped charge carriers could be

caused by an image potential, a disordered interface, arising from dipoles during charge transfer, or interfacial chemistry [31].

Wang et al. examined top-contact pentacene TFTs with copper and gold electrodes and they found that contact resistances are lower in copper contact with pentacene than gold. It is known that gold has higher work function than copper [31]. Their conclusion was that the magnitude of contact resistance is mainly dominated by the trap distribution rather than a hole injection barrier at the metal/organic interface. They suggested the density of traps is most likely higher in the contact region as result of dense structural defects. The causes of such defects may include the presence of defects in the original surface of each material itself. Distortion and vacancy formation at the interface due to chemical reaction between the metal electrode and organic semiconductor, and also molecular polarization as result of image force, will cause defects. Contact resistance in gold/organic semiconductor interfaces will lower transport efficiency.

The inefficient charge injection discussed causes an energy barrier to transport between the semiconductor and metal electrode. Therefore, in order to overcome the barrier height the work function/Fermi level of the source and drain electrode has to be close the HOMO and LUMO level of the organic semiconductor in p–channel [32] and n-channel transistors respectively [8,32], However good energy level alignment is not the only factor that reduces contact resistance. For example, the formation of dipoles at the interface causes the alignment of the vacuum level to break [33]. If electrode deposition onto an organic layer is used, high temperatures may damage the organic uppermost layer and may also lead to metal atoms diffusing into the organic semiconductor layer.

3.3.1 Inclusion of contact resistances in the Modified Approach

From our re-tracing of Raja and Eccleston's model to include the sign information the key expressions for handling n-type semiconductors (equations 3.2.33 and 3.2 45), where sign(V_D) is +1 were:

LINEAR region $\qquad I_{DS} = +K'\{(V_{GT})^{2m+2}\} - \{(V_{GT} - V_D)^{2m+2}\}$ $\qquad$ (3.3.1)

SATURATION region $\qquad I_{DS} = +K'\{(V_{GT})^{2m+2}\}$ $\qquad\qquad$ (3.3.2)

where $\quad V_{GT} = V_G - V_T$

and $K' = + \left\{ \dfrac{(W/L)KC_O^{2m+1}}{(2m+1)(2m+2)(2\varepsilon_o \varepsilon_s k_B T_c)^m} \right\}$

Following Natali et al [8],

$$V_{GS} = V_G - I_{DS} R_S$$

$$V_{DS} = V_D - I_{DS} (R_D + R_S)$$

where V_G is the gate electrode potential relative to the source electrode, and V_{GS} the true potential of the gate relative to the source end of the accumulation layer. Likewise, V_D is the drain electrode potential relative to the source electrode and V_{DS} the true potential at the drain end of the accumulation layer.

Then in the linear and saturated regions, respectively, the expressions become:

$$I_{DS} = +K'. \{(|V_{GT} - I_{DS} R_S|)^{2m+2}\} - \{(|V_{GT} - V_D + (I_{DS} R_D)|)^{2m+2}\} sign(V_D)$$

(3.3.3)

$$I_{DS} = +K'. \{(|V_{GT} - I_{DS} R_S|)^{2m+2}\} sign(V_D)$$

(3.3.4)

It is important to realise that the eqns. (3.3.3) and (3.3.4) are identical for analysing p-type materials and n-type materials apart from the sign(V_D). For the moment, we consider n-type materials, where I_{DS}, $V_D > 0$ and sign (V_D) = +1, and in the linear region $V_{GT} > V_D$ by definition, and the corresponding expressions become:

$$I_{DS} = +K'. \{(V_{GT} - I_{DS} R_S)^{2m+2}\} - \left\{ \left(V_{GT} - V_D + (I_{DS} R_D) \right)^{2m+2} \right\}$$

(3.3.5)

$$I_{DS} = +K'. \left\{ (V_{GT})^{2m+2} \left(1 - \frac{I_{DS} R_S}{V_{GT}} \right)^{2m+2} \right\}$$

(3.3.6)

There are two ways to obtain a tractable correction for R_D, R_S effects. The first applies a Taylor expansion to first order, which would seem to require $I_D.R_S/V_{GT}$ and $I_D.R_D/(V_{GT}-V_D) \leq 0.1$. There are situations where this condition is not met. The alternative way makes use of the limited range of m; in our experience accurate extraction places m in the range $0 \leq m \leq 0.25$. This allows a special approximation to be applied which allows a much a wider range for R_S, R_D to be handled. In a working OTFT device it is expected that the total contact resistance is less than that of the working accumulation channel.

The second approach makes use of the approximation:

$$Y^{1+m} - X^{1+m} \approx (1+m)(Y\text{-}X)\left[\frac{1}{2}(Y+X)\right]^m \tag{3.3.7}$$

For m ≤ 0.25 and an extreme range 1000X ≤ Y ≤ 0, it is straightforward to show numerically that the error is ≤ 5%.

Identifying Y with $(V_{GT} - I_{DS}\,R_S)^2$ and X with V_{GT}^2 we obtain:

$$(V_{GT} - I_{DS}R_S)^{2+2m} \approx$$

$$V_{GT}{}^{2+2m} - \left\{(1+m)\left[V_{GT}{}^2 - (V_{GT} - I_{DS}R_S)^2\right]\left(V_{GT} - \frac{1}{2}I_{DS}R_S\right)^{2m}\right\}$$

$$= V_{GT}{}^{2+2m} - 2(1+m)\left(V_{GT} - \frac{1}{2}I_{DS}R_S\right)^{1+2m}I_{DS}R_S \tag{3.3.8}$$

Now identifying $X = V_{GT}$ and $Y = V_{GT} - \frac{1}{2}I_{DS}R_S$:

$$\left(V_{GT}\text{-}\frac{1}{2}I_{DS}R_S\right)^{1+2m} \approx V_{GT}{}^{1+2m}\text{-}\frac{1}{2}(1+2m)\left(V_{GT}\text{-}\frac{1}{4}I_{DS}R_S\right)^{2m}I_{DS}R_S \tag{3.3.9}$$

(Here, 2m ≤ 0.5, but the maximum error in using the approximation is still less than 6%)

Substituting (3.3.9) in (3.3.8) and truncating the progression to 2nd order in $I_D.R_S$

$$(V_{GT} - I_{DS}R_S)^{2+2m}$$

$$\approx V_{GT}{}^{2+2m} - \left[2(1+2m)(V_{GT}{}^{1+2m})(I_{DS}R_S)\right]$$

$$+ \left[(1+m)(1+2m)(I_{DS}R_S)^2\left(V_{GT} - \frac{1}{4}I_{DS}R_S\right)^{2m}\right]$$

$$= V_{GT}{}^{2+2m} - \left[2(1+m)(V_{GT}{}^{1+2m})(I_{DS}R_S)\right]$$

$$\tag{3.3.10}$$

Analogously,

$$(V_{GT} - V_D + I_{DS}R_D)^{2+2m}$$
$$\approx (V_{GT} - V_D)^{2+2m} + 2(1+m)(V_{GT} - V_D)^{1+2m}(I_{DS}R_D)$$

(3.3.11)

For the linear region:

$$I_{DS} \approx K'\{(V_{GT})^{2+2m} - (V_{GT} - V_D)^{1+2m}\}$$
$$-(2K' \ (1+m))\{R_S(V_{GT})^{1+2m} + R_D(V_{GT} - V_D)^{1+2m}\}I_{DS}$$
$$+ K'(1+m)(1+2m) \left\{ R_S{}^2 V_{GT}{}^{2m} + R_D{}^2 \ (V_{GT} - V_D)^{2m}\right\}I_{DS}{}^2$$

(3.3.12)

And by analogy for the saturated region:

$$I_{DS} = K'\{V_{GT}{}^{2+2m}\} - 2.\,K'(1+m)\left\{R_S V_{GT}^{(1+2m)}\right\}.\,I_{DS}$$
$$+K'(1+m)(1+2m)\{R_S{}^2(V_{GT})^{2m}\}I_{DS}{}^2 \qquad (3.3.13)$$

The symmetry in Ohmic contact requires that $R_D = R_S = R_{DS}/2$, so that the useful expression to correct for passive contact resistances becomes:

$$I_{DS} = K'\{V_{GT}{}^{2+2m} - (V_{GT} - V_D)^{2+2m}\}$$
$$-\{K'(1+m)(\ V_{GT}{}^{1+2m} + (V_{GT} - V_D)^{1+2m})\}R_{DS}I_{DS}$$
$$+\frac{1}{4}K'(1+m)(1+2m)\left\{(\ V_{GT}{}^{2m} + V_{GT} - V_D)^{2m}\right\} R_{DS}{}^2 I_{DS}{}^2 \qquad (3.3.14)$$

The last second order term amounts to ca.10% ($\sim$ ¼ $I_{DS} R_{DS} / V_D$) of the first order term in the worst case, so

$$I_{DS} \approx K'\{V_{GT}{}^{2+2m} - (V_{GT} - V_D)^{2+2m}\}$$
$$-\{K'(1+m)R_{DS}(\ V_{GT}{}^{1+2m} + (V_{GT} - V_D)^{1+2m})\}.\,I_{DS} \qquad (3.3.15)$$

Finally, collecting terms in I_D and rearranging:

$$I_{DS} \approx \frac{K'\{V_{GT}^{2+2m}-(V_{GT}-V_D)^{2+2m}\}}{\{1+K'(1+m)R_{DS}(\ V_{GT}^{1+2m}+(V_{GT}-V_D)^{1+2m})\}} \qquad (3.3.16)$$

By analogy, for the SATURATED region, starting from equation.(3.3.2):

$$I_{DS} \approx \frac{K'\{|V_{GT}|^{2+2m}\}}{\{1+K'(1+m)R_{DS}|V_{GT}|^{1+2m}\}} \qquad (3.3.17))$$

If the p-type materials are considered, I_D, $V_D \leq 0$ and $sign(V_D) = -1$, where now the linear region occurs for $|V_{GT}| \geq |V_D|$. To be comprehensive for both regions:

$$I_{DS} \approx \frac{K'\{|V_{GT}|^{2+2m}-(|V_{GT}-V_D|)^{2+2m}\}sign(V_D)}{1+K'(1+m)R_{DS}\{|V_{GT}|^{1+2m}+|V_{GT}-V_D|^{1+2m}\}} \qquad (3.3.18)$$

$$I_D \approx \frac{K'\{|V_{GT}|^{2+2m}\}sign(V_D)}{1+K'(1+m)R_{DS}|V_{GT}|^{1+2m}} \qquad (3.3.19)$$

for the linear and saturated regions, respectively.

3.3.2 Active contact resistance: Schottky effects

The expression in equation 3.3.12 and its analogue for the saturated region (equation 3.3.13) allows R_D and R_S to be different. The linear and saturated final expressions in this case become:

$$I_{DS} \approx \frac{K'\{V_{GT}^{2+2m}-(V_{GT}-V_D)^{2+2m}\}}{D}$$

where $\quad D = \left\{1 + 2K'(1+m)\left[R_S V_{GT}^{1+2m} + R_D(V_{GT} - V_D)^{1+2m}\right]\right\} \qquad (3.3.20)$

and

$$I_{DS} \approx \frac{K'V_{GT}^{2+2m}}{D}$$

where $\quad D = \left\{1 + 2K'(1+m)\left[R_S V_{GT}^{1+2m}\right]\right\} \qquad (3.3.21)$

In practice, it is worth mentioning that the denominator, D, should not exceed the value of 3 if an accurate extraction of m and K is to be obtained. This will be important when R_D or R_S becomes large relative to the resistance of the accumulation layer.

The DC performance characteristics in a situation where the contact resistance plays an non-Ohmic role must now be considered. It is necessary to consider how R_D and R_S independently behave when contact occurs. In this case the drain and source contacts have some Schottky diode character which

may be PN- or NP- type. The equivalent circuit needs to be modified in a way which allows a realistic behaviour, whilst introducing only one extra parameter relative to the 4-parameter "passive" resistance model. It is assumed at the outset that the template onto which the organic semiconductor is coated is symmetrical; R_D and R_S will be functions of the individual potential differences across the contact, and the direction of contact in one case will be the reverse of the other.

(a)

metal electrode

organic semiconductor

accumulation layer

metal-organic surface monolayer

(b)

V_D

R_B

D_d $R_O/2$ R_{ch} $R_O/2$ D_S

Drain

Source

V_1

Gate

V_2

$D_d = f(R_X, V_1)$

$D_S = f(R_X, V_2)$
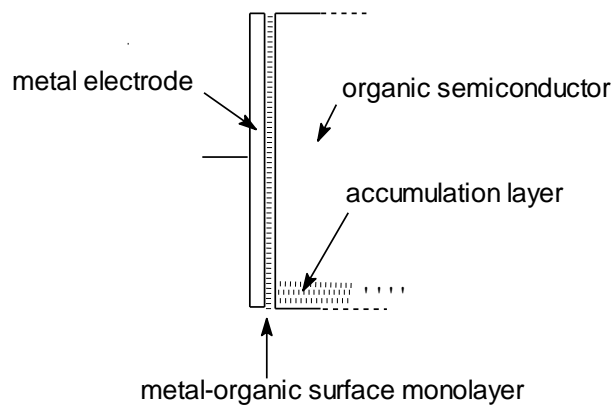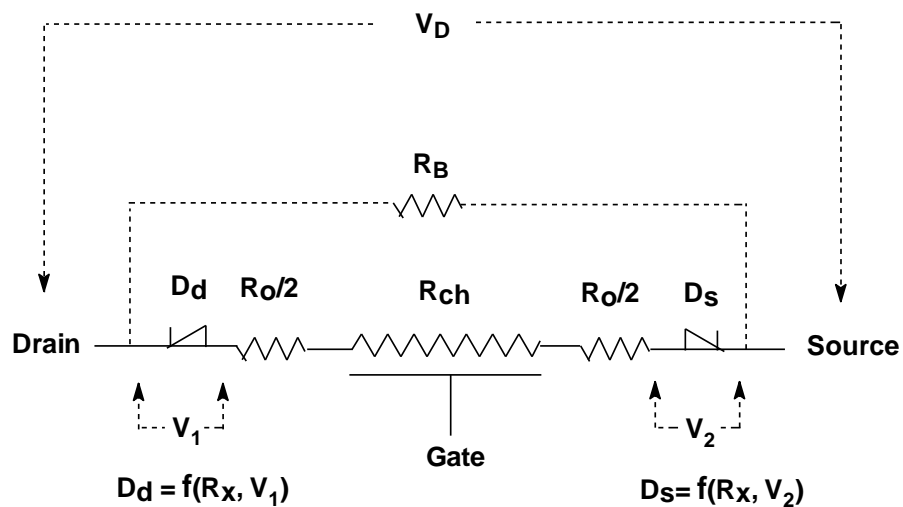
Figure 3.2. (a) The detail of the electrode – surface layer - semiconductor contact, (b) The symmetrical nature of the equivalent circuit, where one contact will have PN-sense, whilst the other will have NP-sense with respect to the voltage difference across each of them.

The contact of the metal electrode with the semiconductor is restricted to the point of contact with the accumulation layer, as indicated in figure 3.2 (a). The "bulk" contribution beyond this contact can be safely neglected. The following coarse assumption is made: the semiconductor in contact with a surface layer of the same material at the electrode presents a passive resistance contribution, since

their work functions will be similar, but the surface layer in contact with the metal – with a distinctly different work function – provides the active Schottky-like contribution. The equivalent circuit represented by: a passive part, $R_o/2$, and an active part, D_S or D_D, as shown in figure 3.2(b). Note that according to the relationship of the metal and semiconductor work functions, each diode may operate in the reverse sense to that shown.

Taken together, however, the series handling will be the same in both cases. D_X will represent the voltage-dependent diode resistance; R_U provides an effective upper limit. R_{ch} and R_{ds} take their conventional definitions.
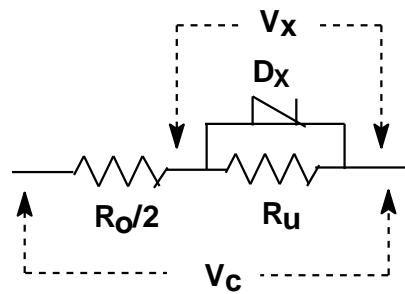
Figure 3.3. Contact junction details at e.g. the source electrode.

The current flowing in the potential chain including the 2 contacts and the accumulation channel will be I_{DS}. If D_X is the voltage-dependent resistance of the diode, then the (D_X, R_u) diode arm will have a resistance R_1 given by:

$$R_1 = \frac{R_U D_X}{R_U + D_X}$$
(3.3.22)

At one electrode (electrode 1) the voltage V_X across D_X will be given by:

$$V_1 = I_{DS} R_1$$
(3.3.23)

The diode offers a resistance given approximately by:

$$D_X = \frac{R_X \left[\frac{e}{k_B T}(+V_1) \right]}{\left\{ exp\left[\frac{e}{k_B T}(+V_1) \right] - 1 \right\}}$$
(3.3.24)

where the factor $e/k_B T$, assuming a temperature of 300K, has the value 38.68V^{-1}, and the ideality factor of the diode is assumed to be 1. By analogy at the other electrode (2), the reverse sense occurs:

$$R_2 = \frac{(R_U D_X')}{(R_U + D_X')}$$
(3.3.25)

$$V_2 = I_{DS} R_2$$
(3.3.26)

$$D_X' = \frac{R_X\left[\frac{e}{k_B T}(-V_2)\right]}{\left[\left(exp\frac{e}{k_B T}(-V_2)\right)-1\right]}$$

(3.3.27)

Ultimately, the two contacts will be treated as a series effect, so the symmetry of the situation does not require an absolute assignment of source or drain electrodes here. R_X is the additional diode parameter (i.e. 5th parameter) that characterises the Schottky effect to be fit by the model. Considering (3.3.24), the effective resistance of the junction represented in figure 3.3 becomes (R_O/2) + R_1, and at the opposite electrode (R_O/2) + R_2. Taken together, the total contact resistance R_{DS} = (R_D + R_S) is given by:

$$R_{DS} = R_0 + R_1 + R_2$$

(3.3.28)

If either D_X or D_X' becomes infinite, R_U serves to realistically limit the effect; this has been realistically set to 100.R_x. The parameter R_X is the effective resistance of each diode as V_1, $V_2 \rightarrow 0$. In practice, the modelling must proceed in two steps. The first calculates I_{DS} by estimating a passive R_{DS} to establish initial values of V_1 and V_2 according to (3.3.23, 3.3.26). The second step recalculates I_{DS} with the calculated diode effects and this is repeated to obtain self-consistency. (Generally, 2 iterations are sufficient.V_1, V_2 are typically 1 to 2 volts maximum.) The situation described makes a choice that a forward-going junction occurs at one of the electrodes. This is determined by metal and semiconductor work functions; the opposite choice can be selected by simply reversing the signs in front of V_1 and V_2 in the expressions 3.3.24 and 3.3.27.

3.4 Bulk resistance correction

One correction is found to be important when modelling output data. The bulk material beyond the accumulation layer has a finite resistance, R_B, shown in fig. 3.2(b). It is typically more than 2 orders of magnitude greater than the value of R_{DS} discussed in §3.3; thus additional contact resistance contributions are insignificant. In transfer experiments, where V_D remains constant, this produces a small constant current contribution, and does not affect the determination of the 5 key parameters: K', V_T, m, R_O and R_X. In output experiments, V_D is swept whilst V_G is kept constant, and this produces a varying, but small, additive contribution (ΔI_{DS}) to I_{DS}.

$$\Delta I_{DS} = \frac{V_D}{R_B}$$

(3.4.1)

R_B can be considered as a 6th parameter in the fitting process.

References

[1] Hamilton, M.C., Martin, S. and Kanicki, J. (2004) 'Field-effect mobility of organic polymer thin-film transistors ' *Chem. Mater.*, **16**(**23**), **4699**, doi: 10.1021/cm049613r.

[2]Shea,P.B.,Kanicki,J.and Ono, N. (2005) 'Field-effect mobility of polycrystalline tetrabenzoporphyrin thin-film transistors', *J. Appl. Phys.*, **98**(**1**), **014503**, doi: 10.1063/1.1949713.

[3] Wang, S. D.,Minari, T., Miyadera, T., et al. (2007) 'Contact-metal dependent current injection in pentacene thin-film transistors' *Appl. Phys. Lett.*, **91**(**20**),**203508**-**3**,doi: 10.1063/1.2813640.

[4] Tsung, K. K. and So, S. K. (2009) 'Advantages of admittance spectroscopy over time-of-flight technique for studying dispersive charge transport in an organic semiconductor ', *J. Appl. Phys.*, **106** (**8**), **083710**, doi: 10.1063/1.3251409.

[5] Liu, C., Huang, K., Park, Won-Tae., et al. (2017) 'A unified understanding of charge transport in organic semiconductors: the importance of attenuated delocalization for the carriers', *Mater. Horizons*, **4**(**4**), **608**, doi: 10.1039/c7mh00091j.

[6] Vissenberg, M.C.J.M and Matters, M. (1998) 'Theory of the field-effect mobility in amorphous organic transistors', *Phys. Rev. B*, **57** (**20**), **12964**, doi: 10.1103/PhysRevB.57.12964.

[7] Raja,M. and Eccleston,B. (2012) 'Analytical device models for disordered organic Schottky diodes and thin-film transistors for circuit simulations', *IET circuits devices & systems*,**6**(**2**),**122**,doi: 10.1049/iet-cds.2011.0199.

[8] Natali,D., Fumagalli,L. and Sampietro.M. (2007) 'Modeling of organic thin film transistors: effect of contact resistances', J.Appl.Phys, **101**(**1**),**04501,** doi: 10.1063/1.2402349.

[9] Horowitz, G., Hajlaoui, M.E., Hajlaoui, R. (2000) 'Temperature and gate voltage dependence of hole mobility in polycrystalline oligothiophene thin film transistors', *J. Appl. Phys.*, (**87**)**9**, **4456**-**4463**, doi: 10.1063/1.373091.

[10] Vissenberg, M. C. J. M. and Matters, M. (1998) 'Theory of the field-effect mobility in amorphous organic transistors', *Phys. Rev. B*, (**57**) **20**, **12964**-**12967**, doi: 10.1103/PhysRevB.57.12964.

[11]Fadlallah,M. et al. (2006) 'modelling and characterization of organic thin film transistors for circuit design', *J. Appl. Phys.*, **99**(**10**),**104504**, doi: 10.1063/1.2197620.

[12]Estrada, A., Cerdeira, A., Puigdollers, J., et al. (2005) 'Accurate modeling and parameter extraction method for organic TFTs', *Solid-State Electron.*, **49**(**6**),**1009**, doi: 10.1016/j.sse.2005.02.004.

[13] Cerdeira, A., Estrada, M., Garcia, R., et al. (2001) 'New procedure for the extraction of basic a-Si:H TFT model parameters in the linear and saturation regions', *Solid-State Electron.*,**45**(**7**),**1077**,doi: 10.1016/S0038-1101(01)00143-5.

[14] Estrada, M., Mejia, I., Cerdeira, A., et al. (2008) 'Mobility model for compact device modeling of OTFTs made with different materials',*Solid-StateElectron.*,**52**(**5**),**787**,doi: 10.1016/j.sse.2007.11.007.

[15] Yingping ,C., Liwei ,S., Zhuoyu ,J.I., et al. (2011) 'Analytical model for the dispersion of sub-threshold current in organic thin-film transistors',*Semicond. Sci. Technol.*,**32**(**11**),**114004**, doi: 10.1088/1674-4926/32/11/114004.

[16] Cerdeira, A., Estrada, M., Iniguez, B., et al. (2004) 'Modeling and parameter extraction procedure for nanocrystalline TFTs', *Solid-State Electron.*, **48**(**1**),**103**, doi: 10.1016/S0038-1101(03)00267-3.

[17] Estrada, M., Cerdeira, A., Ortiz-Conde, A., et al. (2002) 'Extraction method for polycrystalline TFT above and below threshold model parameters',*Solid-State Electron.*, **46**(**2**), **2295**,doi: 10.1016/S0038-1101(02)00186-7.

[18] Resendiz, L., Estrada, M., and Cerdeira, A. (2003) 'New procedure for the extraction of a-Si : H TFTs model parameters in the subthreshold region',*Solid-StateElectron.*,**47**(**8**),**1351**, doi:org/10.1016/S0038-1101(03)00070-4.

[19]Estrada, M., Cerdeira, A., Ortiz-Conde, A., et al. (2002) 'Unified extraction method for amorphous and polycrystalline TFT above threshold model parameters', Fourth IEEE International Caracas Conference on Devices, Circuits and Systems, Aruba, April 17-19, 2002, pp. D013 – 1-6.

[20] Resendiz, L., Iniguez, B., Estrada, A., et al. (2004) 'New procedure for the extraction of AIMSpice level 15 a-Si:H TFT model parameters', ieee, Conference:24th International Conference on Microelectronics (MIEL 2004) ,2004, 291.

[21]Cerdeira, A., Estrada, M., Garcia, R., et al. (2001) 'New procedure for the extraction of AIMS pice level 15 a-Si:H TFT model parameters', IPN No. 2508, Apto. Postal 14-740, 07300 DF, México. E-mail: cerdeira@mail.cinvestav.mx, Laboratorio de Electrónica del Estado Sólido, Universidad Simón Bolívar, Apartado Postal 89000, Caracas 1080A, Venezuela. On sabbatical leave from Universidad Simón Bolívar.

[22] Nguyen, P.C. and Vu, T. T., 'CHFET Model Parameter Extraction Program' Top-Vu Technology', 2650-14th Street NW, Saint Paul, Minnesonta 55112,USA   651-633-5925,651-633-5934(FAX): tho@topvu.com,www.topvu.com,http://www.topvu.com/doc/chfetextraction_paper.pdf.

[23] Xie, Z., Abdou, M. S.A., Lu, X., et al. (1992) 'Electrical characteristics and photolytic tuning of poly(3-hexylthiophene) thin-film metal-insulator-semiconductor field-effect transistors (MISFETs)', *Can. J. Phys.*,**70**(**10**),**1171**, doi: 10.1139/p92-189.

[24] Shur, M., Fjeldly, T.A., Ytterdal, T., et al. (1992) 'Unified MOSFET model ', *Solid-State Electron.*, 35(**12**), **1795**, doi: 10.1016/0038-1101(92)90263-C.

[25]Necliudov, P.V., Shur, M.S., Gundlach, D.J., et al. (2000) 'Modeling of organic thin film transistors of different designs', *J. Appl. Phys.*,**88**(**11**), **6594**, doi: 10.1063/1.1323534.

[26] Baeseller, H. (1993) 'Charge transport in disordered organic photoconductors a Monte Carlo simulation', *Phys. Status Solidi B*, **175**(**1**),**15**-**56**, doi: 10.1002/pssb.2221750102.

[27] Fishchuk, I. I., Kadashchuk, A. K., Genoe, J., et al. (2010) 'Temperature dependence of the charge carrier mobility in disordered organic semiconductors at large carrier concentrations',*Phys. Rev. B*,**81**(**4**),**045202**,doi: 10.1103/PhysRevB.81.045202.

[28] Rani,V.,Sharma,A.,Kumar,P.,et al. (2017) 'Charge transport mechanism in copper phthalocyanine thin films with and without traps', *RSC Adv.*,(**7**)**86**, **54911**-**54919**, doi: 10.1039/c7ra08316e.

[29] Berliocchi, M., Manenti, M., Bolognesi, A., et al. (2004) 'Charge transport in pentacene and porphyrin-based organic thin film transistors', *Semicond. Sci. Technol.*,(**19**)**4**,**S354**-**S356**,doi: 10.1088/0268-1242/19/4/117.

[30] Wang,H., Liu,Z., Fai Lo,M., et al. (2010) 'Organic heterostructures in organic field-effect transistors', *NPG Asia Mater.*, **2**(**2**), **69**, doi: 10.1038/asiamat.2010.44.

[31] Wang, S. D., Minari, T., Miyadera, T., et al. (2007) 'Contact-metal dependent current injection in pentacene thin-film transistors', *Appl. Phys. Lett.*, **91** (**20**), **203508**3,doi: 10.1063/1.2813640.

[32] Singhl, Th. B., Sariciftci, N. S., et al. (2008) 'Organ ic Field-Effect Transistors: FromMaterials to DevicePhYsics', Handbook of Organic Electronics and Photonics, 3, pp.153-176., ISBN: 1-58883-098-5 Copyright o 2008.

[33] Kraus,M.,Richler, S., Opitz,A., et al.(2010)'High-mobility copper-phthalocyanine field-effect transistors with tetratetracontane passivation layer and organic metal contacts' ,*J. Appl. Phys.* , **107**(**9**), **094503**,doi: 10.1063/1.3354086.

4. ORGANIC SEMICONDUCTOR MATERIALS

In organic semiconductors the charge transport process is governed by the electronic structure of the individual molecules and their intermolecular interactions. However, discontinuity in the molecular stacking results in less crystallinity and creates energy barriers. Hole- and electron charge carriers do not then flow in an analogous way to band-like transport, but rather carriers hop between neighbouring molecules [1].

Phthalocyanine (Pc) is an organic semiconductor material; the molecular structure is made of a macrocyclic aromatic ring with alternating single and double bonds, and electrons in the out-of-plane π-orbitals become delocalised [2]. Between molecules of organic semiconductors in the solid state, the intermolecular interactions are due to weak Van der Waals forces [3]. Pc has various properties making it easily adapted to different applications [4]. However, it is a big challenge to produce an organic semiconductor device with Pc-derived materials since their nature, i.e. molecular alignment with long-range ordering, is difficult to control [5].

There are two common ways to modify this compound's physical and chemical properties: replacement of the two central hydrogen atoms with a central metal ion and/or substituting at positions 1-4, 8-11, 15-18 and 22-25 see Figure 4.1 [6].

It is very important to have a better knowledge of the structural and optical properties of metal Pc (MPc) layers in order to improve device performance. MPc's as thin layers and MPc's as single crystals have different optical and electrical properties. Optical absorption in thin layers will cause energy transfer or charge transfer between molecules [7]. Optical absorption by Pc's in the visible region [8] and other experiments show that high thermal and chemical stability is observed in the conversion of solar-to-electric energy using Pc's[9].
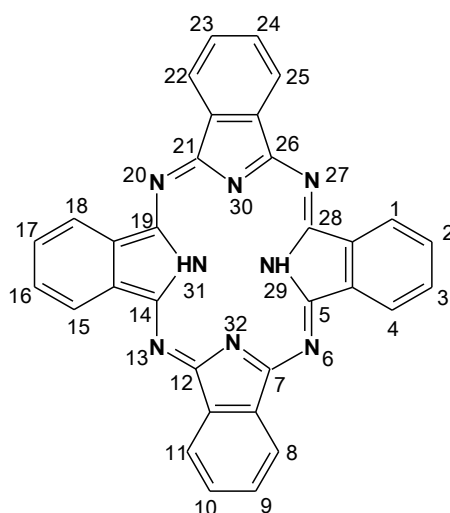

Figure 4.1. The basic molecular structure of metal free Pc and the IUPAC naming convention [13].

The planar structure in Pc is made of four isoindole units connected with four aza nitrogen atoms and two hydrogen atoms [10, 11]. Braun and Tcherniak were the first people who synthesized metal-free Pc (H_2Pc) in 1907] [12]. See Figure 4.1.

4.1 Metallophthalocyanines (MPc's)

MPc's where M = Zn, Cu, Ni etc have been investigated in detail since the early 20th century. In the case of MPc's, a single metal atom replaces the two central hydrogen atoms and due to their dative covalent bond make the compound more stable [14&15].
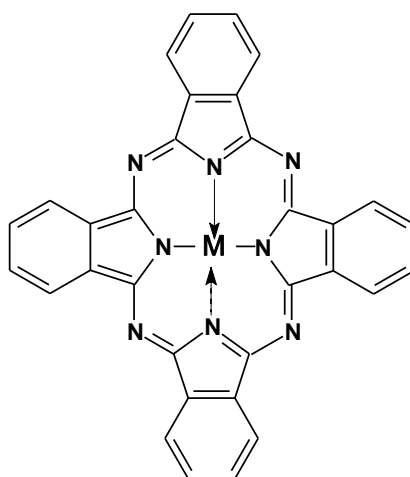
Figure 4.2. Phthalocyanine molecules with metal

Metal-substituted (M=Cu) Pc have been synthesised with excellent properties such as thermal stability and well-ordered thin film formation having a wide absorption band within the optical region [16, 17]. Work continued using the Robertson X-ray diffraction analysis to study both metal free and metal Pc's [17]; this contribution led to the improvement of Pc electrical conductivity properties, and inspired this field of research using Pc's.

Mono- and bis-MPc's are known, as well as syntheses of many layered MPc's including tris(phthalocyaninato) due to their extra pi-electron clouds and ambipolar behaviour [18, 19].

4.1.2 Mono-Pc

The most popular mono-Pc's for many device applications are zinc Pc (ZnPc) [20], copper Pc (CuPc) [21] and lead Pc (PbPc) [21, 22, 23]. The nature of the central metal ion affects the molecular orientation on a substrate, for example the non-planar structure of PbPc, where the central metal ion is out of the plane of the Pc ring. Its cone-shape results in poorly crystalline films. In addition, the molecules are not packed closely together in the solid state. The intermolecular interactions are weaker, indicating the molecular packing density has been lowered, compared with planar molecular structures, e.g. ZnPc and CuPc. Synthesizing 2-dimensional (2D) covalent organic frameworks

(COFs) using MPc's is one technique to enhance the carrier mobility. The Ding et al. group [24] successfully developed 2D MPc COFs such as CoPc-COF, CuPc-COF, and ZnPc-COF. Their work shows columns of π-macrocycles are the source of the conduction charge. Field-emission scanning electron microscopy shows the morphologies of ZnPc-COF are disc-like, but CuPc-COF are belt-like. Synthesizing MPc in 2D COF's improved the molecules' stacking and hence increased the absorption capability in the near-infrared and long wavelength visible regions [24, 25, 26].

4.1.3 Bis-Pc

Owing to the size of the metal ion, Gadolinium Pc (GdPc$_2$) forms a sandwich structure with 2 Pc macrocyclic rings. In GdPc$_2$ [27], two Pc rings are connected by one gadolinium metal ion and the typical liquid crystalline phase makes it more attractive for electrical devices although the bis-phthalocyanines (e.g. (Lu(PcR8)2[28) have extra π-π interactions, but their charge carrier mobilities in films are not high as mono-Pc's.

4.2 Ring substitution groups

Unsubstituted molecular and polymer semiconductors, like Pc's, are more likely to have rotational freedom and hence molecules can achieve a large crystalline domain[29]. Substituted alkyl chains in similar molecules influence the molecular packing in their crystal lattice. Although substituted organic semiconductor molecules can lead to increased rigidity, it can also cause the molecules to have good π-π stacking and improved charge transport. Substituted alkyl chain groups could make the molecules become more planar, and the probability is higher for the molecules to stack with their adjacent molecules directed to their centroids. However, much more rigid molecules can be less soluble and chemically unstable to the environment [29].

Substituting at ring positions 1-4, 8-11, 15-18 and/or 22-25 in PC's (see figure 1) make the molecule dissolve more easily in solvents, even in e.g. chloroform and water [30]. Alkyl (e.g. Octyl) are well known solubilizing substituents for Pc's[31]. Substituent groups can be placed at either peripheral (2,3,9,10,16,17,23,24) [32] or non-peripheral (1,4,8,11,15,18,22,25) [33] positions .

It is necessary to identify positions of substitution, where the substituent either increases or decreases the electron/hole mobility. Substitutions with electron-withdrawing groups can changes p-type into n-type organic semiconductors [34]. In addition the group may alter the original disc-like Pc molecule orientation [35], making the intermolecular distance larger, resulting in a smaller intermolecular overlap of the pi–electron orbitals. Hence the mobility of electronic charge carriers decreases. Finally, the substituent's chain length and size are factors that may alter the physical and chemical properties of the Pc material. It is believed that the substituent group, either non-peripheral or peripheral may hinder disc-like Pc molecules which can lead to alternative stacking in the crystalline structure. Additionally, non-peripheral substitutuents may alter the strong π-π stacking compared with peripheral substituents since the non-peripheral positions of substitution are nearer to the central core [35], although there is limited evidence at this stage.
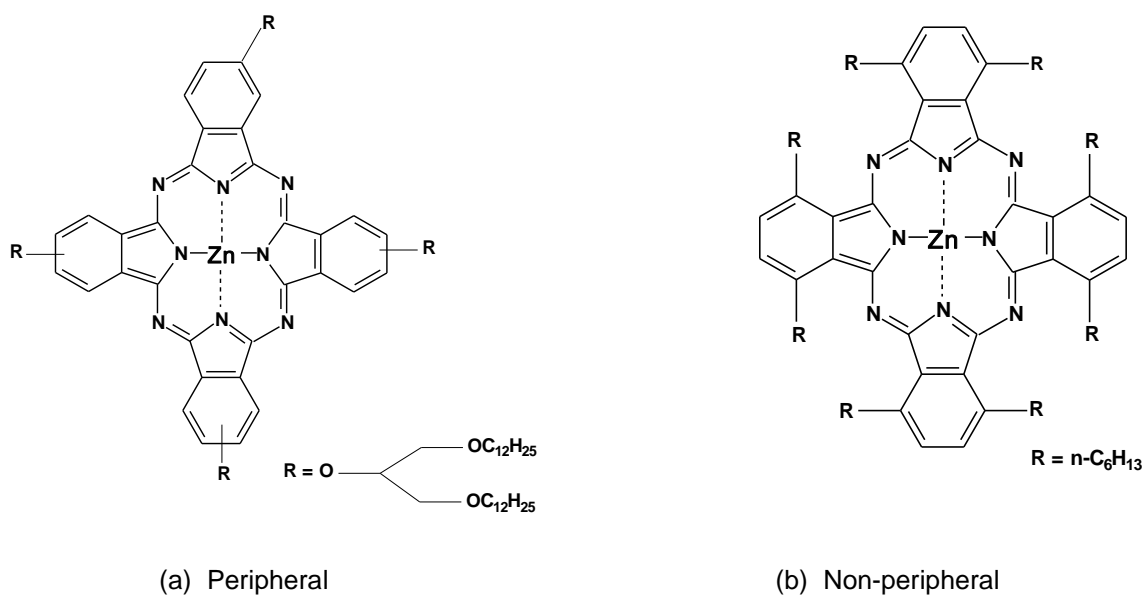
(a) Peripheral   (b) Non-peripheral

Figure:4.3. (a) Peripheral 2,9 (10) ,16 (17),23 (24)-(13,17-dioxanonacosane-15-oxy) phthalocyaninato Zinc (II) (ZnPcR$_4$) [32] and (b) non-peripheral (bay position) 1,4,8,11,15,18,22,25-octakis(hexyl)substituted phthalocyanines (ZnPc6) [33] .

Dong et al. [35] studied four non-peripheral substitution sites of tetrahexyl-substituted vanadyl Pcs. This group showed by experimental evidence that in all four cases the interplanar distances are similar to unsubstituted Pcs. Where only one out of four substituents is in a non-peripheral site, mobility is close to that for unsubstituted Pc's. This is because non-peripheral substituted sites on the *iso*-indole units overlap on intermolecular π-π stacking to one rather than two benzene rings. In addition to this, two-dimensional (2D) molecules are arranged perpendicular to the plane with π-π stacking [35].

They extended their studies by annealing four Pc films with substitution at different sites. After annealing, the mobility increased; one film improved by three orders of magnitude. AFM images were used to clearly attribute this to large domain size and better molecular orientation. Work has been carried out to improve the solubility of Pc molecules to enable the use of less expensive solvents. However, these modifications are detrimental to their electrical properties.

4.3 Molecular packing

The molecular structure of organic semiconductors has been studied vigorously to help understand their charge transport properties, with studies carried out by X-ray diffraction [36]. The phases of the materials are characterised by their X-ray diffraction pattern, and their performance in a device investigated by relating their electrical properties to their structures. Through knowing the crystalline structure, the solid-state properties are revealed. Analysis of their (or related) structures reveals the

important parameters, such as the overlap between the molecules, their twist, their dihedral angle (tilt) and their planarity [37, 38].

A single crystal is a benchmark in the study of crystal structure of any material due to the definite molecular ordering in their packing structure being defined. The interaction between the nearest molecules is assessed by the distance between the centres of adjacent molecules. In the case of MPc's the molecular interaction is dependent on distance between the adjacent metal ions of neighbouring Pc molecules. The smaller the stacking and sliding angle (see figure 4.4) between molecules the closer the molecules pack [38].
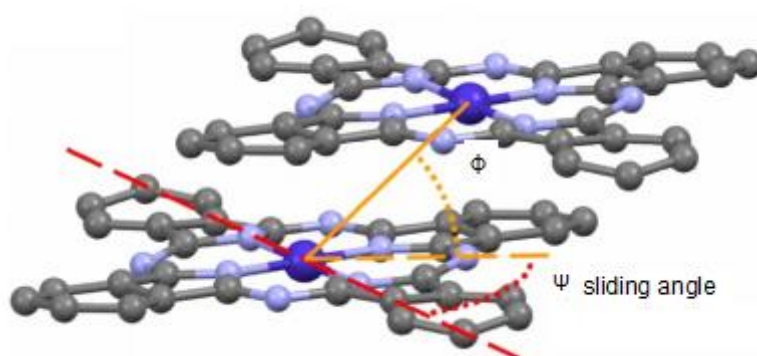
Figure 4.4. Stacking φ and sliding Ψ angles [38].

Pcs (and porphyrins) possess a large pi electron cloud above and below their ring structures. When these organic semiconductors overlap, charge transfer mechanisms are influenced. These mostly depend on the distance between neighbouring molecules and whether these atoms align, both of which can be assessed by measuring the intermolecular short contacts [39].

The degree of intermolecular interaction (electron coupling) is affected by multiple factors; some of these are: the total area of the electron cloud overlap, distance of the π-π stacking between molecules and the way molecules pack in crystal structures. There are various types of molecular packing, for example slipped pi-stacking, herringbone, bricklayer and other 2D pi-stacking motifs are well known molecular packing arrangements.
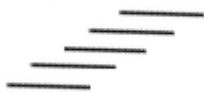
Figure 4.5. Slipped-pi-stacking [39].

In brick wall-like crystal packing the molecules have close-packed AB stacking.

 Figure 4.6. Brick wall-like crystal packing [39, 40].

The herringbone packing motifs are favourable for some molecular structures. The herringbone arranged molecules are packed in rectangular patterns within the layers; columns of molecules are inclined where the molecules in the column interact with their neighbours in both face–to–face and face–to–edge in vertical and horizontal directions, respectively. The face–to–face interaction is more desirable due to the potential to facilitate charge transport. The face–to–face molecular interactions are formed where the pi-ring of one molecule stacks cofacially with the nearby molecule's pi-rings, whereas face–to–edge stacks are formed via the interaction of the π–ring of one molecule with hydrogen atoms (CH-) of the adjacent molecules. This can manifest itself in a number of ways [41], see figure 4.7

The modes of this molecular packing depend on the molecular structure of a molecule and the optimisation of intermolecular of pi-electron interactions, which varies due to the molecular stacking arrangement. A perfect cofacial stacking is favoured where an electron rich molecule is superimposed (co-crystallised) on the top of another molecule which is electron deficient. Otherwise, electrostatic repulsion is likely to occur, thus tending to prevent perfect cofacial stacking.
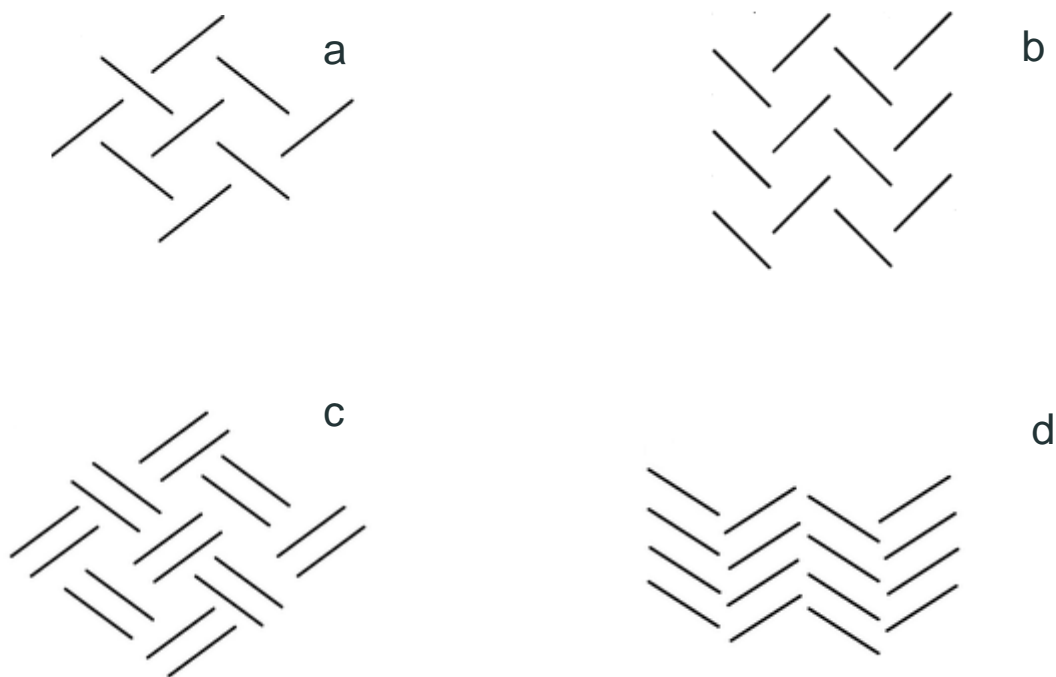
Figure 4.7. (a) Herringbone packing, (b) mono face–to–edge [42], (c) dimer face–to–edge molecular interactions [43] and (d) herringbone packing face–to–face molecular interactions.

The existence of electrostatic repulsion diminishes the intermolecular interaction between adjacent molecules. Molecular stacking with delocalisation of a molecule's π-electrons over long-range favours a charge carrier's mobility. This is because defects in the molecular structure tend to be reduced and the barrier to charge carrier propagation is removed [44].

4.4 Liquid crystal semiconductors

Pc's show liquid crystal (LC) semiconductor behaviour [45] and have been synthesized in ways which exhibit many different phases; the discotic liquid crystal (DLC) phase is one form of liquid crystalline material. Most DLC's are made up of flat and rigid aromatic cores [46]. Their molecular structure consists of disc-like molecules with flexible alkyl or alkoxy chains being substituted at their peripheral /non-peripheral positions, see figures 4.2 (a) and (b). These flexible alkyl or alkoxy chains contribute to extra delocalization of electron density and therefore improved MPc's conductivity [47, 48].

Examples of this class are aromatic hydrocarbons, macrocyclic cores, heterocyclic cores and metallomesogens. Pc's are one type of metallomesogen. Mesophases produced by disc-shaped molecules are mainly of three types: nematic, columnar and lamellar. Columnar mesophases in discotic liquid crystals are formed by strong π-π interactions in the polyaromatic cores [49].
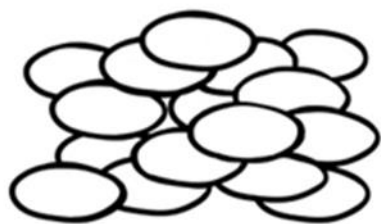
(a) Nematic-Discotic (N$_D$) (b) Nematic-Columnar (N$_{Col}$)

(c) Columnar Hexagonal (Col$_h$) (d) Columnar Rectangular (Col$_r$)

Figure 4.8.Discotic liquid crystal phases: (a) Nematic Discotic (N$_D$), (b) Nematic Columnar (N$_{Col}$), (c) columnar hexagonal (Col$_h$), and (d)columnar rectangular (Col$_r$)[49, 50].

As can be seen in Figure 4.9 (b), the separation distance between two neighbouring columns is much larger than the distance between two cores in the same column. Because of this, large overlaps of π-orbitals exist along the column's direction. The intermolecular overlapping of π-orbitals in π-conjugated systems determines the intermolecular interaction between the neighbouring molecules. The strength of the interaction depends on the number of pi-orbitals involves. Charge carrier migrations in then propagated along the direction of the strongest interaction, i.e.in the same column rather than between the neighbouring columns [51]. The interactions in DLCs also depend on the side chain length and the flexible long aliphatic chains that surround the core. As a result of these characteristics, a quasi-one-dimensional charge migration is expected in this type of material [51].

A long sequence of 2D conjugated cores within a DLC forms a column crystal–like molecular order by means of self-assembly. Commonly known highly-ordered discotic columnar phases are hexagonal and rectangular, all of which are 2D lattices. As shown in Figure 4.8 (c) a basic hexagonal columnar mesophase of flat disc-like molecules is stacked up in an organised manner to produce a discotic columnar mesophase [51].
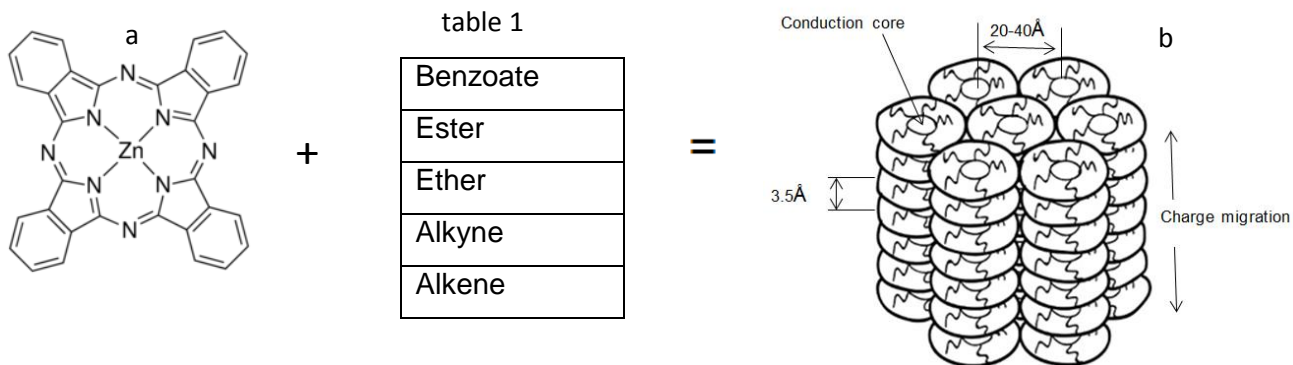
Figure 4.9. (a) ZnPc is a typical molecular structure, (b) a basic hexagonal columnar mesophase [51]. A list of side chain substituents in Pc's at Peripheral/ Non-peripheral positions is given in Table 4.1.

The 2D self-organized conjugate cores form stable columnar phase structures. This 2D lattice widens the organised delocalization area and may strengthen the intermolecular pi-pi interaction [51, 52].
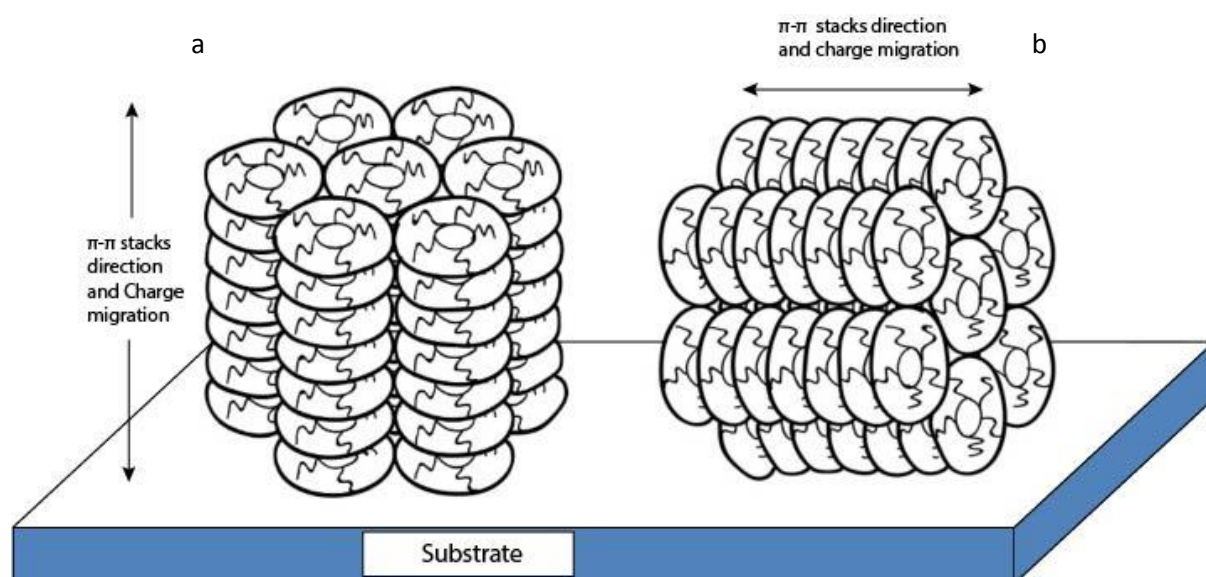
Figure 4.10. Columnar conduction core direction (a) Conduction core lying perpendicular to the substrate and (b) Conduction core lying parallel to the substrate [53].

As shown in figure 4.10, the π-π stacks can be face-on to the substrate, as in fig.4.10(a), or they can be edge-on to the substrate as in fig. 4.10 (b). In organic electronic devices, current flow is enhanced where injected carriers are directed face-on to the DLC's column. For this reason, the direction of DLC's columns perpendicular to the substrate are favoured for diode applications [53], whilst for transistor [53] applications it is argued that edge on to the substrate is preferred.

Different kinds of defects are commonly found in organic semiconductor materials; chemical impurity is a defect that causes structural defects and trapped charges. However, DLC's have the advantage

of liquid-like behaviour where structural defects at grain boundaries are more likely to heal [54]. An intrinsic amorphous organic semiconductor material can be annealed to improve its structural orientation causing the material to be less disordered. Pc's undergo different phase transitions as a result of annealing; ZnPcR$_4$ annealed at 70°C produces polycrystalline DLCs [55].

The field-independent mobility is one of the fundamental parameters revealing the conductivity of a device's active organic semiconductor layer, and is a measure of how fast charge carriers move through this material. The molecular packing arrangement of a material defines the intermolecular interaction (electronic coupling).This interaction, on which the rate of charge transfer depends, comprises the sum of the reorganisation energy and the electronic energy difference given by transfer integral [56,57]. The reorganisation energy is the difference in energy between the relaxed nuclear configuration, including the immediate surroundings, and the relaxed nucleus configuration of the final state, including the immediate surroundings, after transfer. The transfer integral is an electronic coupling between the initial and final electronic states of the charge transfer. It is given by an electron exchange interaction.

Therefore, identifying a mechanism that increases the transfer integral, which consequently speeds up the hopping rate, will increase carrier mobility and contribute to better device performance.

Organic thin film transistors with unsubstituted pentacene molecules with a herringbone packing arrangement exhibit a lower electrical mobility owing to edge-to-face interactions. In contrast, for thiophene-substituted pentacene molecules, the molecules lie in parallel face-to-face arrangements with maximum overlap of the aromatic ring. In the latter case, the pi-stacked columns provide cofacial stacking, and higher mobility, for the charge transport process [58].

Oh et al.[59] studied core-chlorinated naphthalene tetracarboxylic diimides (NDIs) with fluoroalkyl chains. Their n-type organic semiconductors' charge mobilities can be controlled by introducing chlorine atoms into the core region and fluoroalkyl side chains at the imide nitrogen. A tetrachlorinated NDI compound has slip-stacked face-to-face molecular packing. However, the dechlorinated compound has the slip-stacked edge-to-face herringbone stacking with high charge carrier mobility. This is attributed to the π-conjugated core being closely-packed with a high molecular packing density. Although chlorination lowers the LUMO level, itroducing two further chlorine substituents (tetrachlorinated) causes chemical instability in air. Therefore, it has been shown that NDI compounds show the best performance with an electron-withdrawing group comprising five fluoroalkyl side chains and dichlorination [59].

Senthilkumar et al. [60] studied discotic liquid crystals of unsubstituted triphenylene and alkoxy- and alkylthio-substituted triphenylene. These molecules behave in a similar way to Pc molecules where parallel overlap of the pi-rings and twist is important. The main contribution from these authors was to show that the charge transfer integral changes due to the alteration of twist angle and lateral slide distance between neighbouring molecules. The charge transfer integral is smallest for largest slide

distances. At zero twist angle the alkylthio substituted compound shows highest charge transfer. However, substituted alkoxy at a twist angle of 60° with respect to the adjacent molecule shows higher charge transfer compared with that for an alkylthio substitution [60].

Pc molecules are actively studied using their UV and visible absorption spectra because this information aids the interpretation of both conductivity and photoconductivity [61]. Such studies produce information about the energetics of their low-lying excited states through absorption wavelength, and through the magnitude of extinction coefficients, also the identities (n-π*, π-π*, etc.) of the states involved. Comparative studies in polar *vs.* non polar environments provide additional confirmation. Transition energies, extinction coefficients and absorption band widths together, allow transition moments to be estimated. These are important, because early experimental estimates of excited state splittings, and hence transfer integrals, relied on donor and acceptor transition moments and molecular separation [62].

Phthalocyanine molecules have four absorption bands Q, B (Soret), N and C. Q and B are the important low lying UV and visible bands which are assigned to π-π* transitions. The Q-band (500-800 nm range) occurs in the visible region, whilst the B-band (300-400 nm range) occurs in the UV region [63, 64]. In the Soret band region, the higher energy peak is assigned to an electron transition from pi to pi* orbitals [64]. In addition to this, charge transfer is attributed to the transition from an s-pz mixture to the macrocyclic ring of the Pc in the N- band [65].
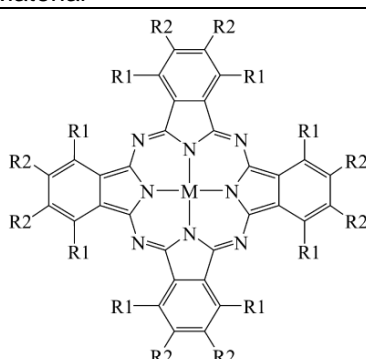
Studies show that the optical absorptions of an organic semiconductor layer are highly influenced by the layer thickness. Sathyamoorthy and Senthilarasu [66] demonstrated that the thickness of a Pc organic semiconductor layer alters the optical absorption, and in their work explain that optical band gap energy is reduced as the Pc film thickness increases. A similar effect was observed by Hussein et al. [67], where the maximum absorption peak for nickel phthalocyanine (NiPc) shifts towards the lower wavelength as film thickness was increased. They deduced that as film thickness increases, the typical crystallite size increases too. As a result, the stack length within the crystallite also increases. Well-known 'pack–of-cards' arguments in photophysics [62] show that the allowed transitions then move to shorter wavelengths. Seoudi et al. [68], has also mentioned that a thicker Pc film causes an increase in the Soret band absorbance. This suggests that the thicknesses of an organic semiconductor layer can influence the charge transfer integral, and hence the device material mobility.
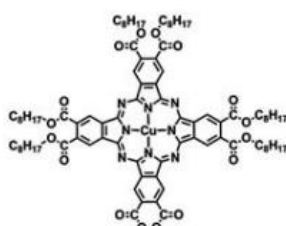
Nandu et al. [69] presented a UV-Visible optical absorption for annealed $ZnPcR_4$. Their results showed in the Q-band region, the 683 nm in chloroform solution was blue-shifted to 632nm and broadened in the annealed film which was attributed to stacking. In photochemistry, it is well-known [62] that the stack-of-cards arrangement in aggregates leads to allowed transitions to higher energy than for isolated molecules. Their research showed that the annealed Pc film had improved durability, stability and charge carrier mobility.
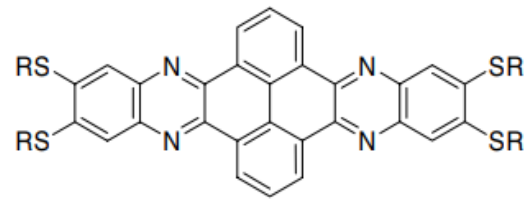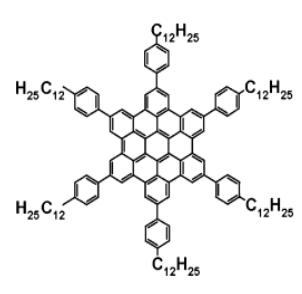
4.5 Other organic materials
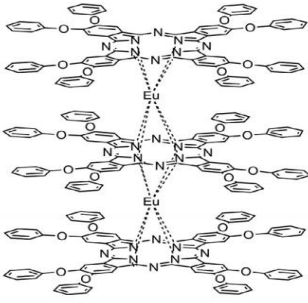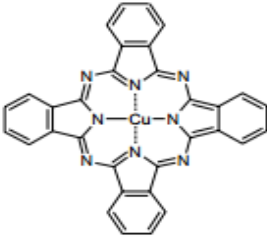
Broadly speaking, organic semiconductors are classified into two material groups: oligomers (small molecules) and conjugated polymers. These two classes of electroactive materials are increasingly interesting to science and technology as a result of their diverse applications. Conjugated polymers are types of conductive material where investigative work is difficult owing to their synthesis and purification processes. Their complex molecular structures and macroscopic ordering present other challenges with respect to molecular packing arrangements [70, 71]. Currently, the highest mobility cited for a conductive polymer (C_{60} needles) is found to be 11 $cm^2V^{-1}s^{-1}$ [72]. A steady progress is needed to attain higher conductivities needed. For this reason research has been directed to small molecules. They are the most researched materials in the organic semiconductor area because of their high electron and hole mobilities, good solubility in most organic solvents and the ability to design molecular structures which stack cofacially in their macroscopic phases. [70, 71, 73].

Small molecules and conjugated polymer materials may be characterised as n-type (see section 2.4.1), p-type (see section 2.4.2) or ambipolar semiconductors. In ambipolar organic semiconductors both electrons and holes are involved in transporting charges. In an n-type the majority charge carriers are electrons while those in p-type semiconductors are holes. Examples of p-type, n-type and ambipolar small molecules of DL semiconductor materials are listed below:

n-type Organic semiconductor			
Material	OTFTS	Mobility (cm^2 /Vs)	Reference
 $MPcF_{16}$ M=Cu,Zn,Fe,Co,Vo; R1=R2=F		0.03	[74]

\n\nCu[Pc(COOC8H17)8]		6.7×10^{-6} -1.6×10^{-4}	[75]

p-type Organic semiconductor		
Organic semiconductor	Mobility (cm^2 /Vs)	Reference
\n\nTQPP-[SR]$_4$\n\n**1a R = C$_{12}$H$_{25}$**	10^{-3}	[76]
\n\nHexa(4-dodecylphenyl)hexa-peri-hexabenzocoronene (HBC-PhC12)	6×10^{-4}	[77]

Ambipolar Organic semiconductor				
Material	OTFTS	Mobility (cm^2 /Vs)		Year /Ref
		μh	μe	
 Eu2(Pc)[Pc(OPh)8]2		1.9×10^{-2}	5.8×10^{-3}	[78]
 copper-phthalocyanine		0.0026	0.041	[79]

References

[1] Bassler, H. and Kohler, A. (2012) 'Charge Transport in Organic Semiconductors' , *Top Curr Chem*, **312**, **1**, Springer-Verlag Berlin Heidelberg, doi: 10.1007/128_2011_218.

[2] Davis, F. and Higson, S. P. J. (2011) 'Macrocycles: Construction, Chemistry and Nanotechnology Applications', United States, Wiley-Blackwell,John Wiley & Sons, Ltd, p:1-15, ISBN: 978-0-470-71462-1.

[3] Janiak,C. (2000) 'A critical account on π-π stacking in metal complexes with aromatic nitrogen-containing ligands', *Dalton Trans*., (**21**), **3885**, doi: 10.1039/b003010o.

[4] Melville,O., Lessard, B. H. and Bender, T. P. (2015) 'Phthalocyanine based organic thin-film transistors: a review of recent advances', *ACS Appl. Mater. Interfaces*, **7**(**24**),**1310**, doi: 10.1021/acsami.5b01718.

[5] Kinder, L., Kanicki, J. and Petroff, P. (2004) 'Structural ordering and enhanced carrier mobility in organic polymer thin film transistors', *Synth. Met.*, **146**(**2**),**181**, doi:10.1016/j.synthmet.2004.06.024.

[6] Merritt, J.E. and Loening K. L. (1980) 'UPAC-IUB Joint Commission on Biochemical Nomenclature (JCBN)-Nomenclature of Tetrapyrroles - Recommendations 1978',*Eur. J. Biochem.*,**108**(**1**),**1**-**30**, doi: 10.1111/j.1432-1033.1980.tb04691.x.

[7] EL-Nahass, M.M., Farid, A.M., Attia, A.A., and Ali, H.A.M. (2006) 'Structural properties and UV to NIR absorption spectra of metal-free phthalocyanine (H2Pc) thin films', *Fizika A*, **3**,1**47-164**.

[8]Gomez, A.R.,Sanchez-Hernandez,C.M., et al.(2014)'Optical absorptionand visible photoluminescence from thin films of silicon phthalocyanine derivatives', *Materials*, **7**(**9**),**6585**, doi:10.3390/ma7096585.

[9] Walter, M. G., Rudine, A. B. and Wamser, C. C. (2010) 'Porphyrins and phthalocyanines in solar photovoltaic cells', *J. Porphyr. Phthalocyanines*, **14**(**9**),**759**, doi: 10.1142/S1088424610002689.

[10] Engel, M. K. (1996) 'Single-Crystal and Solid-State Molecular Structures of Phthalocyanine Complexes', Kawamura Rikagaku Kenkyusho Hokoku, Vol:11-54, pp.1-52.

[11] Sakamoto,K.and Ohno-Okumura, E. (2009) 'Syntheses and Functional Properties of Phthalocyanines', *Materials*, **2**(**3**),**1127**, doi:10.3390/ma2031127.

[12] Rodríguez, L.A.G. and Kharisov, B.I. (2008) 'Pigmentos tipo ftalocianinas no sustituidas obtenciony propiedades',**40**(**38**),**1-10**, https://www.researchgate.net/publication/28203387.

[13] Moss,G.P. (1987) 'Nomenclature of tetrapyrroles', *Pure Appl. Chem.,***59**(**6**),**779-832**,doi: 10.1351/pac198759060779.

[14] Basova, T., Kol'tsov, E., Ray, A.K., et al. (2006) 'Liquid crystalline phthalocyanine spun films for organic vapour sensing', *Sens. Actuator B-Chem.*,**113**(**1**),**127**,doi: 10.1016/j.snb.2005.02.038.

[15]Benjamin,MM. and OLeckie, J. (1981) 'Multiple-site adsorption of Cd,Cu,Zn,and Pb on amorphous iron oxyhydroxide',*Adv.Colloid.Interface.Sci.*,**79**(**1**),**209**,doi.org/10.1016/0021-9797(81)90063-1.

[16]Herbst,W. and Hunger,K. (2004) 'Industrial organic pigments: production, properties, applications, 3rd edition', wiley-vch verlag gmbh & co. kgaa, weinheim , Germany, p:423-425, ISBN: 978-3-527-60406-7.

[17] Bekaroglu,O. (1996) ' Phthalocyanines containing macrocycles', *Appl. Organomet. Chem.*,**10**(**8**), **605**, doi: 10.1002/(SICI)1099-0739(199610)10:8<605::AID-AOC527>3.0.CO;2-U.

[18] Asatkar, A. K., Bedi, A. and Zade, S. S. (2014) 'Metallo-organic conjugated systems for organic electronics '*, Isr. J. Chem.*, **54**(**5**),**467**, doi: 10.1002/ijch.201400023.

[19] Kong, X., Zhang, X., Gao, D., et al. (2015) 'Air-stable ambipolar field-effect transistor based on a solution-processed octanaphthoxy-substituted tris(phthalocyaninato) europium semiconductor with high and balanced carrier mobilities', *Chem. Sci.*, **6**(**3**),**1967**, doi: 10.1039/c4sc03492a.

[20] Senthilarasu, S., Sathyamoorthy, R., Lalitha, S., et al. (2005) 'Space charge limited current conduction in zincPhthalocyanine (ZnPc) thin films', *Solid-State Electron.*,**49**(**5**),**813**,doi: 10.1016/j.sse.2005.01.007.

[21] Sivamalar, S. , Shanthi, J., Kalugasalam, P. (2013) 'Comparison of photoconduction property of Pbpc and Cupc thin films', *International Journal of Engineering Research and Development*, **5**(**8**),**75-80**, e-ISSN: 2278-067X, p-ISSN : 2278-800X.

[22] Liu,Y., Zhang,F. and Wang,J. (2013) 'Organic Photovoltaic Cells Based on PbPc Nanocolumns Prepared by Glancing Angle Deposition',*Int.J.Photoenergy*, No: **346818**,doi.org/10.1155/2013/346818.

[23] Kalugasalam, P. and Ganesan, S. (2010) 'Optical Properties of Moclinic and Triclinic Lead Phthalocyanine Thin Films', *Int. J. Energy Res*, **2**(**3**), **149**,http://www.irphouse.com.

[24] Ding,X., Feng,X., Saeki, A., et al. (2012) 'Conducting metallophthalocyanine 2D covalent organic frameworks: the role of central metals in controlling p-electronic functions', *Chem. Commun.*, **48**(**71**),**8952**, doi: 10.1039/c2cc33929c.

[25] Feng,X., Ding,X., Chen,L., et al. (2016) 'Two-dimensional artificial light-harvesting antennae with predesigned high-order structure and robust photosensitising activity', *Sci. Rep.*,**6**(**32944**), **1**, doi: 10.1038/srep32944, www.nature.com/scientificreports.

[26]Mandal,A.K.,Mahmood, J. and Baek, J-B. (2017) 'Two-Dimensional Covalent Organic Frameworks for Optoelectronics and Energy Storage', *chemnanomat*,**3**(**6**),**373**,doi: 10.1002/cnma.201700048.

[27]Huang,C.,Zhang,Y.and Sun, J., et al. (2013) 'Bis/tris[octakis(hexylthio)phthalocyaninato] europium(III) complexes: structure, spectroscopic, and electrochemical properties', *J.Porphyr. Phthalocyanines*, **17**(**8**),**673**, doi: 10.1142/S1088424612501465.

[28] Chaure, N. B., Basova, T., Ray, A. K., et al. (2009) 'Memory effects in thin film organic transistor characteristics' ,*J. Phys. D* , **42**(**12**),**1**, doi:10.1088/0022-3727/42/12/125103.

[29] Fong, H. H., Pozdin, V., Amassian, A., et al. (2008) 'Tetrathienoacene copolymers as high mobility, soluble organic semiconductors', *Acc. Chem. Res.*, **130**(**40**),**13202**, doi: 10.1021/ja804872x.

[30] Nemykin, V. N. and Lukyanets, E. A. (2010) 'Synthesis of substituted phthalocyanines', *Arkivoc*, Part: 1, Special Issue: SI, PP:136-208.

[31] Melville, O. A., Lessard, B. H. and Bender, T. P. (2015) ' Phthalocyanine-Based Organic Thin-Film Transistors: A Review of Recent Advances', *ACS Appl. Mater. Interfaces.*, **7**(**24**), **13105** , doi: 10.1021/acsami.5b01718.

[32] Jimenez Tejada, J.A., Awawdeh, K M.,et al. (2011) 'Contact effects in compact models of organic thin film transistors: Application to zinc phthalocyanine-based transistors', *Org Electron* ,**12**(**5**), **832**, doi: 10.1016/j.orgel.2011.02.010.

[33] Chaure, N.B., Barard, S., Ray, A. K., et al. (2013) 'Ambipolar charge transport in non-peripherally substituted octahexyl zinc phthalocyanine', *EPL*,**104**(**5**),**57005**, doi: 10.1209/0295-5075/104/57005.

[34] Matumoto,A.,Hoshino, N., Akutagawa, T., et al. (2017) 'N-Type Semiconducting Behavior of Copper Octafluorophthalocyanine in an Organic Field-Effect Transistor',*Appl.Sci.,* **7**(**11**),**1111**,doi:10.3390/app7111111.

[35]Dong,S., Tian,H., Huang, L., et al. (2011) 'Non-peripheral tetrahexyl-substituted vanadyl phthalocyanines with Intermolecular cofacial π–π stacking for solution-processed organic field-effect transistors', *Adv. Mater.,* **23**(**25**), **2850**, doi.org/10.1002/adma.201004776.

 [36] Jibo Z. et al. (2013) 'Remarkable fluorescence change based on the protonation–deprotonation control in organic crystals', *Chem. Commun.*, **49**(**37**), **3878**, doi: 10.1039/c3cc41171k.

[37] Senthilkumar, K., Grozema, F. C., Bickelhaupt, F. M. et al. (2003) 'Charge transport in columnar stacked triphenylenes: effects of conformational fluctuations on charge transfer integrals and site energies', *J. Chem. Phys.*, **119**(**18**),**9809**, doi: 10.1063/1.1615476.

[38] Serri, M., Wu, W.,Fleet, LR., et al. (2014) 'High-temperature antiferromagnetism in molecular semiconductor thin films and nanostructures', *Nat. Commun.* **5**(**3079**),**1-9**, doi: 10.1038/ncomms4079.

[39] He, T.,Stolte, M., Burschka, C.,et al. (2015) 'Single-crystal field-effect transistors of new Cl-2-NDI polymorph processed by sublimation in air', *Nat.Commun.*, **6**(**5954**),**1**, doi: 10.1038/ncomms6954.

[40] Kirsch,P.,Tong,Q.and Untenecker,H. (2013) 'Crystal design using multipolar electrostatic interactions: A concept study for organic electronics', *Beilstein J. Org. Chem.*,**9**,**2367**-**2373**, doi:10.3762/bjoc.9.272.

[41] Janiak, C. (2000) 'A critical account on π - π stacking in metal complexes with aromatic nitrogen-containing ligands', *Dalton Trans.*, **21**, **3885**-**3896**, doi: 10.1039/b003010o.

[42] Shrestha, B.B., Higashibayashi, S. and Akurai, H. (2014) 'Columnar/herringbone dual crystal packing of pyrenylsumanene and its photophysical properties', *Beilstein J. Org. Chem.*,**10**,**841**-**847** doi:10.3762/bjoc.10.80.

[43] Loots, L. and Barbour, L.J. (2012) 'A simple and robust method for the identification of π–π packing motifs of aromatic compounds', *CrystEngComm.*,**14**(**1**), **300**, doi: 10.1039/C1CE05763D.

[44] Coropceanu,V., Cornil,J., Da Silva Filho, D. A., et al. (2007) 'Charge transport in organic semiconductors', *Chem. Rev.*, **107**(**4**), **926**-**952**, doi:10.1021/cr050140x.

[45] Tsumura, A., Koezuka, H. and Ando,T. (1986) 'Macromolecular electronic device - field-effect transistor with a polythiophene thin-film', *Appl. Phys. Lett.*, **49** (**18**), **1210**-**1212**, doi: 10.1063/1.97417.

[46] Bushby, R.J. and Iozman, O.R. (2002) 'Discotic liquid crystals 25 years on', *Curr. Opin. Colloid Interface Sci.*, **7**,(**5-6**),**343**-**354**, doi: 10.1016/S1359-0294(02)00085-7.

[47] Deibel, C., Janssen, D., Heremans, P., et al. (2006) 'Charge transport properties of a metal-free phthalocyanine discotic liquid crystal',*Org.Electron.*,**7**(**6**),**495**-**499**, doi.org/10.1016/j.orgel.2006.07.002.

[48] Wang, Y., Liu, X., Shan, H., et al., (2017) 'Tetra-alkyl-substituted copper (II) phthalocyanines as dopant-free hole-transport layers for planar perovskite solar cells with enhanced open circuit voltage and stability', *Dyes Pigm.*,**139**, **619-626**, doi.org/10.1016/j.dyepig.2016.12.067.

[49] Tschierske, C.,Nuernberger, C., Ebert, H., et al. (2012) 'Complex tiling patterns in liquid crystals', *the Royal Soc.*, **2(5)**,**669-680**, doi:10.1098/rsfs.2011.0087.

[50] Bisoyi, H. and Kumar, S. (2010) 'Discotic nematic liquid crystals: science and technology', *Chem. Soc. Rev.*, **39(1)**,**264-285**, doi: 10.1039/b901792p.

[51] Kumar, S. (2006) 'Self-organization of disc-like molecules: chemical aspects', *Chem. Soc. Rev.*, **35 (1)**,**83-109**,doi: 10.1039/b506619k.

[52] Lin, X., Suzuki,M., Gushiken, M., et al. (2017) 'High-fidelity self-assembly pathways for hydrogen-bonding molecular semiconductors', *Sci. Rep.*,**7**,**43098**, doi: 10.1038/srep43098.

[53] Choudhury, T.D., Rao, N.V.S., Tenent, R.,et al.(2011) 'Homeotropic alignment and director structures in thin films of triphenylamine-based discotic liquid crystals controlled by supporting nanostructured substrates and surface confinement',*J.Phys.Chem.B*,**115(4)**,**609**,doi: 10.1021/jp106344f.

[54] Sergeyev, S., Pisula, W. and Geerts, Y. H. (2007) 'Discotic liquid crystals: a new generation of organic semiconductors', Chem*. Soc. Rev.*,**36(12)**,**1902**, doi: 10.1039/b417320c.

[55] Chaure, N-B., Basova, T., Zahedi, M. et al. (2010) 'Solution processed tetrasubstituted Zinc Phthalocynine as an active layer in organic field effect transistors', *J. Appl. Phys*, **107(11)**,**114503**, doi:10.1063/1.3428386.

[56] Newman, C.R., Frisbie, C.D., Da Silva, D.A., et al. (2004) 'Introduction to Organic Thin Film Transistors and Design of n-Channel Organic Semiconductors', *Chem. Mater.*, **16(23)**,**4436-4451**,doi: 10.1021/cm049391x.

[57] Dong, H. et al. (2013) '25th anniversary article: key points for high-mobility organic field-effect transistors', *J. Am. Chem. Soc.*, **25(43)**,**6158**-**6182**, doi:10.1002/adma.201302514.

[58] Miao, Q., Chi, X., Xiao, S. et al. (2006) 'Organization of acenes with a cruciform assembly motif', *J. Am. Chem. Soc.*, **128(4)**,**1340**, doi:10.1021/ja0570786.

[59] Oh, J H., Suraru, S-L., Lee, W-Y., et al. (2010) 'High-performance air-stable n-type organic transistors based on core-Chlorinated naphthalene tetracarboxylic diimides', *Adv. Funct. Mater.*, **20(13)**, **2148**, doi: 10.1002/adfm.201000425.

[60] Senthilkumar, K., Grozema, F.C., Bickelhaupt, F.M., et al (2003) 'Charge transport in columnar stacked triphenylenes: Effects of conformational fluctuations on charge transfer integrals and site energies', *J. Chem. Phys.*,**119(18)**, **9809**,doi: 10.1063/1.1615476.

[61] Jlali,A.,Jablaoui,C., Lahouel,M. and Jamoussi,B. (2016) 'New zinc (II) phthalocyanines substituents: synthesis, characterization, aggregation behavior, lectronic and antibacterial properties', *IJSR*,**5**(**6**),**1750**,doi.org/10.21275/v5i6.NOV164594.

[62] Becker, R. S. (1969) 'Theory and Interpretation of flourescence and phosphorescence', John Wiley Inc. New York, pp. 234-238, SBN 471 06126 3, and references therein.

[63] Nackiewicz, J, Suchan,A. and Kliber, M. (2014) 'Octacarboxyphthalocyanines - compounds of interesting spectral, photochemical and catalytic properties', Faculty of Chemistry, Opole University, Opole, Poland **68**, (**4**), **369**, https://www.researchgate.net/publication/288390469.

[64] Seoudi, R., El-Bahy, G. S. and El Sayed, Z. A. (2006) 'Ultraviolet and visible spectroscopic studies of phthalocyanine and its complexes thin films', *Opt.Mater.*,**29**(**2**),**304**,doi: 10.1016/j.optmat.2005.10.002.

[65] Wojdyla,M., Derkowska,B.,Lukasiak,Z.,et al. (2006) 'Absorption and photoreflectance spectroscopy of zinc plithalocyanine (ZnPc) thin films grown by thermal evaporation', *Mater. Lett.*, **60**(**29**),**3441**, doi: 10.1016/j.matlet.2006.03.029.

[66] Senthilarasu,S. and Sathyamoorthy, R. (2006) 'Effect of substrate temperature on the optical constants of zincphthalocyanine thin films', *Cryst. Res. Technol.*, **41**(**11**),**1136**,doi: 10.1002/crat.200610734.

[67] Sathyamoorthy,R. and Senthilarasu,S. (2006) 'Influence of RMS strain on optical band gap of ZincPhthalocyanine (ZnPc) thin films', *Solar Energy*,**80**(**2**),**201**-**208**, doi: 10.1016/j.solener.2005.06.005.

[68] Hussein,M.T.,Nasir,E.M.and Al-Aarajiy, A.H. (2012) 'Study on the UV-Visble of Ni-phthalocyanine thin film optical properties', *Int. J. Thin Film Sci. Tec.*, **1**(**2**),**71**-**76**, https://www.researchgate.net/publication/236621039.

[69] Chaure, N B., Basova, T., Zahedi, M., et al. (2010) 'Solution processed tetrasubstituted zinc phthalocyanine as an active layer in organic field effect transistors', *J.Appl. Phys.*,**107**(**11**),**114503**, doi: 10.1063/1.3428386.

[70] Dong,H.,Fu, X.,Liu,J., et al. (2013) '25th Anniversary article: key points for high-mobility organic field-effect transistors', *Adv. Mater.*,**25** (**43**), **6158**, doi: 10.1002/adma.201302514.

[71]Boughias,O.,Belkaid ,M.-S.,Nemmar,F. and Hatem,D. (2012) 'Organic transistors field effect performances', pp.1-3,Www.arpapress.com/Volumes/Vol12Issue2/IJRRAS_12_2_11.pdf.

[72] Li, H., Tee, B.C-K., et al. (2012) 'High-mobility field-effect transistors from large-area solution-grown aligned C-60 single crystals', *J. Am. Chem. Soc.*,**134(5)**, **2760-2765** ,doi: 10.1021/ja210430b.

[73] Mikroyannidis,J.A., Tsagkournos, D. V., Sharma, S. S., et al. (2010) 'Conjugated small molecules with broad absorption containing pyridine and pyran units: Synthesis and application for bulk heterojunction solar cells', *Org. Electron.*, **11**(**12**),**2045**, doi.org/10.1016/j.orgel.2010.10.002.

[74] Ling, M-M. and Bao, Z. (2006) 'Copper hexafluorophthalocyanine field-effect transistors with enhanced mobility by soft contact lamination', *Org.Electron.*,**7**(**6**),**568**, doi:10.1016/j.orgel.2006.09.003.

[75] Ma, P., Kan, J., Zhang, Y., et al. (2011) 'The first solution-processable n-type phthalocyaninato copper semiconductor:tuning the semiconducting nature via peripheral electron-withdrawing octyloxycarbonyl substituents' *J. Mater. Chem. A.*, **21**(46), **18552**, doi:10.1039/c1jm13082j.

[76] Kaafarani, B.R., Lucas, L.A., Wex, B. et al. (2007) 'Synthesis of novel pyrene discotic for potential electronic applications', *Tetrahedron Lett.*, **48**(**34**), **5995**, doi.org/10.1016/j.tetlet.2007.06.121.

[77] Shklyarevskiy, I.O., Jonkheijm, P. and Stutzmann, N., et al. (2005) 'High anisotropy of the field-effect transistor mobility in magnetically aligned discotic liquid-crystalline semiconductors',*J.Am. Chem. Soc.*, **127** (**46**), **16233**, doi: 10.1021/ja054694t.

[78] Kraus,M., Richler,S., Opitz,A., et al. (2010) 'High-mobility copper-phthalocyanine field-effect transistors with tetratetracontane passivation layer and organic metal contacts', *J. Appl. Phys.*, **107** (**9**), **094503**, doi: 10.1063/1.3354086.

[79] Li, D., Wang, H., Kan, J., et al. (2013) 'H-aggregation mode in triple-decker phthalocyaninato-europium semiconductors. Materials design for high-performance air-stable ambipolar organic thin film transistors', *Org. Electron.*,**14**(**10**), **2582**, doi: 10.1016/j.orgel.2013.07.003.

5.   CHARACTERISTICS OF METALLOPHTHALOCYANINE OTFT'S

This thesis focuses on the physical modelling of MPc-based organic thin film transistors. Organic MPc's were used as organic semiconductors to fabricate the bottom-gate-bottom-contact organic thin film transistors, the structure of which is shown in figure 5.1(a).This active p-type semiconductor layer was deposited on a previously prepared template. Gold, with an adhesive underlayer of titanium, was used for both the source and drain electrodes; the two electrodes, having the same width, W, and depth, Z, were separated by a channel length, L. The channel length, W, could be compactly increased by using an interdigitated electrode arrangement as shown in figure 5.1(b). In all the experiments discussed in chapter 5 and 6, the total channel width, was 1-10x the length of an individual "finger". Silicon oxide (SiO_2) was grown on an n-type silicon wafer substrate to obtain a dielectric gate. An octadecyltrichlorosilane (OTS) solvent was used in order to improve coating uniformity. The surface morphology of spin-coated MPc films was investigated at room temperature by using a Nanoscope IIIa atomic force microscope (AFM). Room temperature current-voltage (I-V) characteristics of the deposited and annealed MPc were obtained using a microprocessor- controlled Keithley 93 I-V instrument. The measurements were performed by Nandu et al., [1] and details of the experimental data and procedure for deposited and annealed $ZnPcR_4$ can be found in a previous publication [1]. The same procedure was used for the other samples described.

(a)

(b)
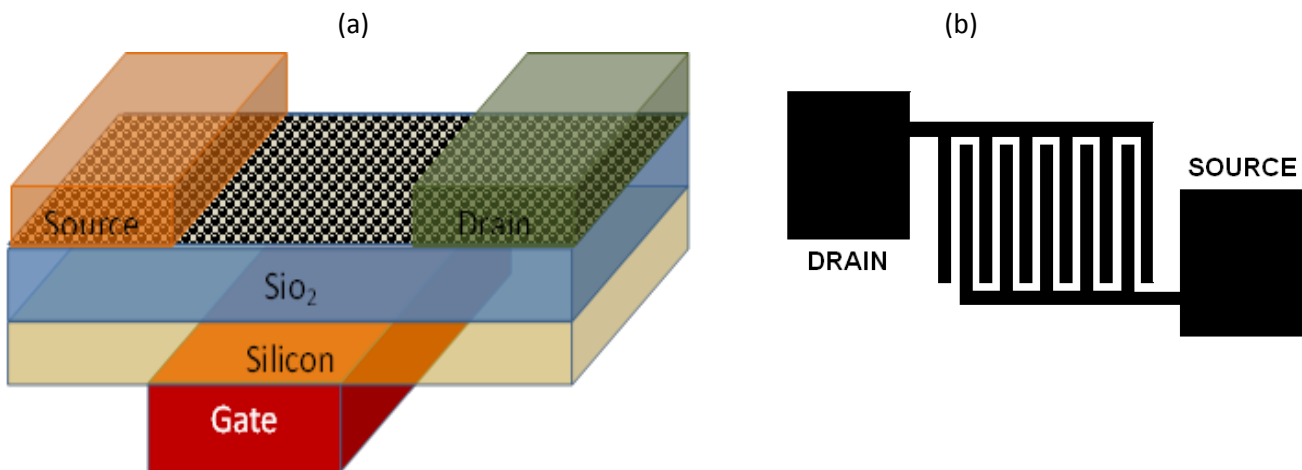
Figure 5.1. (a) Bottom-gate-bottom-contact $ZnPcR_4$ organic thin film transistor and (b) interdigitated electrode arrangement.

The flow of charge carriers in the accumulation channel between the source and the drain was analysed in Chapter 3. A statistical modelling procedure was described where an analytical simulation was performed to fit the experimental I-V data of the MPc OTFT's. An analytical model for disordered semiconductor materials, based on modified Raja and Eccleston equations [2] was first implemented to extract the device parameters modelling the OTFT behaviour. The important quantities

characterising the material: m, μ_o, T_C and NME, could then be deduced. The extracted device parameters can explain all the MPc semiconductor properties.

The modified analytical model for disordered materials here has the facility to simulate both the linear and saturation regions of either transfer or output measurements. In addition to this, the model has the ability to handle leakage current and bulk by-pass effects, as well as passive and Schottky-diode contact effects where these become significant.

Bottom-gate-bottom-contact transistors were fabricated as described in the first paragraph, and OTFT experimental data have been acquired using metallophthalocyanines incorporating four different metals. All transistors are listed below with the molecular structures of their active organic semiconductors. In the following section the electrical behaviour of these OTFT devices will be presented, and the comparison of mono- and bis metal-phthalocyanines with substitution at peripheral- or non-peripheral positions, used in the semiconductor layer, will be discussed.

5.1   Mono-Pc OTFT's

5.1.1 6CuPc and 6CuTBTAP

CuPc's are very stable and have the typically planar structure of a mono-Pc. These organic semiconductors, have been widely investigated in the past decades. An active 1,4,8,11,15,18,22,25-octakis(hexyl) copper phthalocyanine (CuPc6) semiconductor, the molecular structure of which is shown in figure 5.2 (a) and (b), was used to fabricate 6CuPc-OTFT's.

Figure 5.2. (a) Molecular structure of the active semiconducting material: 1,4,8,11,15,18,22,25-octakis(hexyl) copper phthalocyanine (6CuPc),and(b)Octahexyl-substituted copper tetrabenzotriazaporphyrin (6Cu-TBTAP) [3].

The alkyl substituents not only increase the π –π interaction between the molecules but also increase the hydrophobicity of the molecule, which lea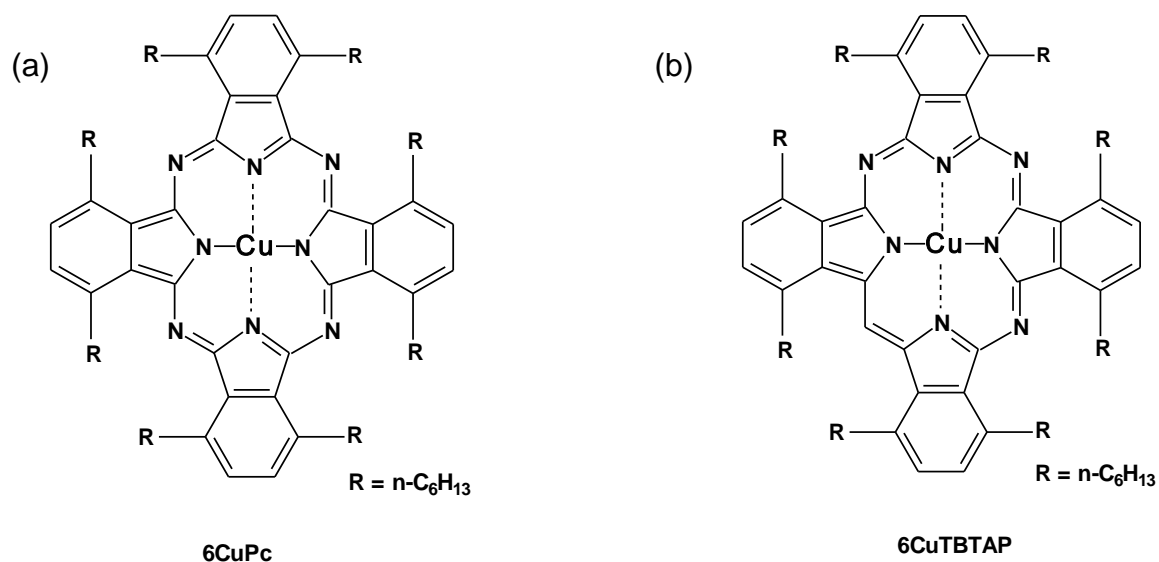ds to a reduction in wettability. A surface with more hydrophobicity is known to be more suitable for charge transfer [4].

The I-V characteristics were measured for each MPc-OTFT sample, as previously explained. For a 6CuPc-OTFT (W=1mm, L=5μm, C_i =10 nF cm^{-2})[5], as a negative voltage is applied between gate and source then a current starts to flow between source and drain in the channel region situated at the semiconductor-dielectric interface. In this device positive holes are the charge carriers when the device operates in the accumulation mode. Therefore, the drain current, I_{ds}, was measured from V_{GS} = +20 to -40V with a 2V step setting of V_{DS} = -5V for probing mostly the linear region, or V_{DS} =-40V, for mostly the saturation region.

Extraction method. The experimental I-V data of the 6CuPc-OTFT sample was fitted to the OTFT expressions developed in Chapter 3 by means of statistical modelling. The expressions provided by equations (3.3.18 & 19), (3.3.20 & 21) and (3.4.1) were used as the basis for the statistical modelling procedure. The basis for parameter optimisation was the cumulative improvement of the Coefficient of Determination, $\Re^2$ [6], towards its theoretical maximum value of 1. $\Re^2$ is an established statistical quantity whose purpose is to provide a measure of how well observed outcomes are replicated by a model and is the widely accepted function of choice for optimisation of hypothetical models[7,8]. There are several equivalent definitions; the computationally pragmatic choice is given by:

$$\Re^2 = 1 - \left\{ \sum (x_i^{expt} - x_i^{model})^2 / \sum (x_i^{expt} - x^{av})^2 \right\} \tag{5.1}$$

where x_i^{expt} and x_i^{model} are the experimental and modelled values of an observable x, $1 \leq i \leq n$, and x^{av} is the mean value:

$$x^{av} = (1/n) \sum x_i^{expt} \tag{5.2}$$

$\Re^2$ for the modelled- *vs.* experimental values of I_d as a function of V_{DS} or V_{GS} , were improved using a gradient ascent variation of the "steepest descents method" [9]. The functional search space of $\Re^2$ was maximised by calculating the vector derivative of this function to determine the ascent direction. Convergence of the process was monitored via the 1st and 2nd derivative of the $\Re^2$-sum with respect to iteration cycle. Careful stepping strategies allow lower local maxima in $\Re^2$ to be bypassed, as monitored by the derivatives on a cycle-by-cycle basis.

Since the stated aim is to extract parameters simultaneously using a statistical modelling technique, it is relevant to address the usual criticism of whether the solution obtained is unambiguous. Firstly, it should be noted that the criticism can be applied to *all* the extraction techniques so far applied in this area. Secondly, experience shows that ambiguous solutions only occur when (a) the fitting is over-parameterised, and (b) when the maximum of the multidimensional $\Re^2$ is particularly flat. In the first

case (a) this will occur when the number of relevant experimental data points is less than 3x the number of parameters being optimised. In the second case (b) is most likely to occur when the quantity D (equations 11 and 12) exceeds 3. A little algebra quickly reveals that the quantities K' and m become poorly determined.

This novel statistical modelling software was developed at the Brunel University London by Prof. Chris Winscom. The software has been extensively tested on real and hypothetical data as a collaborative effort. A suite of software tools has been developed which allows all of the data to date to be successfully modelled.

Data was simulated using a standard 4-parameter (4PA) analytical model, as was described in chapter 3. In the 4PA model, the relevant parameters, K', m, V_T and R_{DS} were extracted simultaneously as described above. A standard 3-parameter model (OP1) is also introduced for the first time, and is only used for output characteristics. The main purpose of this 3 parameter model is to provide accurate confirmation of V_T and R_{DS}, particularly in cases where the number of relevant data points (<12) is insufficient to accurately extract 4 parameters. In order to extract K', a value of m must be supplied from an additional source, e.g. a prior analysis of transfer characteristics.

A standard 5-parameter (5SC) model is similar to 4PA, for cases where the contact resistances, R_D and R_S may exhibit Schottky effects; two parameters are required to accommodate such effects where only one is required for strictly passive contacts to the source and drain electrodes. These parameters allow the voltage-dependent values of R_D and R_S to be determined for any voltage conditions, providing for a straightforward passive effect ($R_D=R_S$) to a pronounced Schottky behaviour ($R_D{\neq}R_S$).

Additionally, in cases where charge carriers are tunnelling through the gate oxide thereby causing a leakage current, a 5-parameter model (5LP) to partner 4PA, and a 6-parameter model (6SP) to partner 5SC were also found to be necessary. These accommodate passive or Schottky contact effects with a distributed passive gate-to-accumulation channel leak, R_L. In practice in all the devices studied, gate leakage was not found to be significant enough to warrant the additional parameter. The relevant expressions have therefore not been detailed in this thesis.

When studying output data, a further effect becomes apparent. This occurs as a result of the "bypass" resistance offered by the bulk of the semiconductor other than that in the accumulation region. Variation of V_{DS} in output curves then introduces an additional current contribution. 4PA and 5SC are complemented by 5BY and 6SB to include this effect at the expense of an extra parameter, R_B, in each case. Similarly, OP1 is complemented by OPB and OSB to cover passive and Schottky contact effects with bypass with 1 and 2 extra parameters, respectively.

Transfer characteristics. The experimental results of 6CuPc sample are presented below along with statistically modelled data using the 4PA, 5SC and 6SP analytical expressions. The experimental transfer data is handled first. Tables 5.1a and 5.1b present the extraction of parameters from these 3

models; it is clearly evident that the parameters are almost identical from each of the three methods at their specified drain-to-source voltages, V_{DS}.

Table 5.1a. OTFT extracted parameters for as-deposited 6CuPc films of V_{DS}=-5V using 4PA, 5SC and 6SP model.

6CuPc											
V_{DS}=-5V											
	K'	V_T (V)	m	$R_O(\Omega)$	$R_X(\Omega)$	$R_L(\Omega)$	R^2	Error (%)	D	$R_D(\Omega)$	$R_S(\Omega)$
Method 4PA[+]	3.91_x10^{-9}	5.3	0.0913	$2.30x10^6$	0	∞	0.9997	1.6	2.7	1.15_x10^6	1.15_x10^6
Method 5SC[≠]	3.80_x10^{-9}	5.4	0.0907	2.09_x10^6	3.55_x10^4	∞	0.9996	1.7	2.6	1.07_x10^6	1.19_x10^6
Method 6SP	3.72_x10^{-9}	5.5	0.0916	2.03_x10^6	3.84_x10^4	2.18_x10^{10}	0.9996	1.7	2.6	1.04_x10^6	1.20_x10^6

+ R_O= R_{DS} ,R_X=0 R_L= ∞

$\neq$ R_L= ∞

Table 5.1b. OTFT extracted parameters for as-deposited 6CuPc films of V_{DS}=-45V using 4PA, 5SC and 6SP model.

6CuPc											
V_{DS}=-45V											
	K'	V_T (V)	m	$R_O(\Omega)$	$R_X(\Omega)$	$R_L(\Omega)$	$\mathscr{R}^2$	Error (%)	D	$R_D(\Omega)$	$R_S(\Omega)$
Method 4PA[+]	6.25_x10^{-9}	9.4	0.0870	1.92_x10^6	0	∞	0.9996	2.15	2.9	9.58_x10^5	9.58_x10^5
Method 5SC[≠]	5.83_x10^{-9}	9.0	0.0939	1.69_x10^6	7.42_x10^3	∞	0.9997	1.21	2.8	8.49_x10^5	9.67_x10^5
Method 6SP	5.95_x10^{-9}	9.1	0.0831	1.56_x10^6	8.06_x10^3	1.77_x10^9	0.9997	1.19	2.6	7.86_x10^5	9.39_x10^5

In the 5SC and 6SP models, $R_O(\Omega)$, $R_X(\Omega)$, and $R_L(\Omega)$ have been introduced as device parameters. R_O and R_x determine the passive and active contributions to the contact resistances, respectively. The values of $R_D(\Omega)$ and $R_S(\Omega)$ are determined separately as functions of R_O, R_X and the maximum value of V_{DS}. If R_D (Ω) and R_S (Ω) are identical then Schottky effects are absent. R_L is a parameter which defines the leakage resistance between the gate and the accumulation region.

In all cases, R_D and R_S evaluated at the maximum value of V_{GS} are essentially equal, clearly showing that Schottky contact effects are insignificant in the 6Cu-series. Simulations were then performed using 4PA results; the current-voltage curves describing the transfer characteristics for an as-deposited 6CuPc OTFT are presented in Figure 5.3.
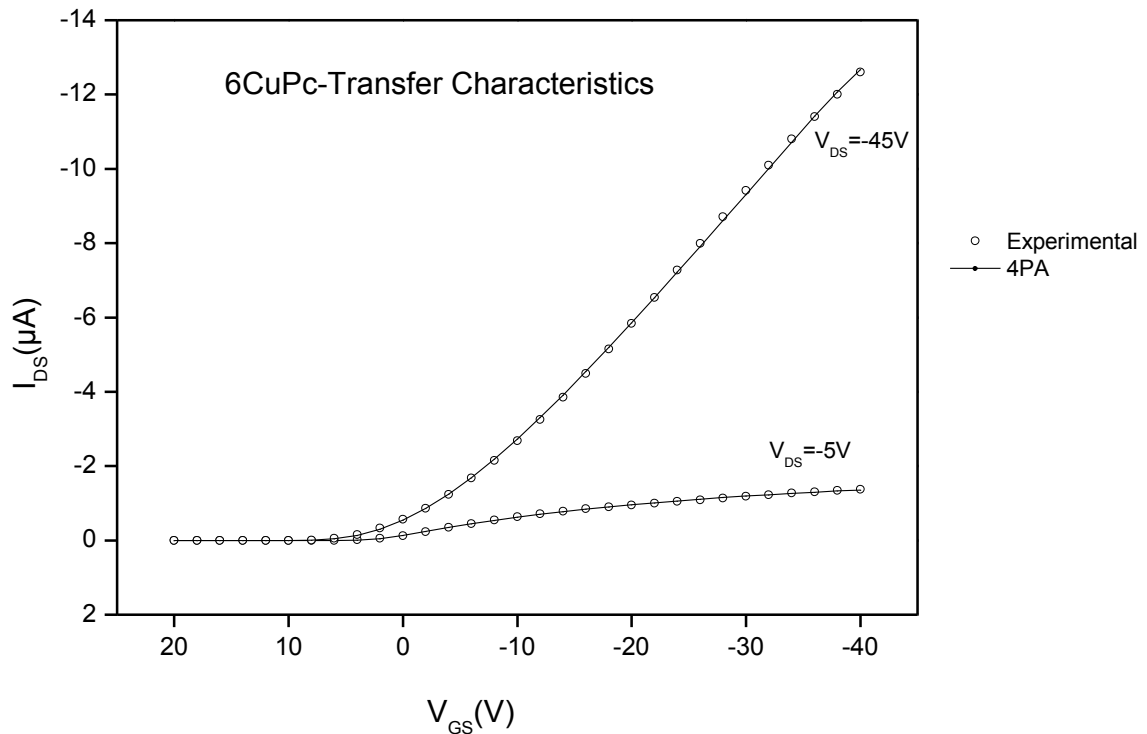
Figure 5.3. Transfer characteristics for 6CuPc films in terms of the variation of the drain current (I_{DS}) as a function of the gate voltage (V_{GS}) for V_{DS}= –5V and V_{DS}= –45V; experimental data (open circle), 4PA modelled data (solid line).

The values in Table 5.1a and 5.1b should be regarded in relation to the relative error in parameter determination by the statistical method used. All the software tools used in this study had the facility to perform the reverse process, in the sense that a set of previously extracted parameters could be used to simulate a hypothetical (and noise-free) set of data. The method could then be tasked to resolve the parameters to reveal the differences between the hypothetical and the experimental data. These differences provide a good indication of the errors inherent in the experimental procedure and parameter extraction process. Using the method 4PA, from Table 5.2, it can be seen that simulating the transfer data for the linear region, the maximum errors in the parameters K', V_T, m and R_{DS} are approximately, 6.4%, 1.9%, 11 % and 1.7% respectively, whilst for the saturated region they are 3.4%, 1.1%,12% and 2.6%.

Table 5.2. OTFT parameters for hypothetical data for as-deposited 6CuPc films (see text).

	6CUPC- OTFT			
	4PA			
	Linear region (V$_{DS}$=-5)		Saturation region (V$_{DS}$=-45)	
	Expt. data	Resim. data	Expt. data	Resim. Data
K'	$3.91_x 10^{-9}$	$4.16_x 10^{-9}$	$6.25_x 10^{-9}$	$6.46_x 10^{-9}$
V$_T$(V)	5.3	5.2	9.4	9.5
m	$9.13_x 10^{-2}$	$8.09_x 10^{-2}$	$8.70_x 10^{-2}$	$7.68_x 10^{-2}$
R$_{DS}$ (Ω)	$2.31_x 10^6$	$2.27_x 10^6$	$1.92_x 10^6$	$1.87_x 10^6$
R$_D$ (Ω)	$1.15_x 10^6$	$1.13_x 10^6$	$9.58_x 10^5$	$9.37_x 10^5$
R$_S$(Ω)	$1.15_x 10^6$	$1.13_x 10^6$	$9.58_x 10^5$	$9.37_x 10^5$
μ$_o$ (cm^2 V^{-1}s^{-1})	$3.91_x 10^{-3}$	$4.16_x 10^{-3}$	$6.25_x 10^{-3}$	$6.46_x 10^{-3}$
T$_C$ (^{o}K)	327.4	324.2	326.1	323.0
MNE(meV)	26.7	26.5	26.6	26.4
D	2.7	2.6	2.9	2.7
$\mathscr{R}^2$	0.999708	0.999999	0.999596	0.999998
Err(%)	1.6	0.13	2.2	0.15

The transfer simulations cover both the linear and saturation regions, and include voltages below and above the threshold voltage, V$_T$. The device parameters were extracted after the modelling of the experimental data was complete. These are listed in Tables 5.1a & 5.1b. The basic four parameter model provides simulated data which closely reproduces the experimental data. The relative errors of the simulations are best assessed as an root mean square (rms) value, but including the most relevant points. Our subjective choice includes all points in the range of 0.1 ... 1.0 of the maximum value of I$_{DS}$. (Below this range small absolute errors cause large relative errors, which in turn detract from the useful purpose of this quantity.) For V$_{DS}$=-5V and V$_{DS}$=-45V the values obtained are 1.6% and 2.2%, respectively. It is useful to note that a basic guideline for statistical modelling is to use the model with the smallest number of parameters for reliable interpretation purposes, and this is adopted in the above case. From the extracted parameters, the underlying fundamental quantities: μ$_o$, T$_C$ and Meyer-Neldel energy (MNE) are presented in Table 5.3. The MNE defines the width of the DOS distribution (σ) in the conductive channel of an organic semiconducting film. It is given by $k_B T_C/q$, where q is the electronic charge.

Table 5.3. OTFT extracted parameters with estimated errors for as-deposited 6CuPc films using the 4PA model.

6CuPc						
4PA						
V_{DS}	K'	m	$R_{DS}(\Omega)$	μ_o (cm^2 V^{-1}s^{-1})	T_C (^{o}K)	MNE(meV)
-5V	$3.91\pm0.26 _x10^{-9}$	$9.1\pm1.1_x10^{-2}$	$2.31\pm0.05 _x10^6$	$3.91 \pm0.26 _{x}10^{-3}$	327.4 ± 3.2	26.7 ± 0.2
-45V	$6.25\pm0.31_x10^{-9}$	$8.7\pm0.3 _x10^{-2}$	$1.92\pm0.17_x10^6$	$6.25\pm0.31_x10^{-3}$	326.1 ± 1.0	26.6 ± 0.1

In Table 5.3, the mobility, μ_o, determined principally from K', appears to increase by a factor of 1.6 going from the linear region (V_{DS}=-5V) to the saturated region (V_{DS}=-45V). However, from Table 5.2, the maximum error in determination of K' is approximately 6%, and so the errors in determining the mobilities are the same. The maximum error of determination of V_T is only 2%, so by the same comparison, V_T is increased by *ca.* 2x; also representing a significant increase. The m-values reveal the crystalline nature of the organic semiconductor's active layer. A semiconductor film with lower m-values implies a more crystalline state and therefore higher mobility values. Although, the m-value for a given material is expected to be the same, it is found that the m-value for the saturation region is ca.10% lower than that in the linear region. Notably, the maximum error in determination is estimated to be 10%, and therefore within this error the m-values are the same. Finally, the contact resistance, R_{DS}, for the saturation region is reduced by 17%, whilst the maximum error of determination is only 4.3%. This change is significant: however in the saturation region the drain voltage is increased by *ca.*10x, and likewise the resistance characteristic of the accumulation channel is reduced. This is the material in direct contact with the metal electrode, and hence a reduction in the contact resistance is expected.

T_C is related to the Gaussian distribution of traps in organic semiconductor materials (and similarly the quantity, MNE). According to the T_c value for the semiconductor film of 6CuPc, it would suggest that higher trap states exist at the V_{DS}=-5V than at the V_{DS}=-45V, but the distribution of traps should be the same in both situations unless the structure or temperature has changed between the two measurements. The slight changes in m, T_C and MNE are within the error of determining m.

Output characteristics. The experimental data of the I_{DS}-V_{DS} output characteristics were also measured by sweeping V_{DS} from 0 to -50V in 2V steps for each value of V_{GS}. V_{GS} is set in the range 0 to -50V at 10V intervals. The 6CuPc OTFT device performs in a similar way to the inorganic TFT device with the exception that at higher values of V_{DS} (for V_{GS}= -40V & -50V) a better development of the plateau region occurs. It is clearly observed that in both such curves, the output I_{DS} is not completely saturated as V_{DS} is swept from 0 to -50V. However, the value of K' is determined by the two main features of the curve, namely the initial gradient and the height of the plateau region, and is thus poorly defined for these values of V_{GS}. Conversely, the output curve for V_{GS} = 0V does not exhibit a linear region at low values of V_{DS}. As a result the K' determined from V_{GS}= 0V, -40V & -50V are less

accurate. In general, the determination of parameters from the V_{GS}= -10V and -20V plots provide most accurate results.

The experimental data of output characteristics were simulated using the 5BY analytical model. This 5-parameter analytical model was developed particularly for output characteristics only. (In transfer, the effect of R_{BY} is simply to add a small constant to all values and is thus undetermined.) In output, the additional extracted parameter is R_{BY}, which is generally some orders of magnitude larger than R_{DS}. The 5BY model obtains more accurate values of K', V_T and m. The modelling results from 5BY and experimental data for the output curves are presented in Figure 5.4. The modelling produces fits to the experimental data and the fitting errors are increased from 0.9% to 5.1% as V_{GS} is increased from V_{GS}=0V to V_{GS}=-50V, respectively.
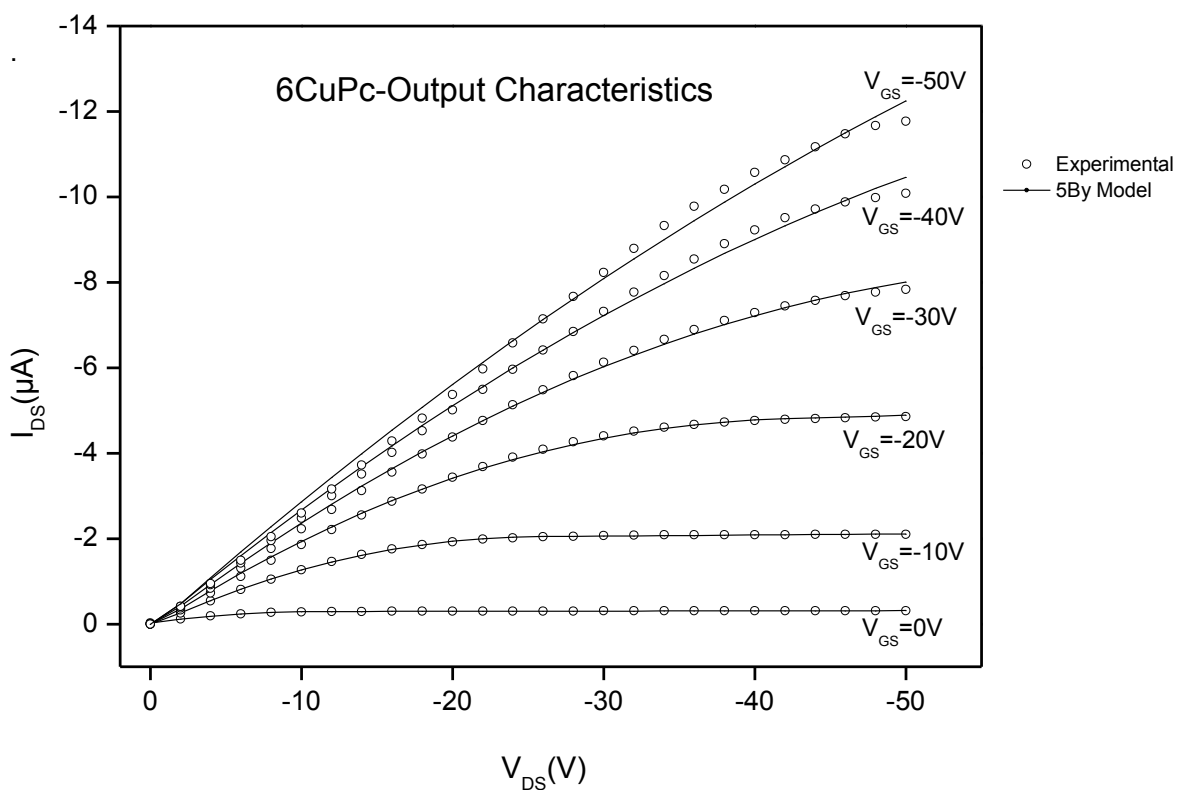
Figure 5.4. Output characteristics for an OTFT with the 6CuPc films in terms of the variation of the drain current as a function of the drain voltage for experimental (open circle), 5BY-modelling (solid line).

In Table 5.4 the extracted parameters from the 5BY model are presented. It is evident that the extracted parameters vary unreliably. Remembering the earlier comments regarding extraction accuracy, one notes that the values for V_{GS}= -10, -20 and -30V form a more consistent trend, and the V_{GS} =0, -40 and -50V can be dismissed. For the three middle values of V_{GS}, the m-values do not change in a progressive manner with V_{GS}. However, the extracted m-values from V_{GS} = -10V, -20V and -30V were 0.084, 0.087 and 0.083, respectively, which lie within experimental error of each other and are also consistent with the values obtained from the transfer data. The K' values decrease

monotonically as the V_{GS} is increased, but curiously are reduced compared with the values obtained from the transfer data. Similarly, V_T is shown to increase in a similar manner; at this stage one notes that V_T is not constant, and the results from both transfer and output data indicate that V_T is somehow dependent on V_{GS} and V_{DS}; the dependence has yet to be resolved. Both R_{DS} and R_{BY} are decreased. The R_{DS} values are expected to decrease as the accumulation layer changes, in the same way as discussed for the transfer data. The R_{BY} values are higher by two orders of magnitude, but also show a decrease going to higher V_{GS}. The notional separation of the "bulk" from the "accumulation" is probably a coarse approximation, so that the "bulk" is "pulled" down slightly for the same reason as for R_{DS}.

Table 5.4. Extracted parameters based on 5BY model from the output characteristics of transistors for as-deposited 6CuPc films.

6CUPC											
5By											
V_{GS}	K'	V_T (V)	m	$R_{DS}(\Omega)$	$R_{BY}(\Omega)$	D	$\mathscr{R}^2$	Err (%)	μ_o (cm^{2}V^{-1}s^{-1})	T_C (°K)	MNE (meV)
0V	1.52_x0^{-9}	11.6	0.0805	2.18_x10^6	1.90_x10^9	1.06	0.9986	0.9	1.52_x10^{-3}	324.2	26.5
-10V	1.92_x10^{-9}	15.3	0.0842	7.09_x10^5	3.79_x10^8	1.06	0.9996	0.9	1.92_x10^{-3}	325.2	26.6
-20V	1.42_x10^{-9}	21.4	0.0872	5.01_x10^5	1.03_x10^8	1.06	0.9992	2.7	1.42_x10^{-3}	326.2	26.6
-30V	1.07_x10^{-9}	31.9	0.0833	4.19_x10^5	8.50_x10^7	1.07	0.9987	3.9	1.07_x10^{-3}	325.0	26.5
-40V	8.89_x10^{-10}	47.0	0.0710	3.82_x10^5	7.57_x10^7	1.08	0.9974	4.3	8.89_x10^{-4}	321.3	26.2
-50V	8.00_x10^{-10}	66.2	0.0549	3.55_x10^5	6.55_x10^7	1.09	0.9966	5.1	8.00_x10^{-4}	316.5	25.8

With regard to the derived mobilities and T_C values derived from the extracted data the situation is complicated. The m-values are consistent over the transfer and output data, and will provide reliable values of T_c. But since the K' are significantly reduced compared with the values obtained from the transfer data, the mobility values derived from them are questionable, and this area will be left to later discussion. Here, the apparent dependence on V_{DS} and V_{GS}, will be minimised for the V_{DS} =-5V transfer data. This is because the device parameters extracted from V_{DS} =-5V are the least influenced by a lateral field, which in turn attenuates any effect of the transverse field. They are arguably best able to characterise the organic semiconductor's active layer of the OTFT device at this time.

5.1.2 6Cu-TBTAP–OTFTs

6Cu-TBTAP sample has a similar molecular structure to its counterpart 6CuPc, but the 6Cu-TBTAP is formed by replacing a nitrogen atom by a single carbon atom and bound hydrogen. The molecular structure of 6Cu-TBTAP can be found in Figure 5.2 (b). (The OTFT device had dimensions of L=5μm and W=1mm, and C_i =10nFcm^{-2})[5]. Data of the transfer characteristics of 6Cu-TBTAP OTFT devices were used to simulate the performance and extract the key parameters using the 5SC model.

In contrast to the transfer curves for 6CuPc, those for 6CuTBTAP do not fit satisfactorily assuming Ohmic contact resistances. Figure 5.5 shows the comparison of the Ohmic (4PA) and Schottky (5SC) contacts in the case of the V_{DS}=-40V transfer curve. The best Ohmic fit is clearly in unsatisfactory with $\mathscr{R}^2$ = 0.995,but this improves dramatically to $\mathscr{R}^2$ = 0.9995 when Schottky contact effects are included. From a comparison of the parameters extracted shown in Table 5.5, this can lead to significant changes in the denominator, D, accounting for contact effects, and the value of K' from which the mobility μ_o is obtained.

Figure 5.5. Transfer characteristics for 6Cu-TBTAP films in terms of the variation of the drain current (I_{DS}) as a function of the gate voltage (V_{GS}) comparison of the Ohmic (4PA) and Schottky (5SC) contacts in the case of the V_{DS}=-40V transfer curve, experimental data (close circle), 4PA modelled data (broken line). 5SC modelled data (solid line).

Table 5.5. OTFT parameters for as-deposited 6Cu-TBTAP at V_{DS}=-40V films comparison of the Ohmic (4PA) and Schottky (5SC) contacts with a selection of fixed m-values.

6TCuPc											
5SC											
V_{DS}=-40V	K'	V_T (V)	m	$R_O(\Omega)$	$R_X(\Omega)$	R_B	$\mathscr{R}^2$	Err (%)	D	$R_D(\Omega)$	$R_S(\Omega)$
4PA (Ohmic)	2.63×10^{-8}	6.45	6.06×10^{-2}	2.42×10^6	0.00	1.00×10^{18}	0.9947	7.19	8.75	1.21×10^6	1.21×10^6
5SC (Schottky)	8.28×10^{-9}	6.60	9.71×10^{-2}	3.13×10^5	1.31×10^4	1.00×10^{18}	0.9995	2.04	3.64	1.70×10^5	1.14×10^6

The experimental and simulated data for V_{DS} =-5v and V_{DS} =-40v using to 5SC model are presented in Figure 5.6. The reproduced simulated data fit the experimental data with estimated errors of 3.2% and 2.0%, for linear and saturation regions, respectively. When fitting these data, the denominator, D, accounting for contact resistances in the expressions (see Chapter 3, equations 3.3.20 and 3.3.21) exceeds a borderline value (*ca.* 3) for accuracy in determining m and K'. Moreover, for this material in particular, the accuracy in determining the m-values is additionally impaired owing to a particularly flat response to variations in m on the multidimensional surface of $\mathscr{R}^2$. To handle this situation, it is assumed that the value of m is a constant of the coated material; the average of the freely optimised values of m for V_{DS} = -5V and -40V is then held fixed for extraction of the other parameters. Note that the V_T-values are not affected significantly since the transfer curves contain a definite onset characteristic. for both the transfer curve D exceeds 3.equaly good fitting is obtained for fixed values in the rage 0.022-0.098.therfore fitting is carried out at fixed values of m equals 0.065 0.033,ther by obtaining limiting values of the other parameters (K',V_T, etc.),and hence the corresponding errors in their determination. μ_o, T_C and MNE values of the 6Cu-TBTAP films can be obtained, by using a spread of fixed values for m (0.065±0.033) for both the values of V_{DS}. The results are then as listed in Tables 5.6 and 5.7.

6CuTBTAP-Transfer Characteristics

I_DS(μA) vs V_GS(V)

V_{DS}=-40V
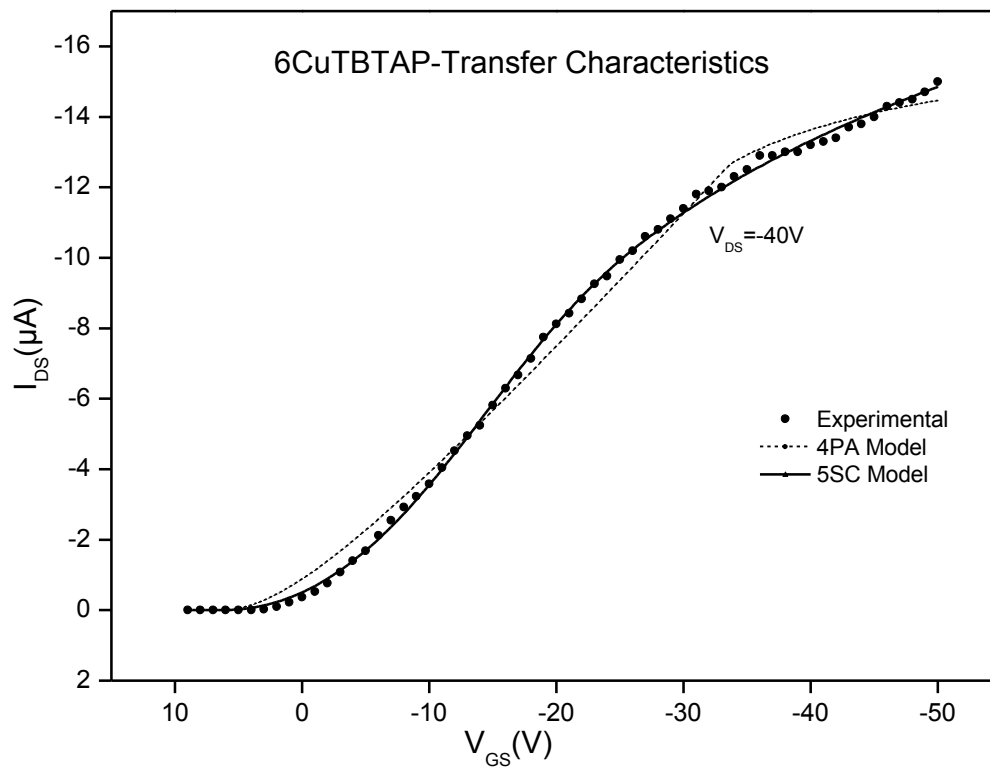
V_{DS}=-5V
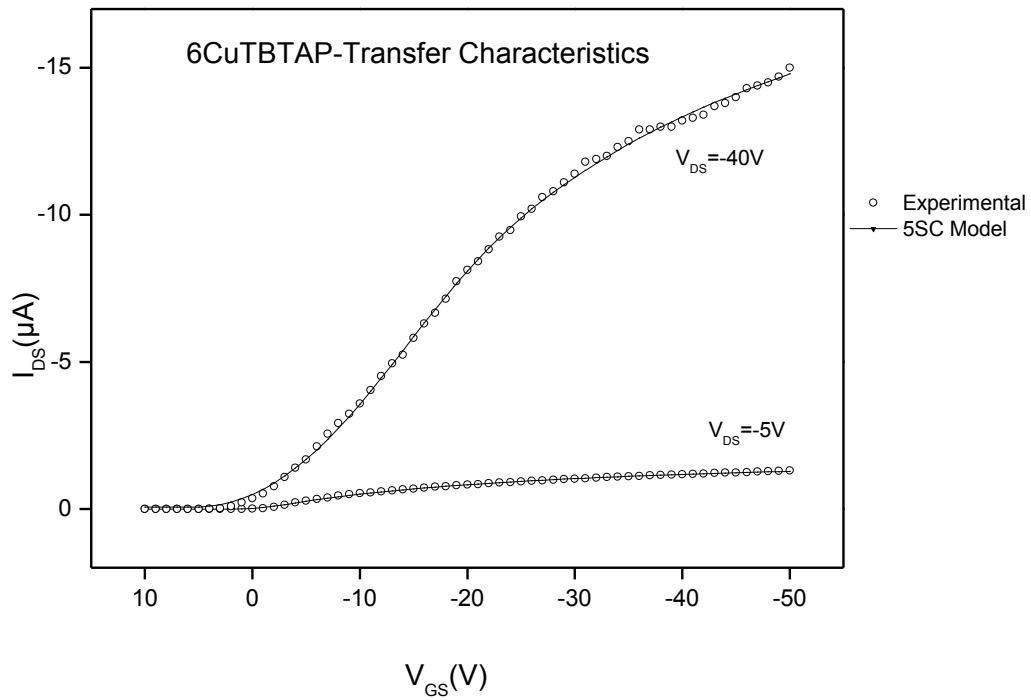
○ Experimental
— 5SC Model

Figure 5.6. Transfer characteristics for 6Cu-TBTAP films in terms of the variation of the drain current (I_{DS}) as a function of the gate voltage (V_{GS}) for V_{DS} = -5V and V_{DS} =-40V, (experimental - open circle) and (modelling - solid line).

Table 5.6. OTFT parameters for as-deposited 6Cu-TBTAP at V_{DS}=-5V films using 5SC with a selection of fixed m-values.

6TCuPc										
5SC										
V_{DS}	K'	V_T (V)	m	$R_O(\Omega)$	$R_X(\Omega)$	$\mathscr{H}^2$	Err (%)	D	$R_D(\Omega)$	$R_S(\Omega)$
-5V	$4.89\pm1.04_x10^{-9}$	2.3 ± 0.3	0.065 ± 0.033	$2.66\pm0.11_x10^6$	$2.73\pm0.24_x10^4$	0.9988 ± 0.0003	3.2 ± 0.4	3.4 ± 0.3	$1.35\pm0.05_x10^6$	$1.40\pm0.05_x10^6$
-40V	$1.06\pm0.28_x10^{-8}$	6.2 ± 0.5	0.065 ± 0.033	$3.14\pm0.70_x10^5$	$1.32\pm0.01_x10^4$	0.9995 ± 0.0001	2.0 ± 0.1	3.1 ± 0.1	$1.70\pm0.04_x10^5$	$1.08\pm0.01_x10^6$

According to the extracted device parameters for 6Cu-TBTAP films (see Table 5.7), K' for the linear region (V_{DS}=-5V) is lowered by a factor of *ca.* 2.2 compared with the saturation region (V_{DS}=-40V). Over the range of m-values centred about the extracted value for V_{DS}=-5V (m=0.065), the spread in K-values is relatively small, ±21% and ±26%, respectively. These indicate that the increase in μ_o from 4.89×10^{-3} to 1.06×10^{-2} cm^2 V^{-1}s^{-1} lies outside of these errors in going from the linear to the saturation region. The V_T are shifted to more positive values by a factor of 2.5 going from the linear region (V_{DS}=-5V) to the saturation region (V_{DS}=-40V).

Table 5.7. OTFT extracted parameters for as-deposited 6TCuPc films using the 5SC model.

6TCuPc					
5SC					
V_{DS}	K'	m	μ_o (cm^2 V^{-1}s^{-1})	T_C (^{o}K)	MNE(meV)
-5V	$4.89\pm1.04\ _x10^{-9}$	0.065 ± 0.033	$4.89\pm0.54\ _x10^{-3}$	319.5 ± 9.9	26.1 ± 0.8
-40V	$1.06\pm0.28\ _x10^{-8}$	0.065 ± 0.033	$1.06\pm0.28\ _x10^{-2}$	319.5 ± 9.9	26.1 ± 0.8

Although the semiconductor film for the saturation region shows higher mobility, a fixed m-value will deliver the same T_C and MNE values compared with the linear region. The Ro-values, which represent the ohmic contribution to the contact resistance has decreased in going from the linear region (V_{DS}=-5V) to the saturation region (V_{DS}=-40V) by an order of magnitude. This comes about for the same reason as given for the 6CuPC performance. For the saturation region the drain voltage is increased by ca.10x, and likewise the resistance characteristic of the accumulation channel is reduced. Again, this is the material in direct contact with the metal electrode, and hence a reduction in the ohmic part of the contact resistance is expected. Here, however, the mobilities are also higher, which explains the more pronounced effect. The output characteristics also display departures from the best fit using the 5SC model unlike the transfer conditions of V_{DS} = constant. For output, V_{DS} is swept and the problem of not taking in to account the bulk semiconductor resistance lying beyond the accumulation channel becomes evident. A comparison of 5SC (without R_B) and (taking account of R_B) is shown in Figure 5.7 for V_{GS}=-10V again, $\mathscr{R}^2$ improves dramatically from $\mathscr{R}^2$=0.985 (5SC) to $\mathscr{R}^2$=0.998 (6SB).

The output characteristics of as-deposited 6TCuPc films are for V_{GS}= -10V and -20V are shown in Figure 5.7. The best fit was obtained using the 6SB model where current through the bulk resistance contributes to that from the accumulation layer. As presented in 5.8, the fitting errors were estimated to be 1.9% and 1.1%, for V_{GS}= -10V and -20V ,respectively.

Figure 5.7. Output characteristics for an OTFT with the 6TCuPc films in terms of the variation of the drain current as a function of the drain voltage for experimental (open circle), 6SB -modelling (solid line).
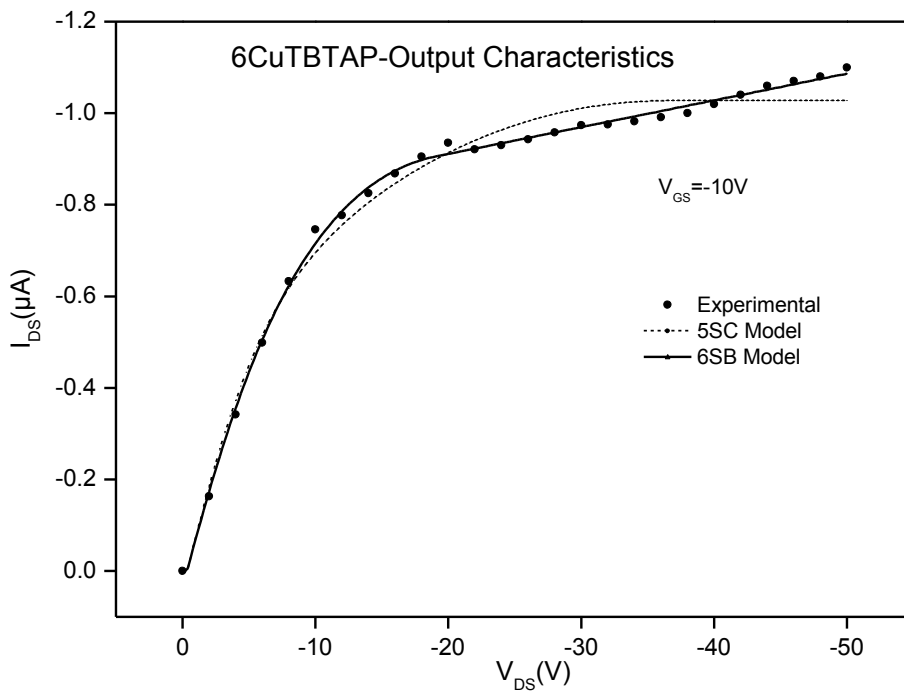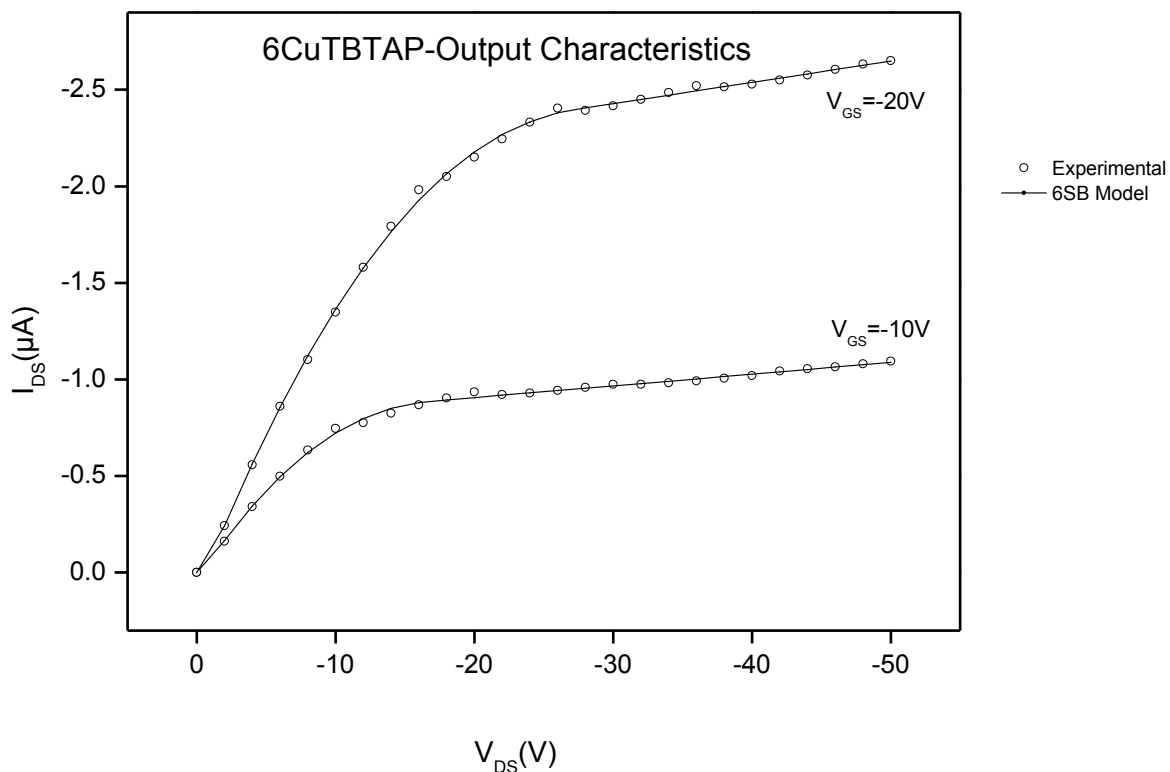

Figure 5.8. Output characteristics for an OTFT with the 6TCuPc films in terms of the variation of the drain current as a function of the drain voltage for experimental (open circle), 6SB -modelling (solid line).

The 6SB model was used to determine the extracted parameters, the denominators are found to be below 3 for both V_{GS}= -10V and -20V, and the m–values determined from V_{GS}=-10v are similar to the m–values determined for V_{GS}=-20V. However, very good fits are obtained for a very wide range of fixed m-values (0 … 0.1) for the experimental data for this particular sample. The reason has been given above. For completeness, the extracted values are shown in Table 5.8. However, only the K' values from the transfer curves are used for estimating μ_0.

Table 5.7. extracted parameters based on 6SB model from the output characteristics of transistors for as-deposited 6TCuPc films.

6TCuPc											
6SB											
V_{GS}	K	V_T (V)	m	$R_O(\Omega)$	$R_X(\Omega)$	$R_B(\Omega)$	$\mathscr{R}^2$	Err (%)	D	$R_D(\Omega)$	$R_S(\Omega)$
-10V	1.75_x10^{-9}	8.6	0.09292	1.14_x10^6	1.19_x10^5	1.73_x10^8	0.9985	1.9	1.30	6.78_x10^5	2.45_x10^6
-20V	1.80_x10^{-9}	7.4	0.08649	6.44_x10^5	3.70_x10^4	9.44_x10^7	0.9994	1.1	1.13	3.52_x10^5	6.71_x10^5

5.2   10CuPc- and 10CuTBTAP-OTFTs

10CuPc and 10CuTBTAP molecules differ from 6CuPc & 6CuTBTAP, respectively, by having a longer alkyl chain length (R = -$C_{10}H_{21}$) at the same non-peripheral position of substitution. The 10Cu- and 10TCu-series present a more difficult analysis problem. As the extractions of the transfer data proceed in both the linear (V_{DS}=-5V) and saturated (V_{DS}=-45V) regions, using the above methods, denominators, D >> 3 are encountered. As noted in the 6Cu- and 6TCu-series, the m- and K'-values will then be very poorly determined. To overcome this problem, use of the respective output data is made. Generally, the fitting is good for a range of fixed V_{GS}, and the denominators are in the range 1.0 to 1.3. Also, provided the quantity (V_{GS}-V_T) is placed approximately in the middle of the swept V_{DS} range, the most reliable value of m is delivered. For the transfer analyses, the reasonable way to proceed is to adopt this m-value as fixed, since this is representative of the material as a constant, but with a generous margin of error (*ca.* 25%).

The channel length L= 5μm and channel width W= 2 mm were the dimensions for both the 10CuPc- and 10CuTBTAP-OTFT devices, and the device capacitance was C_i = 14 nFcm^{-2}[3].

5.2.1 10CuPc–OTFT's

The output characteristics for V_{GS}=-10V and -20V are presented in Figure 5.7, since these both place V_{GS}-V_T centrally in the swept V_{DS} range. The extracted parameters for these data are given in Table 5.8, here it can be seen that the m-values are fairly consistent, and the denominators are <2. The analysis of the transfer data then adopts a range of m=0.086±0.020. In the same way as for the 6TCu

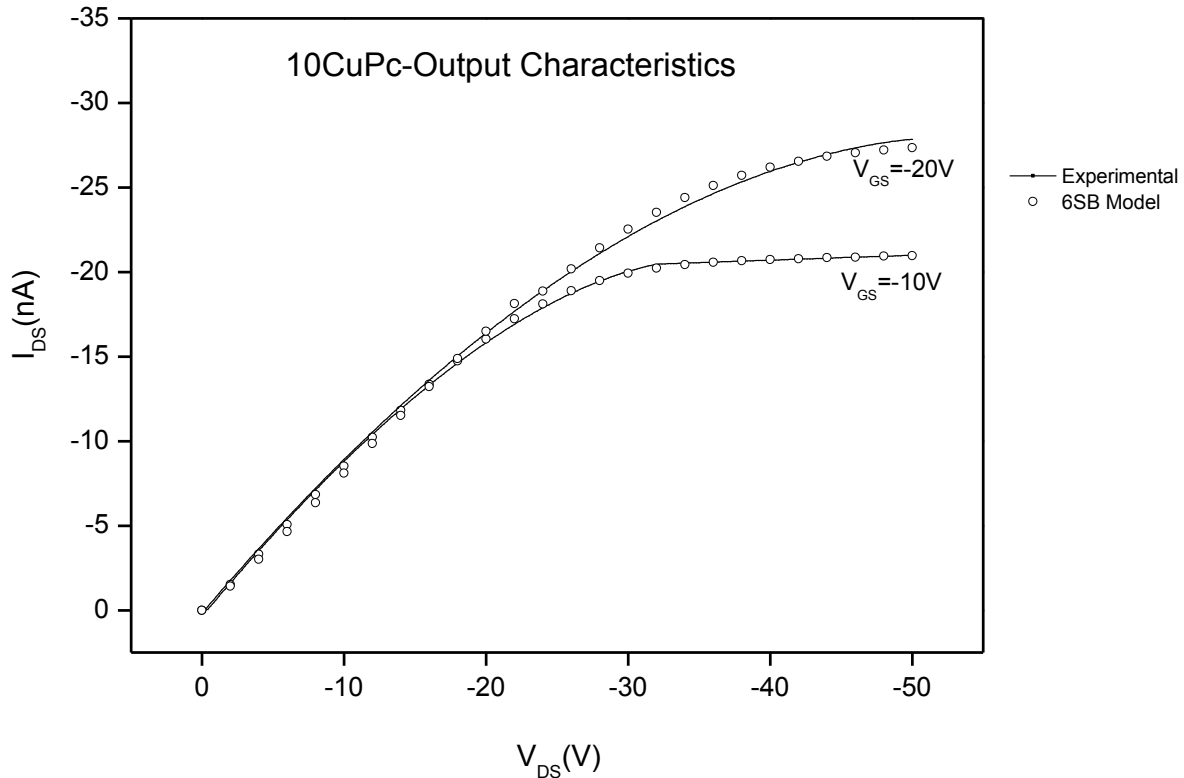data, the extracted values are obtained as the median value± error derived from the range of fixed m used.

Figure 5.7. Output characteristics for an OTFT with a 10CuPc film showing the drain current as a function of the drain voltage for the experiment (open circle) and the 6SB-modelling (solid line).

Table 5.8. Extracted parameters using the 6SB model from the output characteristics of transistors for as-deposited 10CuPc films.

10CuPc											
6SB											
V_{GS}	K'	V_T (V)	m	$R_O(\Omega)$	$R_X(\Omega)$	$R_B(\Omega)$	$\mathscr{R}^2$	Err (%)	D	$R_D(\Omega)$	$R_S(\Omega)$
-10V	1.90_x10^{-11}	21.8	0.071	5.53_x10^8	2.23_x10^6	3.46_x10^{10}	0.9994	2.3	1.6	2.78_x10^8	2.84_x10^8
-20V	7.64_x10^{-12}	29.4	0.069	3.37_x10^8	1.90_x10^6	2.28_x10^{10}	0.9972	6.6	1.3	1.70_x10^8	1.76_x10^8

The K'-value is reduced by a factor of *ca.*2.5 as the V_{GS} increases from V_{GS}= -10V to V_{GS}= -20V, whilst V_T increases by a factor of *ca.*1.4. The discussion of this and the interpretation of K' and V_T will be handled later. For the following analysis of the transfer data, the m-value from the V_{GS}=-10V output analysis is preferred since (V_{GS}-V_T) is placed most centrally in the V_{DS} range. The same margin of error in m, i.e. ±0.020, is applied when extracting from both the V_{DS}=-5V and -45V data.

The experimental I-V transfer characteristics of the 10CuPc-OTFT were fitted with the 5SC model as shown in Figure 5.8. The fitting errors for the linear region (V_{DS}=-5V) and the saturation region (V_{DS}=-45V) were found to be 3.2% and 3.1%, respectively. The larger fitting errors in the saturation region (V_{DS} =-45V) compared with linear region (V_{DS} =-5V) arise from noisy experimental data for V_{DS} =-45V between V_{GS}=-11V and V_{GS}=-13V.
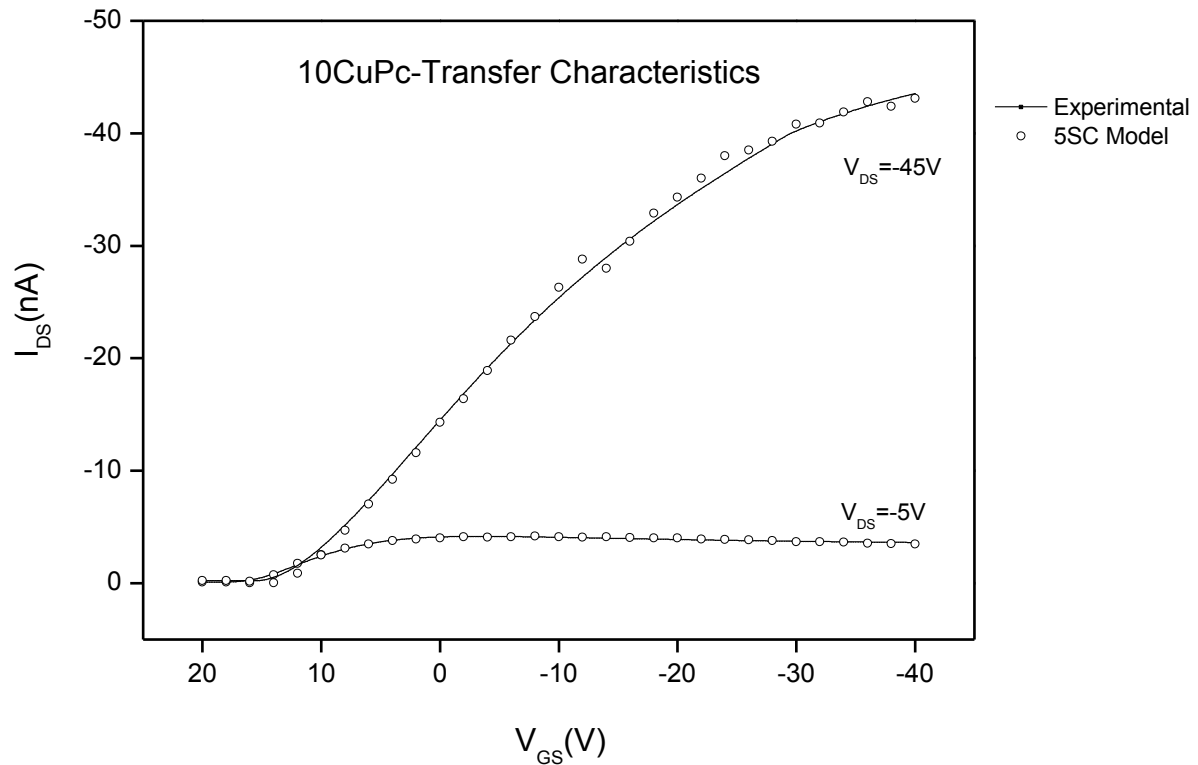

Figure 5.8. Transfer characteristics for 10CuPc-OTFT devices showing the drain current (I_{DS}) for the linear region (V_{DS}=-5V) and the saturation region (V_{DS}=-45V) as a function of V_{GS} open circle (experimental) and solid line (modelled).

The extracted 10CuPc-OTFT device parameters for the transfer curves are presented in Table 5.9, using the 5SC method. The 10CuPc-OTFT device shows the same trend as the 6CuPc-OTFT and 6CuTBTAP-OTFT devices. The K' value in the saturation region is increased by 3x compared with the linear region, as a result the μ_o in the saturation region (V_{DS}=-45v) is increased by the same factor compared with the linear region (V_{DS}=-5v). The m-values for the 10CuPc film are similar to those for 6CuPc within the error of m-determination. V_T for the saturation region (V_{DS}=-45v) has shifted to a more positive V_{GS} by *ca.* 7V. The passive contribution to contact resistance, R_O, for saturation region is increased by *ca.* 3x compared with the linear region. However, the active contribution, R_X, is reduced by ca. 5x going from the linear region to the saturation region.

Table 5.9. The extracted model parameters of 10CuPc-OTFTS for transfer characteristics using 5SC.

	10CuPc								
	5SC								
V_{DS}	K	V_T (V)	m	$R_O(\Omega)$	$R_X(\Omega)$	$\mathscr{R}^2$	Err (%)	$R_D(\Omega)$	$R_S(\Omega)$
-5V	$3.52\pm 0.4_x10^{-11}$	18.2 ± 0.1	0.071 ± 0.020	$2.28\pm 0.10_x10^8$	$2.03\pm 0.01_x10^7$	0.9952 ± 0.0005	3.2 ± 0.2	$1.34\pm 0.05_x10^8$	$1.10\pm 0.02_x10^9$
-45V	$1.10\pm 0.4_x10^{-10}$	25.7 ± 0.3	0.071 ± 0.020	$6.19\pm 0.12_x10^8$	$3.98\pm 0.01_x10^6$	0.9983 ± 0.0001	3.1 ± 0.1	$3.14\pm 0.07_x10^8$	$4.99\pm 0.04_x10^8$

Table 5.10. OTFT extracted parameters for as-deposited 10CuPc films using 5SC model.

	10CuPc				
	5SC				
V_{DS}	K'	m	μ_o (cm^2 V^{-1}s^{-1})	T_C (^{o}K)	MNE(meV)
-5V	$3.52\pm0.40_x10^{-11}$	0.071 ± 0.02	$1.40 \pm0.07_x10^{-5}$	315 ± 3	25.8 ± 0.3
-45V	$1.10\pm0.39_x10^{-10}$	0.071 ± 0.02	$3.94\pm 0.69_x10^{-5}$	321 ± 6	26.2 ± 0.5

Table 5.10 presents the outcome of the foregoing analysis. At the higher value of V_{DS} (saturation region), the mobility is increased by ca.3x compared with the lower value of V_{DS}. Both T_C and MNE values are also higher for the saturation region.

5.2.2 10Cu-TBTAP–OTFT's

A 10Cu-TBTAP organic semiconductor has similar substituent chain length to 10CuPc, but differs from 10CuPc in that a single nitrogen atom is replaced by a CH unit. As indicated in the foregoing section, the analyses of the 10- and 10T- Cu-series present a greater difficultly. A similar procedure for the 10Cu- series was used to extract the parameters from the 10Cu-TBTAP devices.

The output characteristics of the 10Cu-TBTAP device were analysed for V_{GS}= -10V and -20V. Both the experimental data and the simulated data using the 6SB model are presented in Figure 5.9. The fitting errors were found to be 3.1% and 5.7% for V_{GS}= -10V and -20V, respectively. The extracted parameters are presented in Table 5.11.
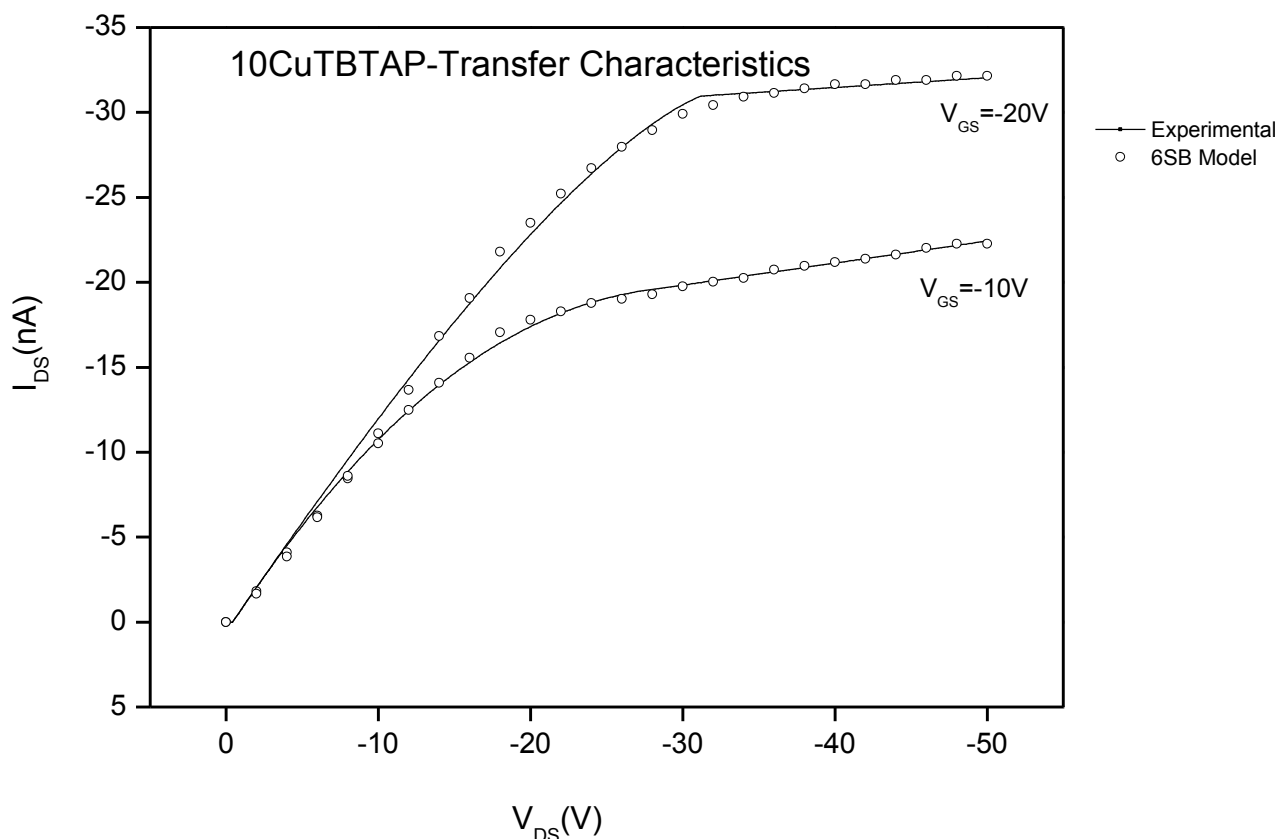
Figure 5.9. Output characteristics for an OTFT with a 10Cu-TBTAP film in terms of the variation of the drain current as a function of the drain voltage for experimental data (open circle), and the 6SB-modelled data (solid line), respectively.

The denominator for V_{GS}= -20V has a borderline value (3.2), whereas for V_{GS}= -10V this is much reduced (1.1). Note, too, that the fit for V_{GS}= -20V is visually poorer; this will be revisited at the end of this chapter. The m-value of V_{GS}= -20V is smaller by a factor of 1.20 compared with the m-value for V_{GS}= -10V. Interpretation of the K'-value and the V_T for output analysis will also be considered later.

Table 5.11. Extracted parameters for the output characteristics of the 10Cu-TBTAP device using the 6SB model.

10Cu-TBTAP											
6SB											
V_{GS}	K'	V_T (V)	m	$R_O(\Omega)$	$R_X(\Omega)$	$R_B(\Omega)$	$\mathscr{R}^2$	Err (%)	D	$R_D(\Omega)$	$R_S(\Omega)$
-10V	1.45×10^{-11}	16.8	0.08132	1.06×10^8	2.78×10^6	7.71×10^9	0.9986	3.1	1.1	5.51×10^7	6.31×10^7
-20V	4.95×10^{-11}	10.9	0.09756	6.46×10^8	1.51×10^6	1.75×10^{10}	0.9977	5.7	3.2	3.24×10^8	3.28×10^8

The transfer characteristics of 10Cu-TBTAP-OTFTs were simulated using 5SC. (In transfer, one remembers that V_{DS} is constant, thus bypass resistance from the bulk is small and constant. For transfer analysis, 5SC and 6SB are then equivalent). The m-value was used from the V_{GS}=-10V of the output characteristics, but allowing for a generous margin of error; a range of 0.081±0.020 was chosen. This will lead to a useful narrow range of K', and other device parameters from the linear region (V_{DS}=-5V) and the saturation region (V_{DS}=-45V) of a transfer analysis.
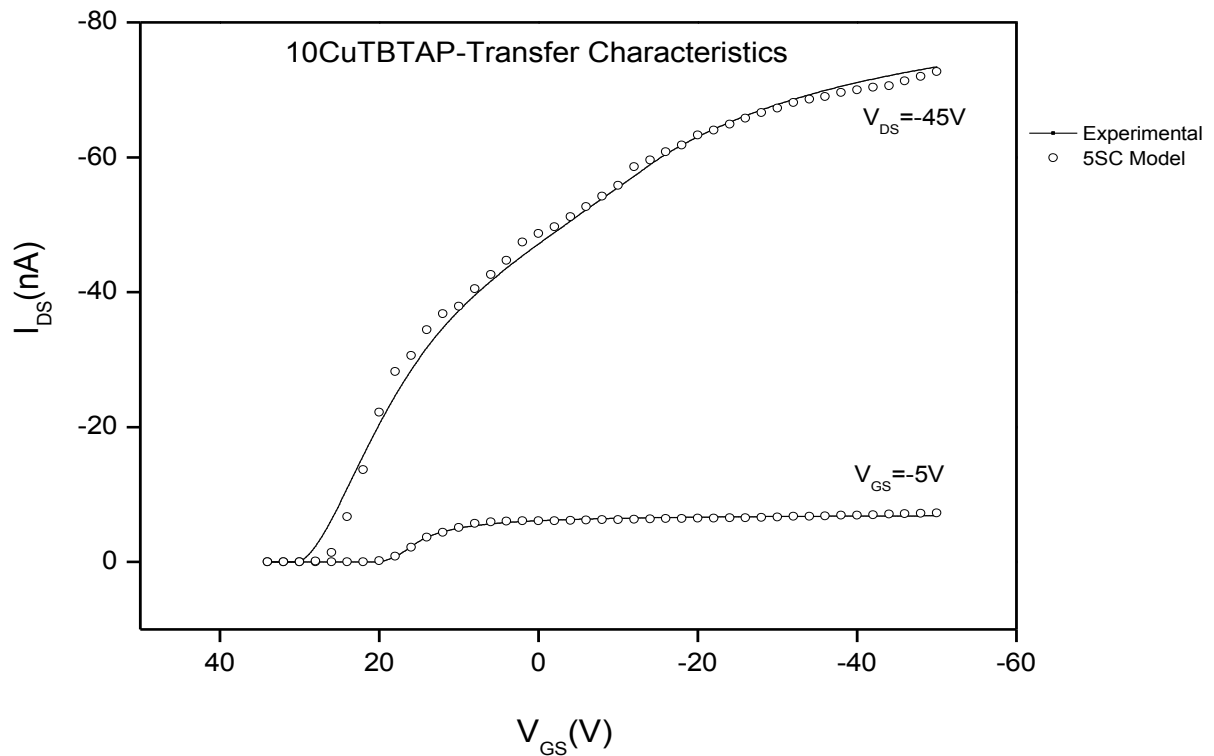

Figure 5.10. Transfer characteristics for the 10Cu-TBTAP device in terms of the variation of the drain current (I_{DS}) for linear region (V_{DS}=-5V) and saturation region (V_{DS}=-45V) as a function of V_{GS}, open circles (experimental data) and solid line (model).

Both the experimental and simulated data are presented in Figure 10. The fitting errors obtained for the linear region (V_{DS}=-5V) and the saturation region (V_{DS}=-45V) were 2.1 % and 4.3%, respectively. The extracted parameters are listed in Table 5.12 and 5.13.

Table 5.12. The extracted parameters of 10Cu-TBTAP film for transfer characteristics using 5SC model.

10Cu-TBTAP									
				5SC					
V_{DS}	K	V_T (V)	m	$R_O(\Omega)$	$R_X(\Omega)$	$\mathscr{R}^2$	Err (%)	$R_D(\Omega)$	$R_S(\Omega)$
-5V	$1.21\pm 0.14_x10^{-10}$	20.7 ± 0.1	0.081 ± 0.02	$5.79\pm 0.29_x10^8$	$1.08\pm 0.01_x10^7$	0.9959 ± 0.0001	2.1 ± 0.1	$2.98\pm 0.01_x10^8$	$4.00\pm 0.04_x10^8$
-45V	$4.72\pm 0.79_x10^{-10}$	30.5 ± 0.2	0.081 ± 0.02	$3.14\pm 0.03_x10^8$	$2.92\pm 0.02_x10^6$	0.9954 ± 0.0001	4.3 ± 0.1	$1.60\pm 0.015_x10^8$	$3.53\pm 0.03_x10^8$

Ro and Rx are reduced by factors of 1.84 and 3.70, respectively, when going from the linear to the saturation region. This suggests that the changes are brought about by the increased density of charge carriers in the accumulation layer as it interfaces with the surface adsorbed layer at the metal surface.

Table 5.13. OTFT extracted parameters for 10Cu-TBTAP films using 5SC model.

10Cu-TBTAP					
5SC					
V_{DS}	K'	m	μ_o (cm^2 V^{-1}s^{-1})	T_C (^{o}K)	MNE(meV)
-5V	$1.21 \pm 0.16_x 10^{-10}$	0.0813 ± 0.02	$4.31 \pm 0.49_x 10^{-5}$	324.4 ± 006	26.5 ± 0.5
-45V	$4.72 \pm 0.79_x 10^{-10}$	0.0813 ± 0.02	$1.69 \pm 0.29_x 10^{-4}$	324.4 ± 006	26.5 ± 0.5

K' increases by a factor of 3.90 and μ_0 is increased by the same factor in going from the linear to the saturation region. V_T becomes more positive by 10V in going from the saturation region to the linear region.

Successive analytical models were tested and applied in the study of the electrical properties of 6CuPc-, 6CuTBTAP-, 10CuPc- and 10CuTBTAP-OTFT devices. A summary of extracted device parameters for the non-peripheral Cu-series is presented in table 5.14, where the methods used were 4PA (passive contact effects) for 6CuPc, and 5SC (Schottky contact effects). (Note that the backward compatibility of 5SC delivers the same parameters as from 4PA by insisting that R_X=0). Table 5.14 presents the results taken from the linear region (V_{DS} =-5V). The different models used to examine the behaviours of the Cu -series took account of not only Schottky contact effects, but also the bulk resistance of organic semiconductor beyond the accumulation region, and possible distributed passive gate-to-accumulation channel leakage. Devices exhibiting pronounced Schottky effects invariably incur large denominators with the result that K'- and m-values tend to be poorly determined.

Table 5.14. Comparion of results for non-peripheral 6CuPc-, 6Cu-TBTAP-, 10CuPc- and 10Cu-TBTAP- OTFT, taken from the linear region (VDS =-5V) of the transfer curve.

	6CuPc	6Cu-TBTAP	10CuPc	10Cu-TBTAP
K'	$3.91\pm0.26_x10^{-9}$	$4.89\pm1.04_x10^{-9}$	$3.52\pm0.40_x10^{-11}$	$1.20\pm1.23_x10^{-10}$
V_T(V)	5.3 ± 0.1	2.3 ± 0.5	18.2 ± 0.1	20.7 ± 0.1
m	0.091 ± 0.011	0.065 ± 0.033	0.071 ± 0.020	0.081 ± 0.020
$R_O(\Omega)$	$2.30\pm0.05_x10^6$	$3.14\pm0.70_x10^5$	$2.28\pm0.10_x10^8$	$5.74\pm0.02_x10^8$
$R_X(\Omega)$	0	$1.32\pm0.01_x10^4$	$2.03\pm0.01_x10^7$	$1.09\pm0.02_x10^7$
$R_D(\Omega)$ (max.Vg)	$1.15\pm0.02_x10^6$	$1.70\pm0.04_x10^5$	$1.34\pm0.05_x10^8$	$2.96\pm0.01_x10^8$
$R_S(\Omega)$ (max.Vg)	$1.15\pm0.02_x10^6$	$1.08\pm0.01_x10^6$	$1.10\pm0.02_x10^9$	$4.02\pm0.04_x10^8$
μ_0 (cm^2 V^{-1}s^{-1})	$3.91\pm0.26_x10^{-3}$	$4.89\pm0.54_x10^{-3}$	$1.40\pm0.07_x10^{-5}$	$4.28\pm0.48_x10^{-5}$
T_C (°K)	327 ± 3	319.5 ± 9.9	321 ± 6	324 ± 6
MNE(meV)	26.7 ± 0.2	26.1 ± 0.8	25.8 ± 0.3	26.5 ± 0.5

Reviewing the results of the copper–series, it is immediately clear that while 6CuPc, 10CuPc and 10CuTBAP have about the same median values of m, the median value of m for 6CuTBAP is reduced. Interestingly, the Vg-independent mobility is enhanced relative to others, suggesting that this arises from improved crystallinity.

The 10CuPc and 10CuTBAP materials exhibit a remarkable reduction of the mobility vs. the 6-series indicating that the larger substituent makes charge transport less effective. This suggests that the presence of eight longer chain lengths in the 10-series vs. the eight shorter chain lengths in the 6-series will occupy more space. The distance between adjacent molecules will therefore increase, thereby disadvantaging the charge transfer process. Others have attributed this to the transfer integral, and also to the reorganisation energy [10, 11].

Comparing the 6CuPc with the 6CuTBAP, a single aza-N atom is replaced by CH. The larger μ_0 in the Pc-analogues with a non-aza group is most likely to result from the carbon atom facilitating better intermolecular π-π stacking between neighbouring molecules. A reduction in this molecular distance would then increase the transfer integral and hence charge carrier transfer would become more efficient. This effect also seems to be apparent when 10CuPc is compared with 10CuTBAP.

The values of the contact resistance parameters, Ro and Rx, are very similar in the 6-series cases, and also similar for the 10-series. There is a 2 order of magnitude difference between the 6- and 10-

series, which roughly tracks the trend in the mobility. Although not relevant to Table 5.14, other models exploring gate leakage showed that R_L in all cases is many orders of magnitude larger than the contact resistance. Hence, the variation across the series did not influence the other parameter values significantly.

According to ref. 4, the mobility for an unsubstituted annealed CuPc is $1.8*10^{-4}$ cm^2/Vs[4], but when short chain length substituents occupy peripheral positions the mobility increases, and as the chain length is increased the mobility begins to decrease. A similar result has been obtained from the experimental results presented in this chapter. Variations in molecular film morphology should be visually evident when replacing a nitrogen atom by a carbon atom or by increasing a substituent chain length. However, images of film morphology for these materials were not available to this study. Furthermore, the process by which a film is created can strongly influence the final morphology of the film; traditional spin-coating was the technique that has been used to deposit the film in the samples described here.

The contact resistances (R_S, R_D) are also interesting for characterising the organic material in an OTFT device since they monitor the injection of charge carriers to- and from the electrode materials. The underlying parameters R_O and R_X determine the voltage dependent R_D and R_S when the Schottky effect is present; the values of R_D and R_S in the tables above are given for the maximum values of V_{DS} and V_{GS} in the experiment. These values of R_D and R_S are almost the same for a device with 6CuPc and 6Cu-TBTAP films and exhibit only a marginal Schottky effect. Overall for the 10-series there is a two order magnitude increase in (R_D+R_S) as the chain length increased. There is a pronounced Schottky effect for 10CuPc and 10CuTBTAP. However, R_O and R_X behave differently within this pair, and do not reflect the relative order of the mobilities (see Table 5.14). One concludes that the structural detail of the metal-organic monolayer and the structural difference of the bulk material interfacing with this monolayer exerts a dominant control.

Devices showing high R_X values suggest that the HOMO level of the organic semiconductor is not close to the Fermi level of drain or source electrode (typically gold), and possibly the contact of the metal-organic monolayer is less intimate. In 6CuPc and 6CuTBTAP we may assume that the HOMO levels are similar, so that R_D and R_S take very similar relatively low values (~$10^6\Omega$) and a small Schottky effect. In the case of the 10CuPc and 10CuTBTAP the longer chain lengths clearly influence the injection rates as a result of being less closely bound to the electrode surface. The typical Rd, Rs are at least two orders of magnitude larger than for the 6-series, which may be easily explained by this effect. In 10CuPc, there is a significantly larger Schottky effect than in 10CuTBTAP, which suggests a larger HOMO shift relative to the gold Fermi level, or a more distant, or tilted, contact between the metal surface and organic monolayer. However, the passive contact component, R_O, is significantly larger for 10CuTBTAP, which suggests a different intermolecular arrangement in the bulk material.

The electric fields provided by V_{DS} and V_{GS} affects the energy of an electron in the HOMO level relative to the Fermi level of the electrode, and therefore the corresponding injection rates. Electron

injection into a device with a 6-series active layer is seen to be more efficient than for a 10-series device. Importantly, this will contribute to a reduction of the device switching speed. However, this explanation may not correlate with the current understanding of V_T [12], where the values for 6CuPc, 6Cu-TBTAP, 10CuPc and 10Cu-TBTAP are increased accordingly from 2.3V and 5.3V, to 18.2V and 20.7V, respectively.

Accepting that a factor in the formation of contact resistance is the mismatch between the HOMO of organic semiconductor and the work function of the metal drain electrode, it has been previously proposed [13] that contact resistance is also dependent on gate voltage. When the V_{DS} is kept constant, the carrier concentration increases around the drain electrode region as a result of an increase in the gate voltage. This leads to a reduction in the width of the Schottky barrier and so at a higher gate voltage, the contact resistance decreases [14, 15, 16]. An energy barrier increase as a result of an induced density of interface states will lead to an increased contact resistance. The contact resistance itself acts as an energy barrier which hinders electrons from being injected into the organic active layer from the gold electrode.

The μ_0 for shorter chain length substituted materials such as 6CuPc and 6CuTBTAP is two orders of magnitude higher than a semiconductor with longer chain length, such as 10CuPc and 10Cu-TBTAP. Introducing a substituted group with shorter C6-chain is able to allow a better molecular pi-pi stacking than the substituted group with longer C10- chain. 6CuPc and 6CuTBTAP are known to adopt an edge-on disposition with respect to the dielectric substrate [4]. If 10CuPc and 10CuTBTAP have a similar disposition, the larger substituent chain lengths may cause the molecules to be tilted away from the vertical by larger angles, or cofacially rotated, owing to the larger distance between neighbouring molecules. The energetic disorder increases as the substituted side chain increases, and this would be expected to cause a reduction of mobility. The 10CuTBTAP film shows higher mobility than for the 10CuPc film which suggests that the CH substitution in the 10CuTBTAP frame may provide a lower energy cofacial arrangement with its neighbours, and consequently a more efficient pi-pi stacking. 10CuPc may then exhibit an increase in energetic disorder that may lower 10CuPc film mobility.

The organic semiconductors are characterised by both Tc and MNE. T_C defined by the exponential distribution of traps, or the width of the Gaussian tail density–of–states (DOS). Both T_C and MNE parameters are correlated with the m-value. According to [17], T_C indicates how disordered the semiconductor film is and becomes higher for more disordered situations. In addition, MNE is representative of the width of the DOS distribution (σ) in the conductive channel of an organic semiconducting film. In Table 5.14 both T_C and MNE values are listed for each sample. The MNE and T_C of a device with 6CuPc's film are obtained at 327K and 26.7meV, respectively. However, both MNE and T_C values of 6Cu-TBTAP's film are reduced to 319K and 26.1meV, respectively. The MNE and T_C values for the longer chain lengths in 10CuPc and 10CuTBPAB films are the same as 6CuPc to within experimental error. This indicates that the 6Cu-TBTAP shows better film morphology than all the others, and the number of trap states is lower. This implies that in appropriate situations (i.e. short chain substituents) better film morphologies are obtained when a CuPc's aza-N is replaced by a CH

moiety. AFM images of other CuPc materials not studied in this work have revealed the surface roughness of the organic semiconductor layer [18].

The power dependence γ is related to m and $\gamma = 2m$ (see section 2.5 and equation 2.5.2.22). For perfect crystalline films both γ and m are close to zero and the field-dependent mobility (μ_{eff}) is also calculated using $\mu_{eff} = \mu_o (V_{GS} - V_T)^{\gamma}$ this indicates that an applied transverse electric field influences the Gaussian DOS distribution of organic semiconductors.

Figure 5.11 shows mobility as a function of gate voltage. At the lower gate voltage, the mobility increases exponentially with V_{GS} for both the linear and saturation regions at V_{DS} = -5V and V_{DS} = -40V or -45V, respectively. This result is expected since carriers gain more energy at the grain boundary as gate voltage increases, therefore additional charge may contribute to the delocalized band mobility in the accumulation layer of the semiconductor [19, 20].

It is recognised that organic semiconductors have a greater number of grain boundaries compared with inorganic semiconductors, and these cause an energy barrier to mobility. The holes carrying charge need to overcome this barrier and this could be done by increasing the gate voltage. Alternatively, the height of the potential barrier may decrease with increasing gate voltage [21, 22], so that thermally-activated mobility increases exponentially. This explains that carrier mobility can increase as a result of an increase in the carrier concentration at higher gate voltage. In this case, trapped carriers become free and a higher number of carriers contribute to the charge flow.

Also, in figure 5.11 one notices that carrier mobility for the saturation regime is greater than for the linear regime. This result is consistent with previous publications [23,24], clearly, since the two transfer experiments span approximately the same range of V_{GS}-V_T, the relationship between the μ_{eff}'s in the two regimes is governed predominantly by the field-independent μ_0's.
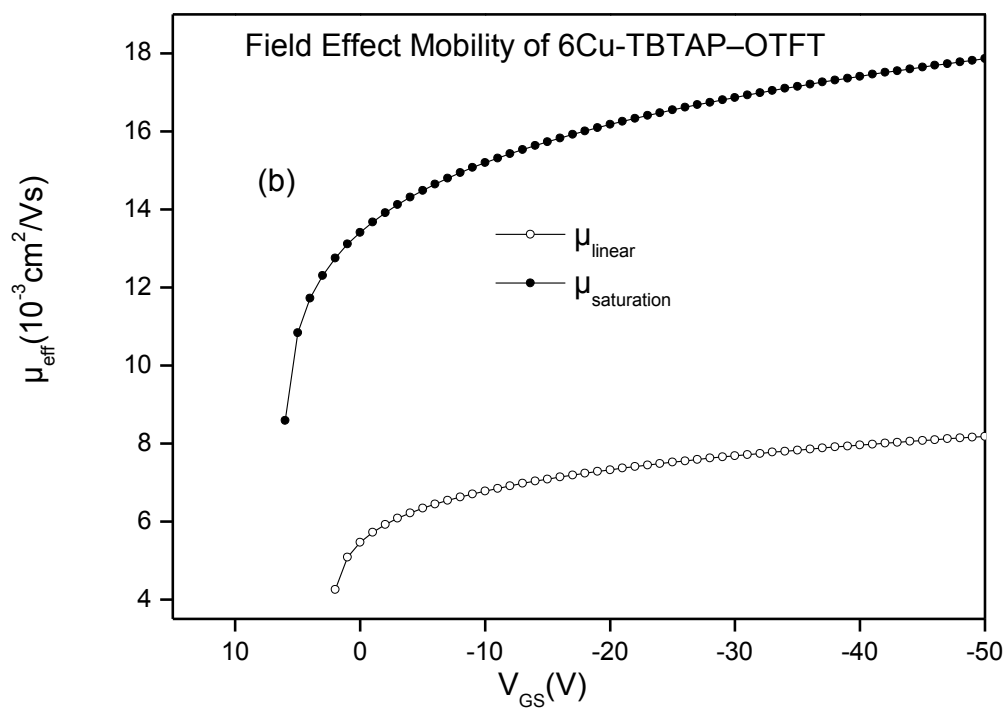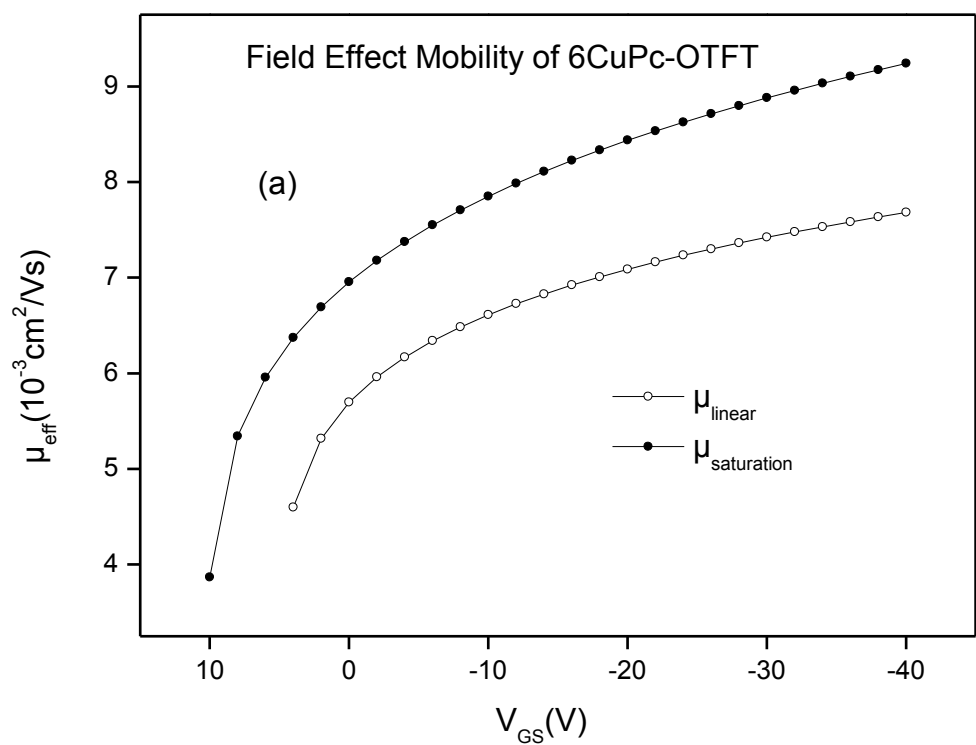
Figure 5.11. Plot of the V_G-dependent mobility, μ_{eff}, as function of V_G for (a) 6CuPc- OTFT and (b) 6Cu-TBTAP –OTFT.

In Table 5.14 this is recognised as a difference in the extracted K' parameters, which reflect the values of μ_0. The expressions thus far used make the underlying assumption that K' and V_T will be constants of the material; when this is not the case a modified approach to extracting parameters is required. This would have the disadvantage of introducing still more parameters than presently used. For example, in the case of K' and μ_o, a variation can occur as a result of the Poole-Frenkel effect [25], where μ_0 takes the form: $\mu_0 = \mu_{00}.\exp\{ k_v.\sqrt{V_{DS}})$. Alternatively, if the Poole Frenkel effect is negligible, but V_T is a function of the lateral and transverse fields, this will affect the extraction analysis to a degree where the K' value becomes distorted; output experiments, which sweep V_{DS} whilst sweeping the full voltage range, will deliver quite inconsistent values of both K' and V_T. This point has been barely recognised in the OTFT literature in the last 2 decades, but explains why output data has found little use!

References

[1] Chaure, N.B., Basova, T., Zahedi, M., et al. (2010) 'Solution processed tetrasubstituted zinc phthalocyanine as an active layer in organic field effect transistors', *J.Appl.Phys.*,**107**(**11**),**114503**, doi:10.1063/1.3428386.

[2] Raja,M. and Eccleston,W. (2011) 'Analytical device models for disordered organic Schottky diodes and thin-film transistors for circuit simulations', *IET Circuits Devices Syst.*, **6**(**2**),**122**,doi: 10.1049/iet-cds.2011.0199.

[3] Tejada, J.A.J., Varo, P.L., Cammidge, A.N., et al. (2017) 'Compact modeling of organic thin-film transistors with solution processed octadecyl substituted tetrabenzotriazaporphyrin as an active layer', *IEEE Trans. Electron Devices*,**64**(**6**),**2629**, doi: 10.1109/TED.2017.2690976.

[4] Wang,Y.,Liu,X.,Shan,H., et al. (2017) 'Tetra-alkyl-substituted copper (II) phthalocyanines as dopant-free hole-transport layers for planar perovskite solar cells with enhanced open circuit voltage and stability', *Dyes Pigm.*, **139**, **619**-**626**, doi: 10.1016/j.dyepig.2016.12.067.

[5] Chaure N.B., Cammidge, A.N., Chambrier,I., et al. (2011) 'High-mobility solution-processed copper phthalocyanine-based organic field-effect transistors',*Sci.Technol.Adv.Mater.*,**12**(**2**),**025001**, doi:10.1088/1468-6996/12/2/025001.

[6] See,E.G. Glantz, S.A.and Slinker, B.K., (1990) 'Primer of Applied Regression and Analysis of Variance' pp.248, McGraw Hill Inc.,New York (1990).The Wikipedia entry under 'Coefficient of Determination' also provides a good introduction.

[7] Winscom, C J., Harris P G. and Silver J. (2016) 'Non-passive behaviour of equivalent circuit components in AC Powder Electroluminescence (ACPEL) Lamps', *ECS J.Solid State Sci.Technol.* **5** (**12**),R**211**-R**218**,doi: 10.1149/2.0201612jss .

[8] Roy, K. et al. (2015) 'A Primer on QSAR/QSPR Modeling.' Chapter 2 'Statistical methods in QSAR/QSPR' p:37-59 SpringerBriefs in Molecular Science, doi 10.1007/978-3-319-17281-1_2.

[9] Press,W.H., Flannery,B.P., Teukolsky, S.A.and Vetterling, W.T. (1986). 'Numerical Recipes' p301, Cambridge University Press, Cambridge.

[10] Dong, H., Fu, X., Liu, J., et al., (2013) '25th Anniversary Article: Key Points for High-Mobility Organic Field-Effect Transistors', *Adv. Mater.*,**25** (**43**),**6158**, doi: 10.1002/adma.201302514.

[11] Newman, C.R., Frisbie, C.D., Da Silva, D.A., et al. (2004) 'Introduction to organic thin film transistors and design of n-channel organic semiconductors',*Chem.Mater.*,**16**(**23**),**4436**,doi: 10.1021/cm049391x.

[12] Etschmaier, H., Pacher, P., Lex, A., et al. (2009) 'Continuous tuning of the threshold voltage of organic thin-film transistors by a chemically reactive interfacial layer', *Appl. Phys. A.*, **95**(**1**), **43**, doi 10.1007/s00339-008-4995-z.

[13] Horowitz, G., (2004) 'Organic thin film transistors: from theory to real devices', *Mater. Res. Technol.*,**19**(**7**),**1946**,doi: 10.1557/JMR.2004.0266.

[14] Jo, G., Maeng, J., Kim, T-W., et al. (2007) 'Channel-length and gate-bias dependence of contact resistance and mobility for In2O3 nanowire field effect transistors', *J. Phys. D.*, **102** (**8**), **084508**, doi: 10.1063/1.2799960.

[15] Cherian, S., Donley, C., Mathine, D., et al. (2004) 'Effects of field dependent mobility and contact barriers on liquid crystalline phthalocyanine organic transistors', *J. Appl. Phys.*,**96**(**10**),**5638**, doi: 10.1063/1.1803945.

[16] Pfattner, R., Rovira, C., Mas-Torrent, M. (2015), 'Organic metal engineering for enhanced field-effect transistor performance', *Phys. Chem. Chem. Phys.*,**17**(**40**), **26545**, doi: 10.1039/c4cp03492a

[17] Raja, M., Donaghy, D., Myers, R. et al. (2012) 'Impact of universal mobility law on polycrystalline organic thin-film transistors', *J. Appl. Phys.*, **112** (8), **084503**,doi: 10.1063/1.4758182.

[18]Yakuphanoglu,F.,Caglar,M.,Caglar,Y., et al. (2010) 'Improved mobility of the copper phthalocyanine thin-film transistor',*Synth.Met.*,**160**(**13**),**1520**,doi: 10.1016/j.synthmet.2010.05.013.

[19] Dong,G., Miyadera,T., Ikeda,S., et al. (2007) 'Analysis of charge transport in a polycrystalline pentacene thin film transistor by temperature and gate bias dependent mobility and conductance', *J. Appl. Phys. D* , **102**(**2**), **023706**, doi: 10.1063/1.2753671.

[20] Natali, D., Fumagalli, L., Sampietro, M. (2007) 'Modeling of organic thin film transistors: effect of contact resistances' *J. Phys. D*, **101**(**1**), **014501**, doi: 10.1063/1.2402349.

[21] Amorim,C.A., Cavallari,M.R.,Santos,G., Fonseca,F.J., Andrade,A.M. and Mergulhao,S. (2012) 'Determination of carrier mobility in MEH-PPV thin-films by stationary and transient current techniques', *J. Non-Cryst. Solids*, **358**(**3**),**484**, doi: 10.1016/j.jnoncrysol.2011.11.001.

[22] Guo, D., Miyadera, T., Ikeda, S., et al. (2007) ' Analysis of charge transport in a polycrystalline pentacene thin film transistor by temperature and gate bias dependent mobility and conductance' *J. Appl. Phys.*, **102** (**2**), **484**, doi: 10.1063/1.2753671.

[23] Shea, P.B., Kanicki, J., Ono, N. (2005) 'Field-effect mobility of polycrystalline tetrabenzoporphyrin thin-film transistors' *J. Appl. Phys.* **98** (**1**), 014503,doi: 10.1063/1.1949713.

[24] Hamilton,M. ,Martin,S. and Kanick,J. (2004) 'Field effect mobility of organic polymer thin-film transistors', *Chem. Mater.*,**16** (**23**), **4699**, doi: 10.1021/cm049613r.

[25] Locci,S., Morana, M.,Orgiu, E., et al. (2008) 'Modeling of Short-Channel Effects in Organic Thin-Film Transistors', *IEEE Trans. Electron Devices*, **55**(**10**), **2561**, doi: 10.1109/TED.2008.2003022.

6. ANNEALED MONO-PC'S AND AS-DEPOSITED BIS-PC'S.

In this chapter the effect of annealing ZnPc and PbPc materials is considered with respect to their characteristics. Also, one example of a bis-phthalocyanine arrangement (GdPc$_2$) is handled to examine the properties of a material with a different structure.

6.1   Non-peripheral ZnPc-OTFT's

A mono- ZnPc is similar to CuPc, they both have a planar structure and can be used as an active layer in the fabrication of OTFT devices. The structure of the p-type semiconductor of both non-peripheral ZnPc and peripheral ZnPc are shown in figures 6.1 and 6.3, respectively. For purposes of comparison, the as-deposited non-peripheral (bay)-substituted ZnPc is considered first, and thereafter the peripheral-substituted analogue as both as-deposited and annealed are examined.
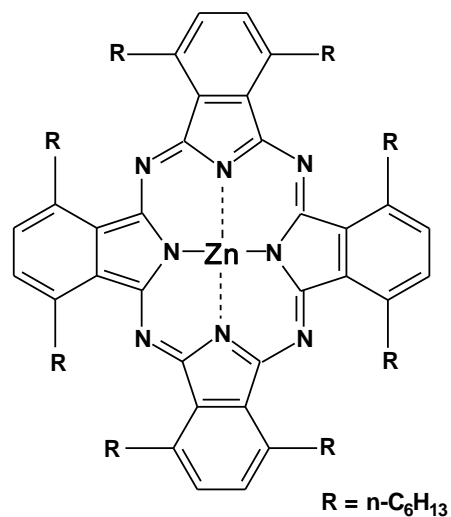

$R = n\text{-}C_6H_{13}$

Figure 6.1. Non-peripheral (bay position) [1].

Electrical measurements of the non-peripheral ZnPc of OTFTs were carried out using the same procedure as the procedure used with Cu-series in chapter 5. The OTFT dimensions in this device were L=10µm, W=10mm and C$_i$=17nF/cm^2. For non-peripheral ZnPc - OTFTs, both the 4PA and 5SC models were used to simulate both the linear and saturation region. The experimental and the 4PA-simulated data is presented in figure 6.2 and the extracted parameters are listed in Table 6.1. The results are indistinguishable from those using the 5SC model and presented in Table 6.2, and the values of Table 6.1 will be used in Table 6.3. The analytical models were fit with the experimental function for the linear region (V$_{DS}$=-5V) and the saturation region (V$_{DS}$=-40V) where the experimental

results were affected by experimental noise or digitizing errors. Hence, the fitting errors were found to be larger than expected at 5.0% and 6.6% for the linear region and the saturation region, respectively.
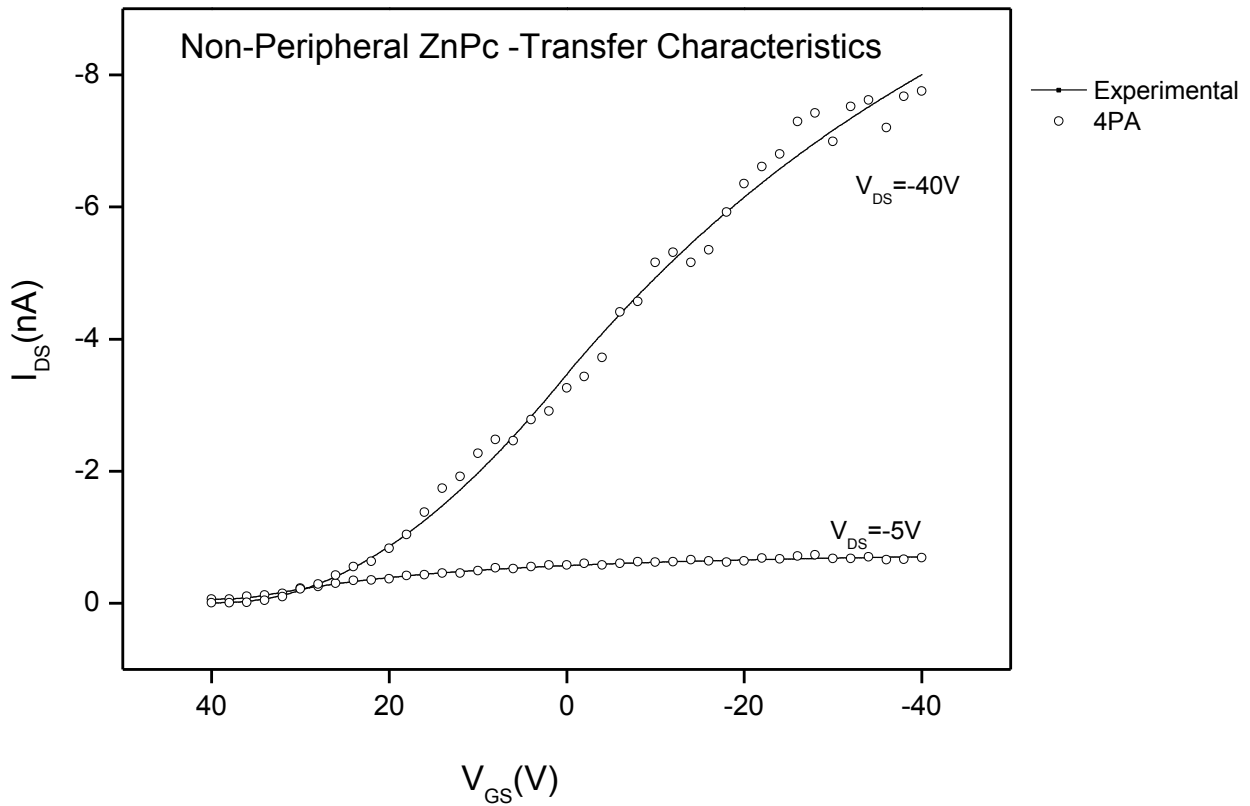

Figure 6.2. I_{DS} vs. V_{GS} transfer characteristics for non-peripheral ZnPc for $V_{DS}=$ –5V and -40V, respectively; experimental data (open circle), 5SC modelled data (solid line).

Table 6.1. OTFT extracted parameters for as-deposited non-peripheral ZnPc films of $V_{DS}=$-5V and -40V using the 4PA model.

Non-Peripheral ZnPc								
4PA								
V_{DS}	K'	$V_T(V)$	m	R_{DS} (Ω)	$\mathscr{R}^2$	Err(%)	$R_D(\Omega)$	$R_S(\Omega)$
-5V	$1.72\pm$ $0.24_x10\text{-}11$	$39.1\pm$ 0.2	$0.10\pm$ 0.02	$6.36\pm$ 0.02_x10^8	$0.9913 \pm$ 0.0001	$5.0\pm$ 0.2	$3.18\pm$ 0.05_x10^8	$3.18\pm$ 0.05_x10^8
-40V	$1.42\pm$ 0.39_x10^{-11}	$39.6\pm$ 0.6	$0.10\pm$ 0.02	$2.62\pm$ 0.19_x10^8	$0.9938\pm$ 0.0001	$6.6\pm$ 0.1	$1.31\pm$ 0.09_x10^8	$1.31\pm$ 0.09_x10^8

Table 6.2. OTFT extracted parameters for as-deposited non-peripheral ZnPc films of V_{DS}=-5V and -40V using the 5SC model.

| | | | | Non-Peripheral ZnPc | | | | | |
| | | | | 5SC | | | | | |
V_{DS}	K'	V_T(V)	m	$R_O(\Omega)$	$R_X(\Omega)$	$\mathscr{R}^2$	Err (%)	$R_D(\Omega)$	$R_S(\Omega)$
-5V	$1.71\pm 0.27_x10^{-11}$	39.2 ± 0.1	0.10 ± 0.02	$6.22\pm 0.10_x10^8$	$4.68\pm 0.29_x10^6$	0.9913 ± 0.0018	5.0 ± 0.3	$3.14\pm 0.03_x10^8$	$3.21\pm 0.09_x10^8$
-40V	$1.41\pm 0.37_x10^{-11}$	39.5 ± 0.1	0.10 ± 0.02	$2.53\pm 0.75_x10^8$	$7.76\pm 0.78_x10^5$	0.9938 ± 0.0023	6.6 ± 0.1	$1.27\pm 0.37_x10^8$	$1.32\pm 0.01_x10^8$

The K' values of the linear region compared with the saturation region are the same to within experimental error. This leads the μ_o for the linear and the saturation regions also to be the same. Similarly, the V_T and m-values are found to be the same for both regions. (This analysis was also performed using the 5SC method with the same result and showed that the Schottky effect was negligible.) According to the R_D and R_S -values from linear and saturation regions, the non-peripheral ZnPc-OTFT device shows a typical reduction in going to the higher V_{DS}-value. Compared with the non-peripheral Cu-series, the non-peripheral ZnPc shows lower mobility.

Table 6.3. OTFT extracted parameters for as-deposited non-peripheral ZnPc films of V_{DS}=-5V and -40V using the 4PA model.

| | | Non-peripheral ZnPc | | | |
| | | 4PA model | | | |
V_{DS}	K'	m	μ_o (cm^2 V^{-1}s^{-1})	T_c (^{o}K)	MNE(meV)
-5V	$1.72\pm0.24_x10^{-11}$	0.1 ± 0.02	$2.03\pm0.45_x10^{-6}$	330 ± 13	27.0 ± 1.0
-40V	$1.42\pm0.39_x10^{-11}$	0.1 ± 0.02	$1.67\pm0.45_x10^{-7}$	330 ± 13	27.0 ± 1.0

The m-value obtained from V_{GS}=-10V for the output analysis, where the denominator was 1.38, was 0.10±0.02. In the transfer experiment, the denominator for the linear region >> 3 but the denominator for the saturation region is 2.09, so inaccuracies in the determination of K' and m are expected. Both the Tc and MNE is almost the same for linear and saturation region.

6.2   Peripheral ZnPc-OTFT's

Peripheral-ZnPc is also a p-type semiconductor and used in OTFT devices, the molecular structure is shown in figure 6.3. The peripheral ZnPc-OTFT device was annealed at 70°c, annealing is one of the techniques used to improve the organic semiconductor film morphology, thus improving the overall OTFT device characteristics.
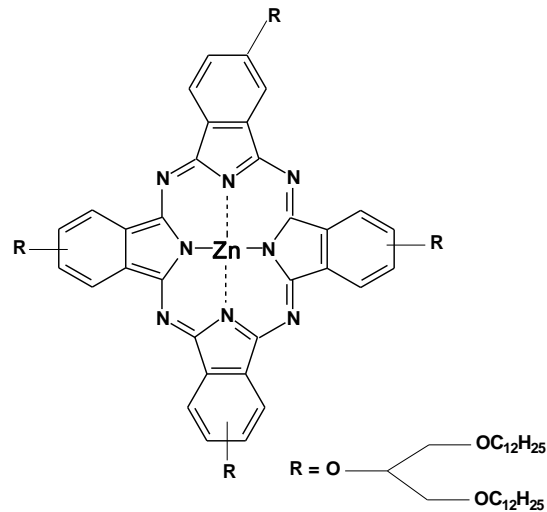

Figure 6.3. Molecular structures of Peripheral ZnPc [2].

The OTFT dimensions in this device were L=10µm, W=1mm and C_i=10nF/cm^2 [2]. The electrical measurement of the peripheral ZnPc OTFT device was analysed using 5SC and the extracted device parameters are listed in Table 6.4 & 6.5. The fitting errors were improved for the linear and the saturation regions from 6.3% to 5.1% and from 4.3% to 3.1%, respectively, after the film was annealed at 70°C. However, poor fitting of the modelled data for both as-deposited and annealed films are mainly due to experimental errors, see Figure 6.4.
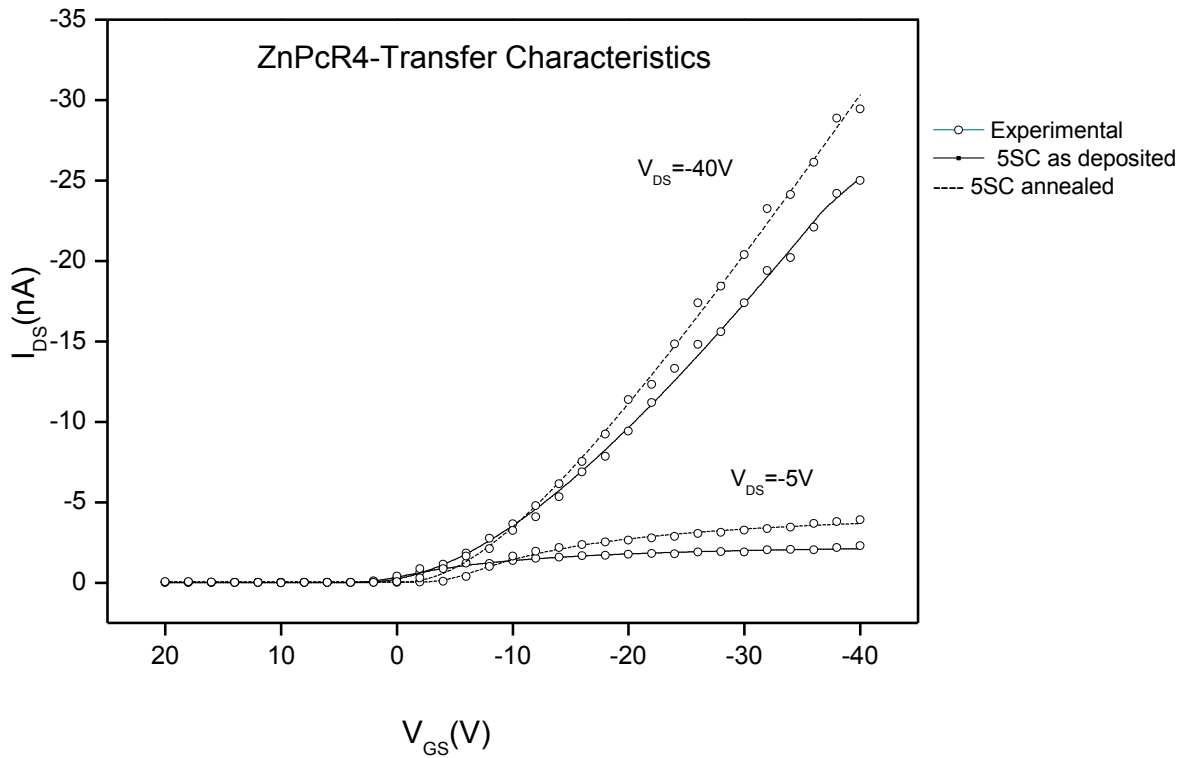
Figure 6.4. I_{DS} vs. V_{GS} transfer characteristics for peripheral ZnPc films for $V_{DS}=$ –5V and –40V; experimental data (open circle), 5SC modelled data (solid line for as deposited and broken line for annealed at 70°C).

Table 6.4. OTFT extracted parameters for as-deposited and annealed peripheral ZnPc-OTFT of V_{DS}=-5V and V_{DS}=-40V using 5SC model.

Peripheral ZnPc										
5SC										
V_{DS}	K'	V_T (V)	m	$R_O(\Omega)$	$R_X(\Omega)$	$\mathscr{R}^2$	Err (%)	D	$R_D(\Omega)$	$R_S(\Omega)$
as deposited										
-5V	$1.54\pm 0.65_x10^{-11}$	4.5 ± 0.1	0.077 ± 0.015	$1.88\pm 0.02_x10^9$	$2.06\pm 0.02x10^7$	0.9956 ± 0.0001	6.3 ± 0.1	5.9 ± 0.3	$9.53\pm 0.12_x10^8$	$1.01\pm 0.01x10^9$
-40V	$1.75\pm 0.17_x10^{-11}$	3.4 ± 0.1	0.077 ± 0.015	$8.52\pm 0.06x10^8$	$1.86\pm 0.06_x10^6$	0.9989 ± 0.0001	4.3 ± 0.1	2.3 ± 0.5	$4.27\pm 0.03x10^8$	$4.33\pm 0.03x10^8$
annealed at 70°C										
-5V	$2.64\pm 0.18_x10^{-11}$	1.7 ± 0.1	0.057 ± 0.012	$9.98\pm 0.08_x10^8$	$1.01\pm 0.05_x10^7$	0.9958 ± 0.0001	5.1 ± 0.1	4.1 ± 0.1	$5.06\pm 0.05x10^8$	$5.27\pm 0.07x10^8$
-40V	$4.31\pm 0.24x10^{-11}$	-0.45 ± 0.1	0.057 ± 0.012	$8.62\pm 0.03_x10^8$	$1.43\pm 0.02x10^6$	0.9989 ± 0.0001	3.1 ± 0.1	3.4 ± 0.1	$4.32\pm 0.02x10^8$	$4.36\pm 0.02x10^8$

The denominator for the linear region, for both as-deposited and annealed materials is much larger than that for the saturated region for all models. However, the denominator for the saturation region is below the acceptable value 3 (as the limit for accurate extraction of m and K'), in both the as-deposited and annealed films.

For the as-deposited non-peripheral ZnPc-OTFT, the K' value was found to be higher in the linear region than the K' value in the saturation region. However for non-peripheral ZnPc-OTFT the K' value is higher for the saturation region in both as-deposited and after annealed. The V_T is negatively shifted after the film is annealed for both the linear and the saturation region. The m-value is similarly reduced after the film is annealed at 70°C for both the linear and saturation regions; this may be an indication of improved film morphology. After annealing, the R_D and R_S are almost similar in magnitude, in both the linear and saturation regions, this demonstrates that the peripheral ZnPc-OTFT device did not exhibit the Schottky effect. Before annealing, there is a small Schottky effect in the saturation region (V_{DS}=-40V). Generally, the fundamental parameters, Ro and Rx are reduced after the film is annealed.

After annealing, μ_o increases by a factor of 1.7 and 3.3 for the linear and the saturation regions, respectively. It is possible that the as-deposited film morphology absorbs moisture, which facilitates the trapping of charge carriers; after annealing this would be reduced.

Table 6.5. OTFT extracted parameters using the 5SC model for as-deposited and annealed peripheral ZnPc-OTFT at V_{DS}=-5V and -40V.

Peripheral ZnPc					
5SC model					
	K'	m	μ_o (cm^2 V^{-1}s^{-1})	T_c (^{o}K)	MNE(meV)
V_{DS} = -5V as deposited	$1.54\pm0.65_x 10^{-11}$	0.077 ± 0.015	$3.08\pm0.26_x10^{-5}$	323.1 ± 4.5	26.4 ± 0.4
V_{DS} =-40V as deposited	$1.75\pm0.17_x 10^{-11}$	0.077 ± 0.015	$3.49\pm0.34_x10^{-5}$	323.1 ± 4.5	26.4 ± 0.4
V_{DS} =-5V annealed at 70°C	$2.64\pm0.18_x 10^{-11}$	0.057 ± 0.012	$5.28\pm0.37_x10^{-5}$	317.1 ± 3.6	25.9 ± 0.3
V_{DS} =-40V annealed at 70°C	$4.31\pm0.24_x 10^{-11}$	0.057 ± 0.012	$8.62\pm0.47_x10^{-5}$	317.1 ± 3.6	25.9 ± 0.3

In comparison with the non-peripheral ZnPc film, the peripheral ZnPc film shows a better performance. On the basis of the m-values, the peripheral ZnPc-OTFT has an improved crystallinity and the μ_o is greater by one order of magnitude when compared with non-peripheral ZnPc-OTFTs.

The V_T of the non-peripheral ZnPc-OTFT shifted to a more positive value by roughly 34V, when compared with the peripheral ZnPc film device. In addition to this, the R_D and R_S of the OTFT device with a non-peripheral ZnPc film were both lower by a factor of 3, compared with the OTFT device with a peripheral ZnPc film. In general, the OTFT device with peripheral ZnPc showed preferable characteristics. Overall the extracted parameters from annealed devices were found to have improved when compared with their non-annealed counterparts in both the linear and saturation regions.

6.3   C6PbPc –OTFT's

A similar manufacturer's template was used to produce a C6PbPc-OTFT device. The molecular structure of a PbPc semiconductor is non-planar, owing to the much larger ionic radius of the Pb ion (1.33Å) [3] resulting in an out-of-plane placement with respect to the phthalocyanine ligand ring. Thus, the structure is categorised as non-planar, with a "shuttlecock" shape. Molecules that are shuttlecock-shaped may arrange themselves into one of two common stacking arrangements. The central metal ion can either be placed facing away from or towards the neighbouring central metal atom [4]. A smaller distance between central metal ions enables better charge transport. For this reason, stacking the central metal ion towards the neighbouring central metal atom is the preferred molecule arrangement for this process.

However, the C6PbPc molecules studied here are formed with an additional eight alkyl substituents of medium length at the non-peripheral sites on the macrocyclic ring. These substituents may change the overall C6PbPc molecular structure. The large ionic radius of the Pb ion causes it to be more weakly-bonded with the Pc ring [5] than for lighter metal ions, a weak bond may cause more charge transfers to occur [5]. A chemical structure of the C6PbPc in shown in figure 6.5, Nabok et al.[5] have characterised the C6PbPc molecules in their research. They found that the absorption spectrum showed both a Soret–band and a Q-band. Observation of a double peak between 700 and 755 nm is classified as being in Q–band whereas obtaining a single observation peak of 500 nm is regarded as Soret–band [5]
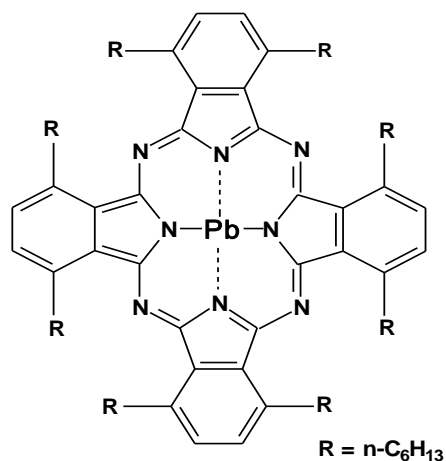
Figure 6.5 Nonperipherally substituted of octakis(hexyl) at 1,4,8,11,15,18,22,25 lead phthalocyanine (C6PbPc) compound (n-hexyl) [5].
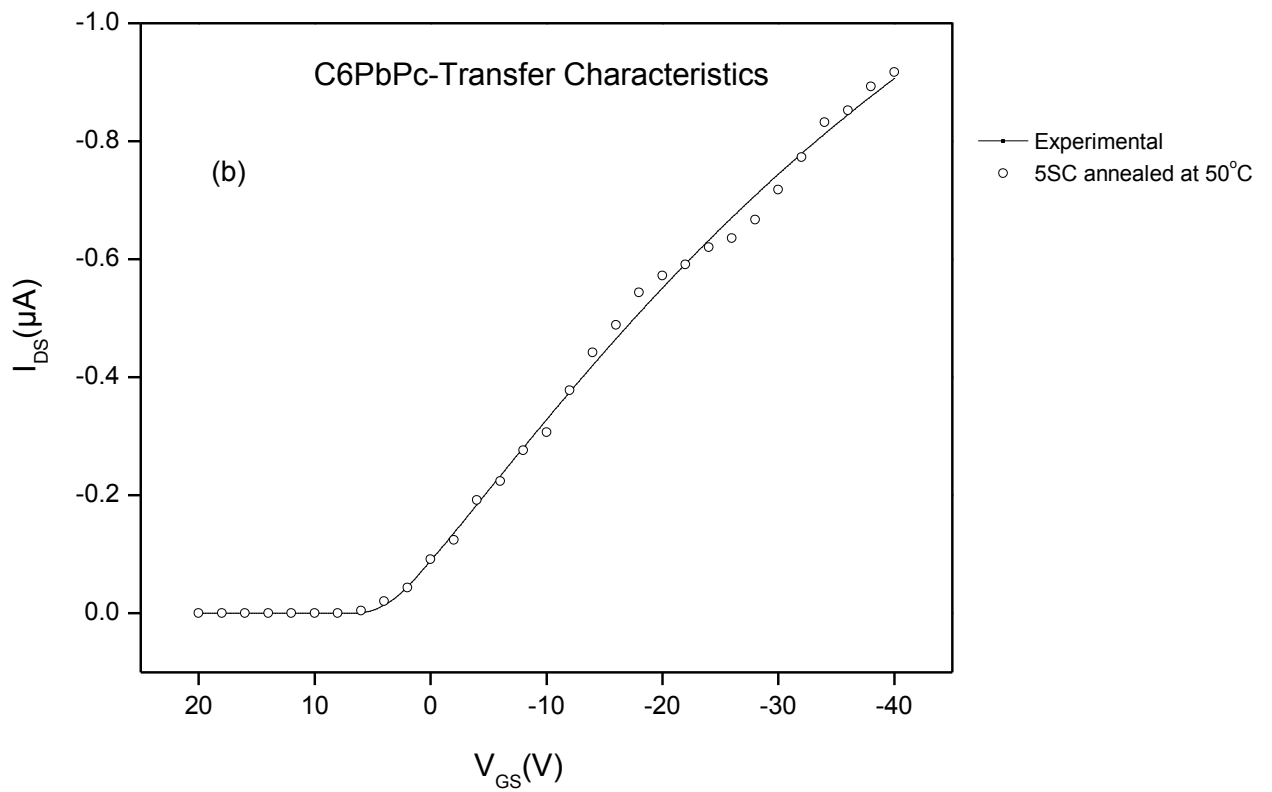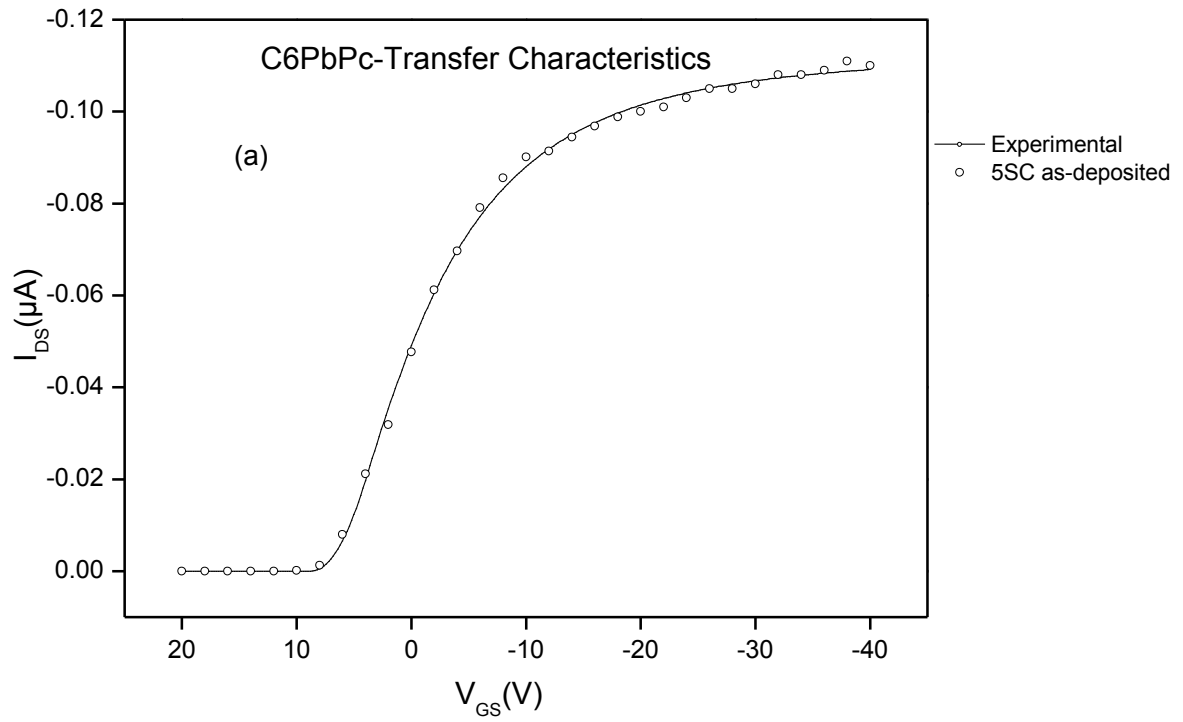
The C6PbPc material was also spin-coated on prefabricated templates for the OTFT devices. The dimensions of the device were L=5μm, W=1mm and C_i=10nF/cm^2. The transfer characteristic (I_{DS} vs. V_{GS}) at V_{DS}=-5V was measured by sweeping V_{GS} from +20V to -40V in 2V intervals. This I-V data was collected and fitted using the 5SC model. This is shown in figure 6.6 (a, (as deposited) and b, c, d and e (annealed)). There is not enough information available on experimental I-V characteristics for the saturation region (V_{DS}=-40V), therefore only the linear region (V_{DS}=-5V) is presented for the C6PbPc-OTFT samples.

As explained in chapter 5 the m and K'-value are poorly determined if the denominators are >> 3. In this case the denominator was found to be >> 3 for the C6PbPc-OTFT device in the linear portion, (V_{DS}=-5V) and as a result the transfer characteristics were characterised by using the m-value from output characteristics, where the denominator involved is <<3. Two values of V_{GS} were chosen initially to try and place the experimental data to have regions of both linear and saturated behaviour. Across the range of as-deposited and annealed samples, the choice V_{GS}= -10V best achieved this goal, and also reflected the best fitting accuracy based on R^2 ,Err, and D. Table 6.6 lists both options, but in the subsequent fitting of the transfer data, the m-value for V_{GS}=-10V is taken with a realistic error range of ±0.02.

Table 6.6. The morphologically important m-parameters obtained from the output characteristics (V_{GS}=-10V and -20V) of transistors for as-deposited and annealed C6PbPc films using the 6SB model, and their fitting accuracy data.

6SB –model				
	m	R^2	Err(%)	D
V_{GS}=-10v as deposited	0.07027	0.999339	2.398	1.45
V_{GS}=-20v as deposited	0.08186	0.999186	3.851	3.76
V_{GS}=-10v annealed at 50°C	0.08851	0.997853	0.928	1.43
V_{GS}=-20v annealed at 50°C	0.1033	0.997708	2.539	1.15
V_{GS}=-10v annealed at 100°C	0.09269	0.997313	1.85	1.66
V_{GS}=-20v annealed at 100°C	0.06523	0.994976	6.598	1.3
V_{GS}=-10v annealed at 150°C	0.08513	0.998552	3.657	1.19
V_{GS}=-20v annealed at 150°C	0.075	0.999562	1.983	1.22
V_{GS}=-10v annealed at 200°C	0.08035	0.998081	5.025	1.21
V_{GS}=-20v annealed at 200°C	0.08936	0.998217	5.299	2.57

The experimental data of as deposited and annealed film was aligned with the model data obtained from the 5SC model (6SB and 5SC are identical for Transfer analyses). The fitting errors were at 3.1% for as deposited and after the film was annealed at 50°C ,100°C,150°C and 200°C the fitting errors were 4.3%, 2.9%, 2.1% and 2.5%, respectively, see figure 6.6 a, b, c, d and e. Table 6.7 presents the extracted C6PbPc-OTFTs device parameters for both as C6PbPc film deposited and annealed at 50°C intervals.

110

C6PbPc-Transfer Characteristics

Experimental
5SC annealed at 100°C

C6PbPc-Transfer Characteristics
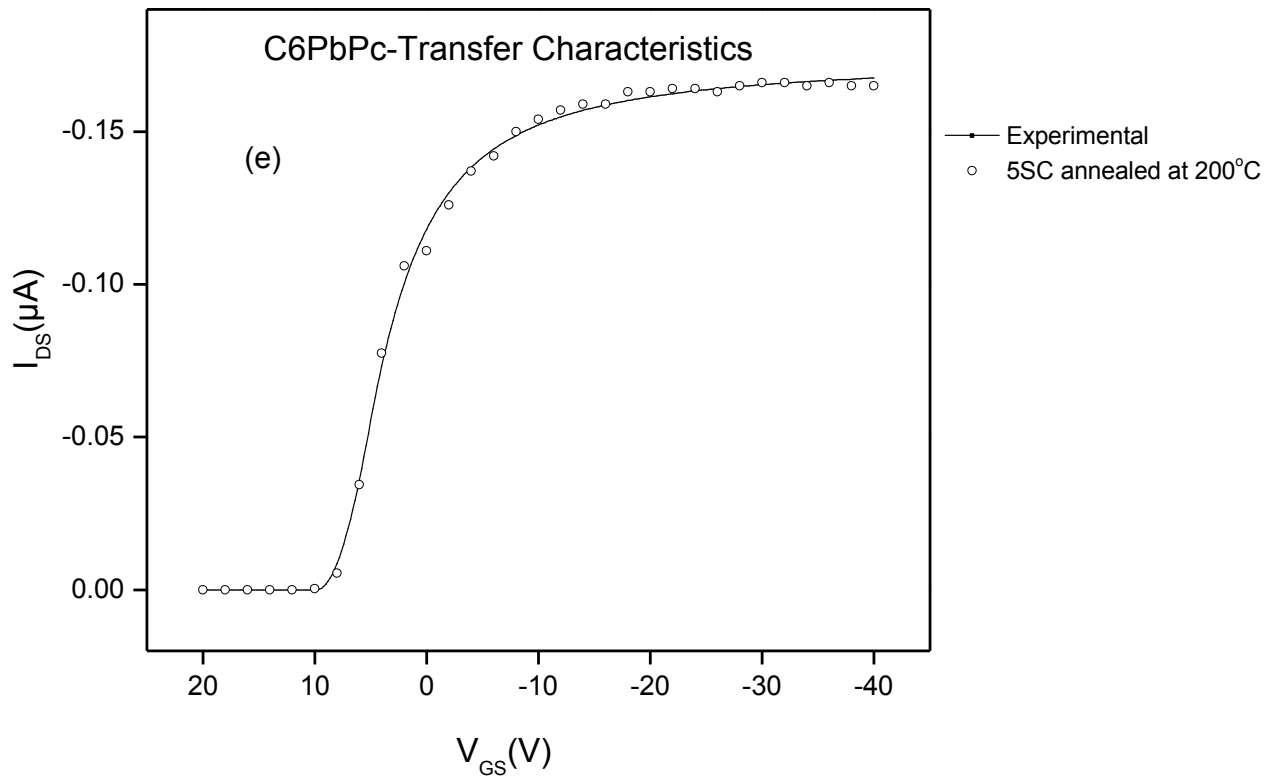
(d)

Experimental
5SC annealed at 150°C
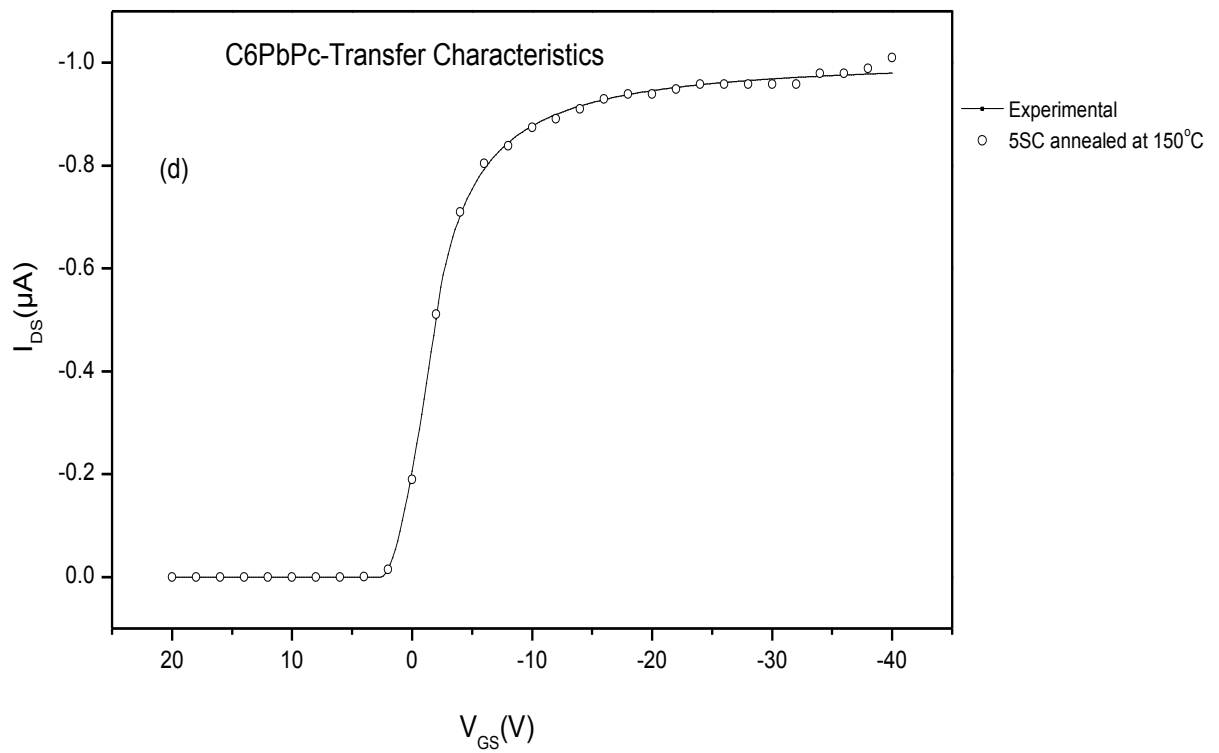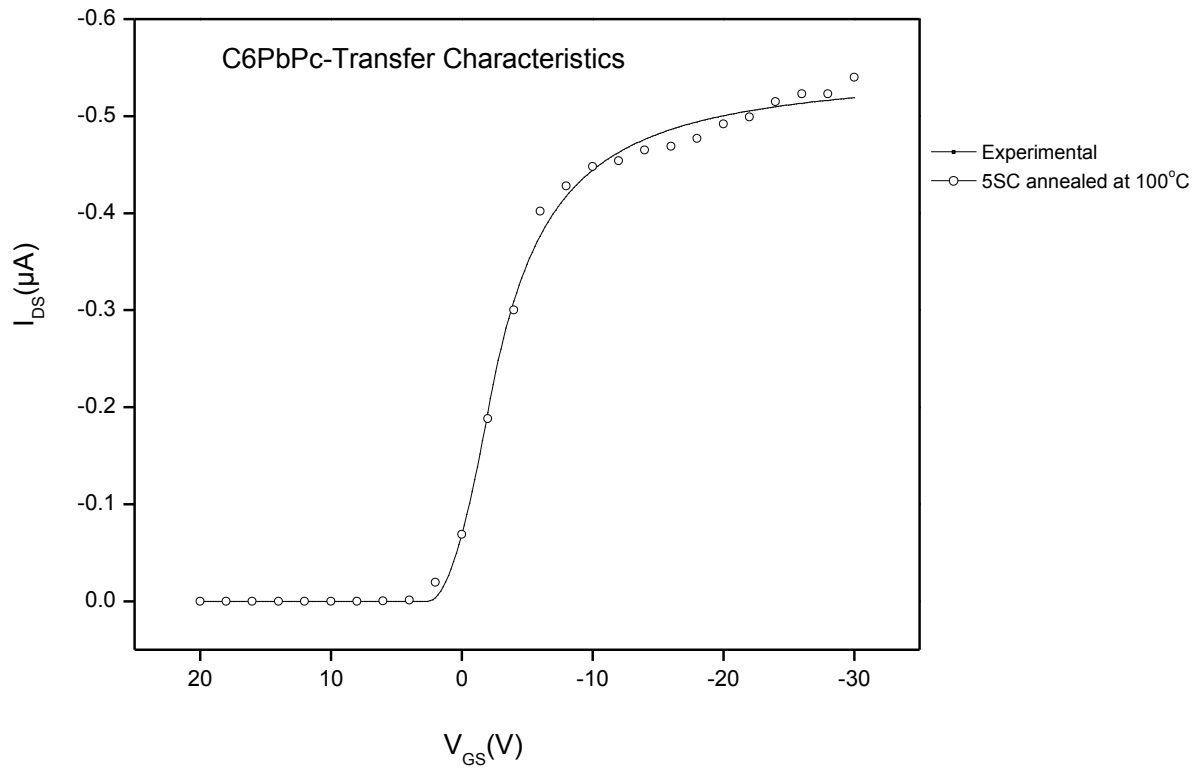
Figure 6.6. I_{DS} vs. V_{GS} transfer characteristics for C6PbPc films for V_{DS}= –5V; experimental data (open circle), 5SC modelled data (a) for as deposited, (b) for annealed at 50°C, (c) annealed at 100°C, (d) annealed at 150°C and (e) annealed at 200°C.

Table 6.7. Extracted parameters for as-deposited and annealed C6PbPc films at V_{DS}=-5V using the 5SC model.

C6PbPc									
5SC									
V_{DS}=-5V	K'	V_T (V)	m	$R_O(\Omega)$	$R_X(\Omega)$	$\mathscr{R}^2$	Err (%)	$R_D(\Omega)$	$R_S(\Omega)$
As deposited	$7.56\pm 0.78_x10^{-10}$	8.8 ± 0.12	0.070 ± 0.02	$2.32\pm 0.09_x10^7$	$7.70\pm 0.03_x10^5$	0.9992 ± 0.0001	3.1 ± 0.1	$1.23\pm 0.05_x10^7$	$2.50\pm 0.01_x10^7$
annealed at 50°C	$1.50\pm 0.23_x10^{-9}$	6.9 ± 0.3	0.089 ± 0.02	$1.80\pm 0.04_x10^6$	$4.73\pm 1.02_x10^4$	0.9975 ± 0.0003	4.3 ± 0.1	$9.31\pm 0.25_x10^5$	$1.06\pm 0.43_x10^6$
annealed at 100°C	$1.02\pm 0.41_x10^{-8}$	2.6 ± 0.1	0.093 ± 0.02	$6.64\pm 0.06_x10^6$	$1.51\pm 0.0_x10^5$	0.9981 ± 0.0001	2.9 ± 0.1	$3.44\pm 0.03_x10^6$	$5.22\pm 0.03_x10^6$
annealed at 150°C	$4.19\pm 0.34_x10^{-8}$	2.7 ± 0.1	0.085 ± 0.02	$4.94\pm 0.0_x10^6$	$6.25\pm 0.56_x10^3$	0.9996 ± 0.0001	2.1 ± 0.1	$2.48\pm 0.01_x10^6$	$2.48\pm 0.01_x10^6$
annealed at 200°C	$2.39\pm 0.13_x10^{-9}$	9.9 ± 0.1	0.080 ± 0.02	$1.88\pm 0.10_x10^7$	$4.96\pm 0.07_x10^5$	0.9987 ± 0.0001	2.5 ± 0.1	$9.84\pm 0.47_x10^6$	$1.73\pm 0.02_x10^7$

In the as-deposited film, the K'- value was found to be 7.56±0.78E-10 for the linear region (V_{DS}=-5v) and this K'-value doubles after the film was annealed at 50°C. Further annealing at 100°C and 150°C leads to very large increases in K' by a factor of 13.49 and 55.42, respectively, relative to the as-deposited position. From the maximum at 150°C, the K' value is then reduced by a factor of 4.27. As expected, the μ_o values track the K'- values before and after the film is annealed. V_T is negatively shifted by 2.1V, 6.2V and 6.1V after the film is annealed at 50°C, 100°C and 150°C, respectively. After 150°C, V_T is positively shifted by ca. 7.2V. The trend in m-values roughly follows the same pattern, but it must be emphasised that within the error limits chosen for m, these values are indistinguishable and cannot yield a reliable conclusion regarding any morphological change. Similarly Ro and Rx parameters are initially reduced after the film was annealed at 50°C. However, both reductions and increases occur through the annealing range which suggests that two phase changes occur between 100°C and 150°C and between 150°C and 200°C.

Table 6.8. OTFT extracted parameters using the 5SC model for as-deposited and annealed C6PbPc - OTFT at V_{DS}=-5V.

C6PbPc					
5SC					
V_{DS}=-5V	K'	m	μ_o (cm^2 V^{-1}s^{-1})	Tc (K)	MNE (meV)
As deposited	$7.56\pm 0.78_x10^{-10}$	0.070 ± 0.02	$7.56\pm 0.54_x10^{-4}$	321.0 ± 3.2	26.2 ± 0.3
Annealed at 50	$1.50\pm 0.23_x10^{-9}$	0.089 ± 0.02	$1.50\pm 0.50_x10^{-3}$	326.7 ± 5.5	26.7 ± 0.5
Annealed at 100	$1.02\pm0.41_x10^{-8}$	0.093 ± 0.02	$1.02\pm 1.8_x10^{-2}$	327.9 ± 7.2	26.8 ± 0.6
Annealed at 150	$4.19\pm0.34_x-10^{-8}$	0.085 ± 0.02	$4.19\pm 1.8_x10^{-2}$	325.5 ± 6.7	26.6 ± 0.6
Annealed at 200	$2.39\pm0.13_x10^{-9}$	0.080 ± 0.02	$1.39\pm 0.71_x10^{-3}$	324.0 ± 7.5	26.5 ± 0.7

The m-values have already been discussed. The non-annealed C6PbPc film shows a lower K' value when compared with all the annealed C6PbPc films, and has also been discussed. The most important result is that the mobility shows almost 2 orders of magnitude increase up to 150°C, beyond which it drops by 1 order of magnitude. The K' value increased as the C6PbPc film annealed, but the K' value reduced when the film was annealed at 200°C. This variation in mobility indicates that there were changes in the phase, also suggested by the Ro and Rx progression in Table 6.7.

Results presented internally [6], have shown AFM images for a C6PbPc film for an as-deposited and annealed film at 50°C ,100°C, 150°C and 200°C. Here, it was revealed that the grain sizes had grown after the film annealed. The film morphology was improved and the number of grains reduced. After annealing at 150°c a smaller number of grain boundaries and larger grain sizes were observed. Furthermore film roughness was reduced at 150°c compared with those annealed at 50°C, 100°C, 200°C. All of these effects contribute to a reduced number of trap states and a consequent increase in mobility for the film annealed at 150°C[6].

In addition to this, according to [7] Atomic force microscopy (AFM) images of a CuPc film have a homogeneous surface with 3.878 nm roughness. In the PbPc film layer a phase transition occurs affecting the morphology as the annealing temperature increases [8]. As with thermal annealing, the initial film growth process affects the film's morphology and therefore the carrier's mobility [9].

It is also known that at certain annealing temperatures the material's mobility is reduced as a result of effects on the film's morphology where it is suggested that polymer molecules reorient themselves to become disordered causing a modified pi-pi stacking interaction [10]. This situation were occurs in our sample when annealed at 200°C the mobilise was reduced as compared with annealed at 150°C.

It is also known that as the result of thermal annealing the Q-band region in the visible absorption may become broadened and either blue shifted for ZnPc molecules [11, 12] or red shifted for $LuPc_2R_8$ [13]. This indicates that the Pc molecule is stacking face to face and edge-on- edge interaction in the ZnPc and $LuPc_2R_8$ molecules, respectively [12 ,13].

Interestingly, this is an indication of a face-to-face interaction between neighbouring C6PbPc molecules which might occurs for annealed at 150°C sample where the Pc molecules form columns which stack edge-on to the oxide surface [14]. However, the C6PbPc molecules annealed at 200°C may lose the face-to-face interaction and this may be one of the reasons the mobility is higher in the annealed case at 150°C.

It was also noted that phase transitions occur in the as-deposited film when annealed above room temperature. The film's structural features became crystalline at 102°C. The film then exhibited a discotic hexagonal columnar phase when annealed at 120°C. Further annealing of the film changed the film to an isotropic phase at 242°C. After the film cooled from 242°C and was reannealed at 92°C, the crystalline phase returned, but this time the crystalline phase was not the same as the original [13, 14, 15]. Where a molecule forms columnar axes, better charge transport is facilitated, thus enhancing a charge carrier's mobility [13, 14, and 15]. After further annealing, well-ordered disk arrangements decline whereby a C6PbPc film is no longer uniform. This leads to the formation of a discontinuous film which results in films with more grain boundaries. Energy barriers due to these grain boundaries hinder both charge transport. Hence the film's morphology is an important factor in improving a charge carrier's mobility [16].

A shuttlecock-shaped C6PbPc leads the molecules to form enough surface terraces where hole charge transfers are faster [17,18]. As a result, the as deposited C6PbPc films show better mobility, and only slightly less than for a CuPc6 film. The formation of surface terraces become more organised and the crystallinity improves greatly with annealing. As the annealed semiconductor films show larger grain sizes with high crystallinity, this leads to a better surface terrace that help increase the charge concentration. This contributes to the flow of charge and hence enhances mobility. However, beyond certain annealing temperatures, the film morphology and phase transformation can become distorted [13]. (The unsubstituted PbPc energy gap from HOMO to LUMO has been found to be 2.15eV [19]. However, an introduction of alkyl groups at substituent sites may distort the nature of the molecular structure that can reduce the energy gap. This enhances the hole carriers to hop efficiently.)

6.4 Bis-Pc complexes

6.4.1 GdPc2R16-OTFT's

The structure of GdPc2R16 is quite different from all the Pc-materials so far studied. The metal atom is bounded by two Pc rings, each Pc ring is formed by a total of eight isoindole nitrogen atoms (N-iso)[20]. This already suggests that this MPc will exist in different crystalline structures compared with its counterpart mono-MPc's see Figure 6.7. The Gd^{3+} bis-phthalocyanine complex has a face-to-face Pc arrangement with a hole delocalized over one Pc ring and shows semiconductor properties [21, 22]. Lu [23], has characterised the electronic absorption bands of bis(phthalocyaninato) complexes which are correlated with the ionic size of the central metal atom within the double-decker Pc arrangement. A blue-shift occurs when the ionic size of the central metal becomes smaller. A small electron transition moment (μ_{tm}) due to the weak absorption results in the band not shifting [23]. For a cofacial dimer the shift (ΔE) is given by $\Delta E \sim 2\mu_{tm}^2/R^3$, [24] where R is the distance of separation between the Pc units. A larger ionic radius of the central metal ion also prevents any splitting of single bands. Splitting of the lowest energy band arises from the interaction of the HOMO's of the cofacial Pc moieties [21,22]. A decrease in the Pc-Pc distance, causes a splitting of the Q band of the dimers; the intramolecular charge transfer energy is reduced. Basvova's group has characterised bis MPc molecules using UV-VIS absorption spectroscopy. Their finding shows that as-deposited films of bis MPc molecules have similar spectral features to their chloroform solutions. Both sample forms were found to absorb in the Q-band region at 704nm [25]. The molecular structure of $GdPc_2R_{16}$ studied in this thesis is believed to be similar to other double-decker Pc complexes, where the benzene rings bend outward to form a saucer- shape, making the Pc-units non-planar.

The $GdPc_2R_{16}$ sample has been tested in different OTFT devices where the device dimensions of channel width (W=10mm) and capacitance (C_i = 17.5nF/cm^2), and the semiconductor thickness are kept the same, but the channel length (L) was altered. A similar experimental procedure was used for the $GdPc_2R_{16}$-OTFT devices to measure the transfer I-V characteristics for 5μm, 10μm and 20μm channel lengths, where the gate voltage V_{GS} was swept from +30V to -40V with a 1V step interval. For transfer, V_{DS} was set at -5V and -40V for the linear and saturation regions, respectively. For output, a range of fixed V_{GS} from +10 to -20V was used for a V_{DS} sweep of 0 to -40V.
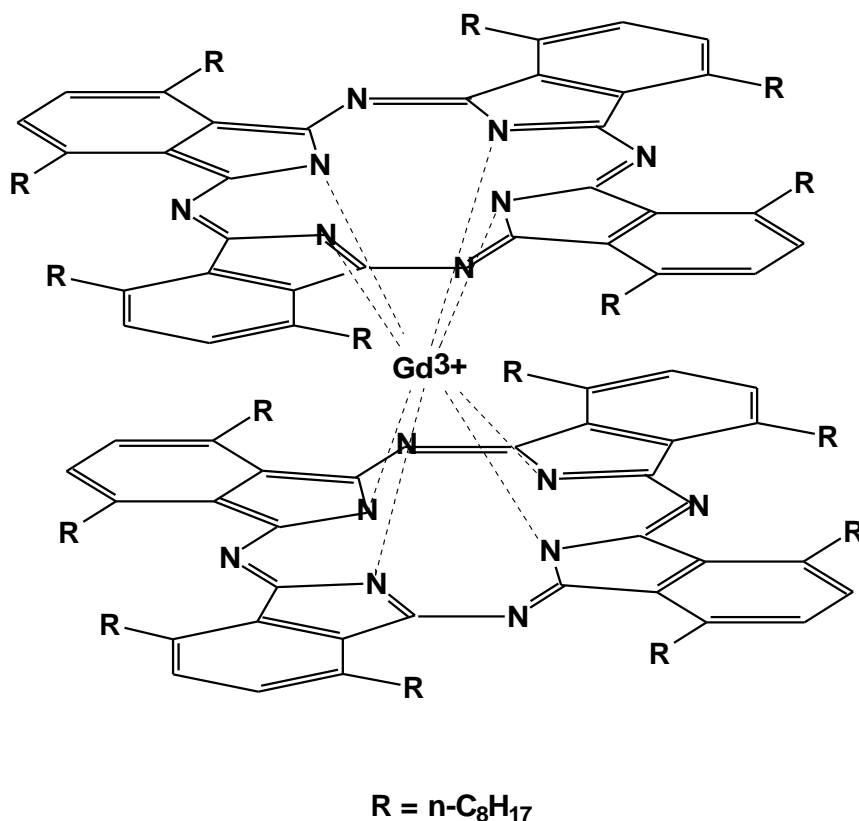
R = n-C₈H₁₇

Figure 6.7. Bis[1,4,8,11,15,18,22,25-octakis(octyl)phthalocyaninato] gadolinium (III), (GdPc$_2$R$_{16}$). File nomenclature: R$_{16}$MPc$_2$, where M= Gd, R = n-C8H17.

As mentioned before, material parameters for the semiconductor were extracted from transfer characteristics. Preliminary examination revealed that a pronounced Schottky contact effect was present, and had the reverse sense compared with the mono-Pc materials. The denominators in the expressions derived were found to be large, with the consequence that the m- and the K'- values are poorly determined directly from the transfer curve when optimised simultaneously. In the output curves, this is not the case; by assuming that the m-value is constant for the given material laid down, the m-values can be reliably obtained from an output curve for a V_{GS}-value, where the swept V_{DS} spans both the linear and saturated regions. V_{GS} values of +5V, 0V and -5V were used for 5-20 μm channel lengths examined. The m-values were found to be 0.0785±0.0040, 0.0798±0.0045 and 0.0811±0.0049 for 5μm, 10μm and 20μm channel lengths, respectively. These m-values were then used to characterise the transfer curves for GdPc$_2$R$_{16}$-OTFT. As can be seen Figure 6.8 (a and b) and the information in the Tables 6.9 and 6.10, for the extracted parameters of the channel length of 20μm, the model fits the experimental data with an error of 2.9% for the V_{DS}=-40V data. However, as a result of the increased experimental noise for 5μm and 10μm channel length for the V_{DS}=-40V data, the fitting errors are higher at 7.0% and 5.7%, respectively. For the V_{DS}=-5V data the fitting errors were found to be 2.0%, 1.5% and 4.6% for 5μm, 10μm and 20μm channel lengths, respectively. For the channel lengths 5μm and 10μm the K'-value is found to be higher for the saturation region than for the linear region. Similarly, for all channel lengths, V_T is increased in going from the linear to the saturation region.
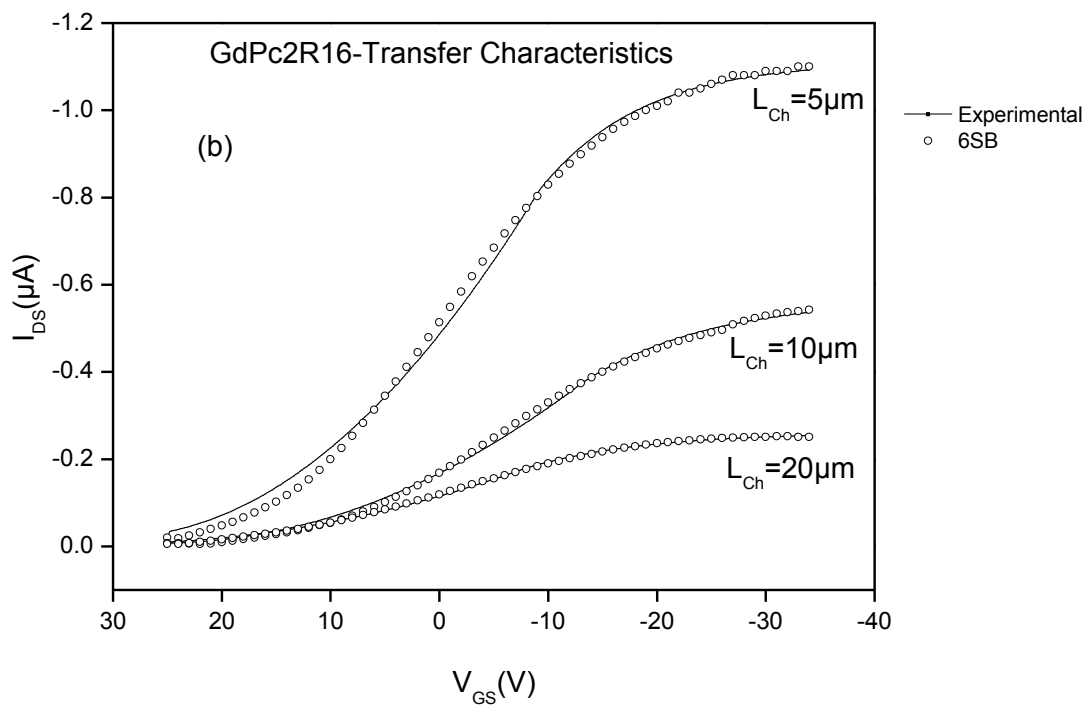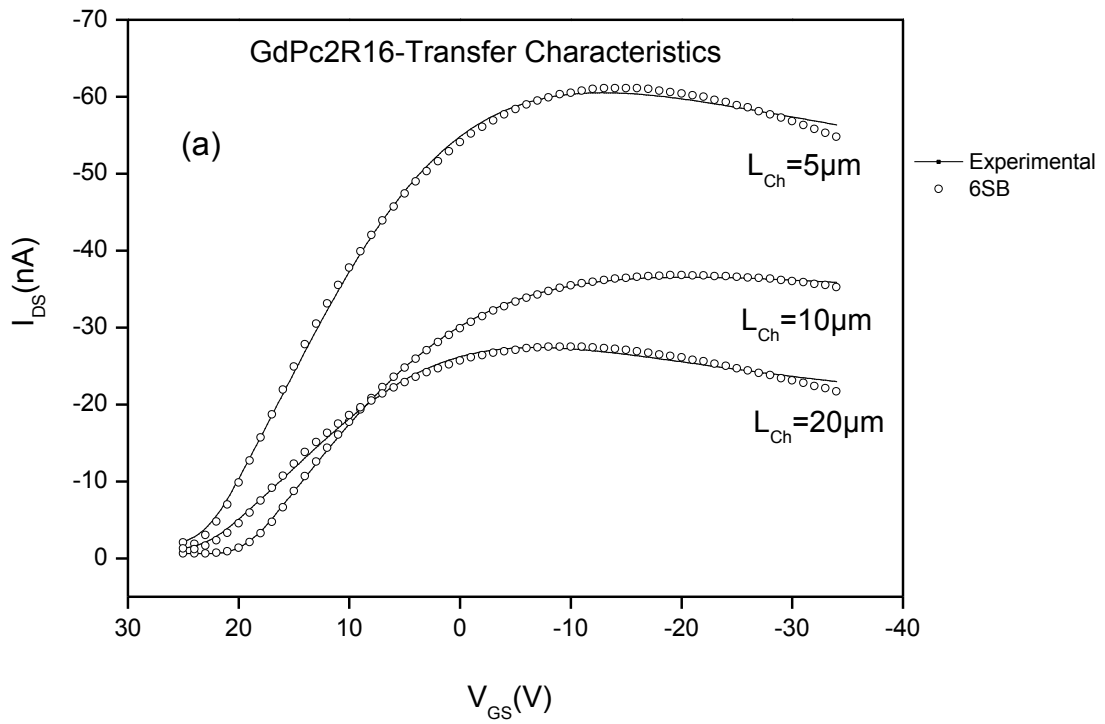
Figure 6.8. I_{DS} vs. V_{GS} transfer characteristics for GdPc$_2$R$_{16}$ with 5 µm, 10µm and 20µm channel lengths, (a) for V_{DS}= –5V and (b) for V_{DS}= -40V, experimental data (open circle), 6SB modelled data (solid line).

Table 6.9. OTFT extracted parameters for as-deposited GdPc$_2$R$_{16}$ films with 5µm, 10µm and 20µm channel lengths obtained from transfer data at V$_{DS}$=-5V and V$_{DS}$=-40V, using the 6SB (or 5SC) model.

V$_{DS}$	K'	Vt(V)	m	Ro(Ω)	Rx(Ω)	R^2	Err(%)	Rd(Ω)	Rs(Ω)
GdPc2R16									
6SB									
For L$_{ch}$=5µm									
-5V	1.88± 0.05 $_x10^{-10}$	25.9± 0.1	0.0785± 0.0040	1.21± 0.03$_x10^7$	1.54± 0.01$_x10^6$	0.9989± 0.0001	2.0±0.1	6.46± 0.01$_x10^7$	7.56± 0.16$_x10^6$
-40V	3.09± 0.10$_x10^{-10}$	30.9± 0.1	0.0785± 0.0040	3.88± 0.01$_x10^6$	3.51± 0.02$_x10^5$	0.9975± 0.0001	7.0±0.1	3.08± 0.02$_x10^7$	2.27± 0.01$_x10^6$
For L$_{ch}$=10µm									
-5V	1.29± 0.04$_x10^{-10}$	22.3± 0.1	0.0798± 0.0045	3.42± 0.06$_x10^7$	2.49± 0.01$_x10^6$	0.9997± 0.0001	1.5±0.1	9.10± 0.02$_x10^7$	1.95± 0.03$_x10^7$
-40V	1.42± 0.05$_x10^{-10}$	26.7± 0.1	0.0798± 0.0045	8.27± 0.03$_x10^6$	6.50± 0.05$_x10^5$	0.9983± 0.0001	5.7±0.1	5.30± 0.05$_x10^7$	4.78± 0.01$_x10^6$
For L$_{ch}$=20µm									
-5V	8.44± 0.27$_x10^{-11}$	25.9± 0.1	0.0811± 0.0049	9.37± 0.69$_x10^6$	3.46± 0.0$_x10^6$	0.9964± 0.0001	4.6±-0.1	1.81± 0.01$_x10^8$	8.11± 0.35$_x10^6$
-40V	6.62± 0.28$_x10^{-11}$	31.9± 0.1	0.0811± 0.0049	1.68± 0.01$_x10^7$	1.46± 0.01$_x10^6$	0.9991± 0.0001	2.9±-0.1	1.26± 0.01$_x10^8$	9.83± 0.03$_x10^6$

The m-values derived from the output data are essentially the same for all channel lengths to a high degree of consistency, as expected. The extracted parameters for the 5µm, 10µm and 20µm for GdPc$_2$R$_{16}$ are presented in Tables 6.9 and 6.10 together with a comparison of the µ$_o$, Tc and MNE values. The overall current, I$_{DS}$, is reduced as the channel length increases, and this is correlated with the K'-value. According to equation 3.2.34 the K'-value is inversely proportional to the channel length producing a stepped change in both the linear and saturation regions. In the mainly linear region, (transfer data, V$_{DS}$=-5V), K' increases by ca. 1.5x as the channel length is successively halved from 20µm to 10µm to 5µm. In the mainly saturated region (transfer data, V$_{DS}$=-40V), K' increases by ca. 2.2x as the channel length is successively halved. Theoretically, a factor of 2x is expected. Although the channel lengths form consistent sequences of K' variation, one question is as yet unresolved: for the shorter channel lengths 5µm and 10µm K' (V$_{DS}$=-5V) is greater than K' (V$_{DS}$=-40V) and consistent with the previous experience of the mono-Pc series. However, for 20 µm this is reversed, contrary to the experience so far.

Table 6.10. Key parameters and material characteristics for as-deposited $GdPc_2R_{16}$ films using the 6SB model for OTFT channel lengths of 5μm, 10μm and 20μm.

GdPc2R16					
6SP					
	K'	m	μ_o (cm^2 V^{-1}s^{-1})	T_C (K)	MNE (meV)
V_{DS}=-5V for L_{ch}=5μm	$1.88 \pm 0.05_x10^{-10}$	0.0785 ± 0.0040	$1.07 \pm 0.03_x10^{-5}$	323.5 ± 1.2	26.4 ± 0.1
V_{DS}=-40V for L_{ch}=5μm	$3.09 \pm 0.10_x10^{-10}$	0.0785 ± 0.0040	$1.76 \pm 0.06_x10^{-5}$	323.5 ± 1.2	26.4 ± 0.1
V_{DS} =-5V for L_{ch}=10μm	$1.29 \pm 0.04_x10^{-10}$	0.0798 ± 0.0045	$1.48 \pm 0.04_x10^{-5}$	323.9 ± 1.4	26.5 ± 0.2
V_{DS}=-40V for L_{ch}=10μm	$1.42 \pm 0.05_x10^{-10}$	0.0798 ± 0.0045	$1.62 \pm 0.06_x10^{-5}$	323.9 ± 1.2	26.5 ± 0.2
V_{DS} =-5V for L_{ch}=20μm	$8.44 \pm 0.27_x10^{-11}$	0.0811 ± 0.0049	$1.93 \pm 0.06_x10^{-5}$	324.3 ± 1.5	26.5 ± 0.1
V_{DS}=-40V for L_{ch}=20μm	$6.62 \pm 0.28_x10^{-11}$	0.0811 ± 0.0049	$1.51 \pm 0.06_x10^{-5}$	324.3 ± 1.5	26.5 ± 0.1

The analytical model and statistical simulations for the transfer data are expected to be reliable within the error limits adopted. It must be remembered that the errors here cited in K' arise only from the uncertainty in the determination of m. There is also an additional error of *ca.* 10-15% (see section 5.1) associated with the optimisation of parameters within a rather "flat" maximum of the multidimensional surface. When the K'-values are translated to V_G-independent mobilities, μ_o, it is found that μ_o increases with channel length for the linear region (V_{DS}=-5V), whilst this trend reverses for the saturation region (V_{DS}=-40V) where μ_o is reduced as the channel length increases. Taking the errors in K' determination into account, the V_{DS}=-40V values return rather constant values of μ_o. For the V_{DS}=-5V values, the spread is greater, lying outside the aggregated error estimate. The trend suggests that the reservoir of accumulated charge carriers produced by a given gate voltage at the smaller channel lengths is somehow decreased. In the linear region (V_{DS}=-5V), μ_o is then slightly reduced as the channel length decreases.

Consistent with the choice of a reverse-going Schottky effect for $GdPc_2R_{16}$, R_D is greater than R_S in every case. Although the parameter governing the passive contribution (R_O) is greater than that governing the active contribution (R_X) by up to an order of magnitude, a pronounced Schottky effect is evident. In both the linear and saturation regions, the parameter governing the extent of the Schottky effect, R_X, increases monotonically as the channel length increases.

The pronounced Schottky contact effect shown to be present for the $GdPc_2$ has the reverse sense compared with those mono-Pc materials where the effect was significant. This is hardly surprising: the sandwich-type $GdPc_2$ arrangement has been shown to perturb the HOMO-LUMO energies, and this effect is simply evidence that the relationship of the MPc_2 conduction band to the Au work function has changed enough to reverse the sense [26]. Although the sandwich-type a $GdPc_2$ contains a larger number of π-electrons in its macrocyclic system - and a "hole" located within it - its mobility is lower compared with that of the best mono–MPc's. It has been suggested that the degree of delocalization of the hole over the two macrocycles is reduced owing to the long-chain alkyl substitution in the double-decker Pc arrangement so that a weaker π-π interaction occurs [20]. At a coarser level, the vast periphery of n-alkyl groups will tend to dictate the molecule-to-molecule spatial separation and juxtaposition. Both these factors will contribute to a reduction in charge transfer efficiency, even when a good morphology is maintained – as suggested by the rather similar m-values for the mono- and bis-Pc complexes.

To summarise, the degree of molecular order of a film is one of the major factors that determine a carrier's mobility. In metal Pc's, the central metal atoms, length of alkyl side chains and the annealed temperature will clearly affect an OTFT device's efficiency.

References

[1] Chaure, N. B., Barard, S., Ray, A. K. et al. (2013) 'Ambipolar charge transport in non-peripherally substituted octahexyl zinc phthalocyanine' *EPL*, **104**(**5**), **57005**, doi: 10.1209/0295-5075/104/57005.

[2] Jimenez Tejada, J. A., Awawdeh, K. M., Lopez Villanueva, J. A., et al. (2011) 'Contact effects in compact models of organic thin film transistors: Application to zinc phthalocyanine-based transistors', *Org Electron*, **12** (**5**), **832**, doi: 10.1016/j.orgel.2011.02.010.

[3] Cotton, F. A. and Wilkinson, G., 'Advanced inorganic chemistry ' 5th John Wiley ,New York ,1988.

[4] Nizovtsev, A.S. and Kozlova, S.G. (2013) 'Electronic Rearrangements during the Inversion of Lead Phthalocyanine',*J. Phys. Chem. A*, **117**(**2**), **481-488**, doi: 10.1021/jp3108107.

[5] Nabok, A.V., Ray, A.K., Cook, M.J., et al. (2004) 'Lead sulphide/phthalocyanine nanocomposite spun films', *IEEE Trans. Nanotechnol.*,**3**(**3**), **388-394**,doi: 10.1109/tnano.2004.834155.

[6] N.Chaure et al, Unpublished work.

[7] Yakuphanoglu, F., Caglar, M., Caglar, Y., et al. (2010) 'Improved mobility of the copper phthalocyanine thin-film transistor',*Synth.Met.*,**160**(**13-14**), **1520**,doi: 10.1016/j.synthmet.

[8] Qiao, X., Huang, L., Chen, W, et al. (2012) 'High performance lead phthalocyanine films and its effect on the field-effect transistors', *Org Electron*, **13**(**11**), **2406**, doi: 10.1016/j.orgel.2012.06.035

[9] Ullah, M., Fishchuk, I. I., Kadashchuk, A., et al. (2010) 'Dependence of Meyer–Neldel energy on energetic disorder in organic field effect transistors', *Appl. Phys. Lett.*, **96**(**21**),**213306**, doi: 10.1063/1.3435477.

[10] Wang, T., Pearson, A. J., Dunbar, Alan D. F., et al. (2012) 'Correlating structure with function in thermally annealed PCDTBT:PC 70BM photovoltaic blends', *Adv. Funct. Mater.*, **22**(**7**), **1399**, doi: 10.1002/adfm.201102510.

[11] Chaure, N. B., Basova, T., Zahedi, M., et al. (2010) 'Solution processed tetrasubstituted zinc phthalocyanine as an active layer in organic field effect transistors', *J. Appl. Phys*,**107** (**11**) No: 114503 ,doi: 10.1063/1.3428386.

[12] Eichhorn, H., Wohrle, D., Pressner, D. (1997) 'Glasses of new 2,3,9,10,16,17,23,24-octasubstituted phthalocyanines forming thermotropic and lyotropic discotic mesophases' , *Liq.Cryst.*, **22**(**5**), **643**, doi: 10.1080/026782997209054.

[13] Basova, T., Kol'tsov, E., Hassan, A.K,et al., (2004), 'Optical investigation of thin films of liquid-crystallinelutetiumbisphthalocyanine',*J.Mater.Sci.Mater.Electron.*,**15**(**9**),**623**,doi: 10.1023/B:JMSE.0000036043.00961.be.

[14] Pouzet, E., De Cupere, V., Heintz, C., et al. (2009) 'Homeotropic Alignment of a Discotic Liquid Crystal Induced by a Sacrificial Layer', *J. Phys. Chem. C*, **113**(**32**),**14398**,doi: 10.1021/jp9035343.

[15] Chaure, N. B., Pal, C., Barard, S. et al. (2012) 'A liquid crystalline copper phthalocyanine derivative for high performance organic thin film transistors',*J. Mater. Chem.*, **22**(**36**),**19179**, doi: 10.1039/c2jm33301e.

[16] Chaure, N. B., Cammidge, A. N., Chambrier, I. et al. (2015) 'A tetrabenzotriazaporphyrin based organic thin film transistor: comparison with a device of the phthalocyanine analogue', *ECS J. Solid State Sci. Technol.*, **4**(**4**),**3086**, doi: 10.1149/2.0131504jss.

[17] Nizovtsev, A. S. and Kozlova, S. G. (2013) 'Electronic rearrangements during the Inversion of lead phthalocyanine ', *J. Phys. Chem. A*, **117**(**2**), **481**, doi: 10.1021/jp3108107.

[18] Kröger,I, Stadtmüller, B., Stadler, C., Ziroff, J., et al. (2010) 'Submonolayer growth of copper-phthalocyanine on Ag(111)', *New J. Phys.*,**12** , **083038** ,doi:10.1088/1367-2630/12/8/083038.

[19] Zhang, Y., Zhang, X., Liu, Z., Xu, H. and Jiang, J. (2006) 'Comparative density functional theory study of the structures and properties of metallophthalocyanines of group IV B ', *science direct*, **40**(**2**), **289**, doi:10.1016/j.vibspec.2005.11.004.

[20] Wang, R.M., Li, R.J., Li, Y., et al. (2006) 'Controlling the nature of mixed (phthalocyaninato) (porphyrinato) rareearth(iii) double-decker complexes the effects of nonperipheral alkoxy substitution of the phthalocyanine ligand',*Chem.Eur.J.,***12**(**5**),**1475**,doi: 10.1002/chem.200500733.

[21] Ishikawa,N., Ohno,O., Kaizu,Y., et al. (1992) 'Localized orbital study on the electronic structure of phthalocyanine dimers', *J. Phys. Chem. A.*, **96**(**22**), **8832**, doi: 10.1021/j100201a028.

[22] Korolev, V. V., Lomova,T. N.,Ramazanova, A G., et al (2016) 'Phthalocyanine-based molecular paramagnets. Effect of doubledecker structure on magnetothermal properties of gadolinium complexes',*J. Organomet. Chem.*,**819**, **209-215**, doi: 10.1016/j.jorganchem.2016.07.002.

[23] Lu, F.-Li (2007) 'The effects of substituents, molecular symmetry, ionic radius of the rare earth metal, and macrocycle on the electronic absorption spectra characteristics of sandwich-type bis(phthalocyaninato) and mixed (phthalocyaninato)(porphyrinato) rare earth complexes',**26**(**14**), **3939**, doi: 10.1016/j.poly.2007.04.017.

[24] Satake, A. and Kobuke, Y. (2007) 'Artificial photosynthetic systems: assemblies of slipped cofacial porphyrins and phthalocyanines showing strong electronic coupling', *Org. Biomol. Chem.*, **5**(**11**), **1679**,doi: 10.1039/b703405a.

[25] Mori, T. (2008) 'Molecular materials for organic field-effect transistors', *J. Phys. Condens. Matter.* ,**20**(**18**), **184010**, doi: 10.1088/0953-8984/20/18/184010.

7. CONCLUSION

Analytical models were reviewed that interpret the mechanisms of charge transport in OTFT devices. The organic-semiconductor materials of OTFT devices are more likely to be polycrystalline or amorphous. As a result, the selection of an analytical model was a primary factor in the extraction of relevant device parameters.

In the last two decades, various analytical models were proposed for OTFT devices and it was difficult to select a complete analytical model that described a given OTFT device adequately. Generally, previously proposed models were either over parameterised, or limited in the accuracy of extracting device parameters, and none provided estimates of errors.

Chapter 3 covered the different models of charge transport; it was noted that the Extended Gaussian Disorder model applied by Baesseler [1] is that currently favoured by many solid state physicists. This model applied to OTFT analyses is hampered by a number of considerations, as already discussed in chapter 3. Whilst this model may be the most realistic physical description of charge transport in disordered organic materials to date, the extraction of mobilities from experimental data to confirm its character would seem to warrant a more realistic approach, in particular handling of the contact resistances in OTFT devices. Until these now have been assumed to be purely ohmic, which ignores the mirror symmetry of the organic-metal junctions of the drain and source contacts. In this thesis, the decision has been to correct this failing using at model based on the VRH model using at most 6-parameters, where extraction relies on analytical expressions consistent with the model.

In this project, the modified analytical model has been developed from a previously proposed model used by Raja and Eccleston. It is based on a trap-and-release of charge carriers and included a charge carrier mobility that increased with gate voltage. The modified analytical model included contact resistance effects, ranging from Ohmic- to Schottky character. 4, 5 and 6-parameter versions were used, and all the parameters had a physical meaning in the OTFT description. These new analytical models were incorporated into novel statistical modelling software. Experimental data were provided by current vs. voltage (I-V) measurements for p-type OTFT devices using mono- and bis-metallophthalocyanine semiconductors. The software extracted all the device parameters simultaneously.

Luckily, the modified analytical model enabled the simulation of the entire experimental curve from both output and transfer measurements, including both above and below the threshold voltage (strong and weak inversion) regions. For the first time percentage fitting errors were estimated and these errors were on the order of 2-4% for devices with little experimental noise.

In this thesis the parameters of novel liquid crystalline mono- and bis-MPc OTFT devices were extracted. The devices of both as-deposited and annealed films of the semiconductor materials were analysed in terms of charge carrier transport mechanisms. Characterisation of the charge transport

included the effect of the Mpc central metal ion, the alkyl substituent chain length, non-aza substitution and the device's channel length.

Charge transport has been studied in both the linear and saturation regions. It has been found that both the field-independent carrier mobility (μ_o) and threshold voltage (V_T) are higher in the saturation region than in the linear region. Here, the extracted device parameters were analysed based primarily on the linear region.

According to the extracted parameters, the mobility for an as-deposited film of 6CuPc was found to be 3.91×10^{-3} cm^2 V^{-1}s^{-1}. This mobility was increased by a factor of 1.3 when a single aza-N atom is replaced by CH in the 6CuPc structure. However, the error of determination is unusually large in this case. One reason for the increased mobility could be that the morphology of the as-deposited 6Cu-TBTAP film is more ordered in this case. However, the mobility was reduced by two orders of magnitude as the alkyl chain length was increased, as in 10CuPc and 10Cu-TBTAP. Evidently, both the morphology and π-π stacking seem to have the greater impact on mobility, which is favoured for a shorter alkyl chain length allowing closer π-π stacking.

As the central metal ion changes to Zn^{2+}, the mobility was found to be reduced by three orders of magnitude. The experimental result of ZnPc samples does show increased experimental noise and the main reason for a reduction in mobility may be that the contact resistance was higher by three of magnitude compared with the 6CuPc sample.

Bulky substitution at non-peripheral positions is different from substitution at peripheral positions. The mobility increased from 2.03×10^{-6} cm^2 V^{-1}s^{-1} to 3.08×10^{-5} cm^2 V^{-1}s^{-1} as eight substituted C$_6$H$_{13}$ groups changes at non-peripheral "bay" position changed to four OCH(C$_{12}$H$_{25}$)$_2$ at peripheral positions.

Pb^{2+} has also been used as a central metal ion. The bigger metal results in a "shuttlecock" structure compared with Cu and Zn ions. The C6PbPc film mobility was found to be 7.57×10^{-4} cm^2 V^{-1}s^{-1} which is lower by a factor of 5 and the contact resistance is higher by one order of magnitude compared with 6CuPc.

Thermal annealing is expected to improve the carrier mobility because annealing forms larger and more well-ordered domains. The mobility of the peripheral-substituted ZnPc annealed film was increased by a factor of 1.71 compared with an as-deposited film. The m-value is related to the crystallinity of the film morphology, and hence mobility. A similar result was obtained for the C6PbPc annealed film where the mobility increased from 7.56×10^{-4} cm^2 V^{-1}s^{-1} C6PbPc as-deposited film to 4.19×10^{-2} cm^2 V^{-1}s^{-1} for an annealed film at 150°C. However, going beyond this annealing temperature caused a reduction of carrier mobility. However, both source and drain contact resistances were reduced even beyond the 150°C annealing point as result of improved morphology at the interface where the orientation of the π-π stacking is thought to improve.

Similarly, the bis-Mpc structure of the GdPc$_2$R$_{16}$ film was analysed for films with a 5μm, 10μm and 20μm channel length. The m-value was found to be the same which indicates that the modified

contact resistance model is quite consistent. The $GdPc_2R_{16}$ OTFT devices were prime examples for exhibiting a Schottky contact effect.

The mobility for the 5μm channel length was 1.07×10^{-5} cm^2 $V^{-1}s^{-1}$; this mobility is lower compared with that from the mono–Mpc's. It was expected that the mobility should be independent of channel length. This indeed turned out to be the case for measurements in the saturated region. However, in the linear region the mobility increased as the channel length increased. This lower mobility for shorter channel lengths may be the result of edge effects at the lower lateral fields used for the linear region. Longer channel lengths are then likely to provide more uniform conditions.

The poorest charge carrier mobility of *ca.* 3×10^{-5} cm^2 $V^{-1}s^{-1}$ was obtained from a device with an as-deposited non-peripheral ZnPc film, and the highest charge carrier mobility of *ca.* 4×10^{-2} cm^2 $V^{-1}s^{-1}$ was obtained from a device with a C6PbPc $150^{o}C$ annealed film.

From as-deposited films, non-peripheral ZnPc films showed the poorest charge carrier mobility and the highest charge carrier mobility was obtained from a device with 6Cu-TBTAP. However, the highest charge carrier mobility overall was obtained from the annealed C6PbPc film as a result of the film undergoing a molecular reorganization during the annealing process.

Finally, the mono-Mpc films show higher field-independent mobility compared with bis-Mpc films. The mobility is improved as result of non-aza group, shorter alkyl chain length and annealing the film. However, ohmic contact resistance and Schottky contact effects will affect the injection efficiency into the semiconductor layer, and thereby the performance of the OTFT device.

Future work   Imaging a molecular structure using a technique with high resolution should enable access to full physical information including the observation of a molecule's structural features. The organic semiconductor film morphology is known to be correlated with the carrier mobility, therefore the smoothness of the film needs to be analysed by a white light interferometer rather than by AFM or scanning electron microscope (SEM). White light interferometry captures an image without contacting the surface. A more accurate film layer thickness, porosity and the number of grain boundaries can be identified.

Complete information about the molecular structure of each sample has not been given. For example, how the molecular structures behave when substituting peripheral compared with non-peripheral positions. It is reasonable to expect that the molecular structures may vary as a result of the substituted alkyl chain groups.

The future may also demand the manufacturing of more OTFTs. In particular, variations in width, channel length and film layer thickness may be required. These characteristics also influence the device's efficiency and would aid research in identifying a more conductive active layer by changing the organic semiconductor.

Organic mono-phthalocyanines appear to be the most accessible organic p-type semiconductors. The immediate objective is to find out which examples from this class can be improved in their efficiency.

This will then help begin the commercial application of OTFTs rather than its currently limited use at an academic level.

Injection efficiency into the semiconductor can affect the device's performance. Gold may not be the ideal electrode choice in this respect. For example, other metals could be chosen having either larger or smaller work functions than gold, and could be used as alternative source and drain electrode materials in an OTFT device. This might improve the charge injection from the drain or source into organic semiconductor. In addition, the surface smoothness at the interface could be modified using an additional thin layer of a chosen injection material to improve the overall performance of the device.

It is not clear yet why the V_T varies under different transfer and output conditions. In this work, there is no consistency in V_T when there is a variation of V_{GS} and V_{DS} for an OTFT device.

Our novel liquid crystalline Pc's are cost-effective, processable semiconductors and usable in devices such as OTFTs. This feature aids a complete understanding of the device, linking the chemical behaviour of Pc's and the general electrical behaviour of the device. Research in institutes based on a low-economy can generate useful technical knowledge without the need for extensive funding. Although our organic phthalocyanine active materials are currently used only at an academic level, they have a potential future application if their HOMO and LUMO energies and charge transport can be manipulated to provide increased efficiency.

A future device will be favoured if it is lightweight, durable, and involves low manufacturing and material costs. Hence, future research should focus on the effect of molecular structure of Mpc on device performance. In addition to this, comparing the device's durability with- and without sample encapsulation is needed since chemical degradation of all organic materials due to light, moisture and general oxidation may reduce the longevity of devices.

For the experimental work used in this thesis, templates were used several times by cleaning and recoating. When adopting this procedure, it is very important to wash and clean the template thoroughly.

In an ideal transistor, intrinsic capacitances are ignored. However, an electric field due to intrinsic capacitance may affect the flow of current [2,3,4]. It has been proposed that a high field due to intrinsic capacitance causes the effective mobility to decrease so that an apparent hole-velocity saturation occurs [2,3]. In addition to this, non-uniform fields (fringing fields) near the source and drain edge are created, and this causes the accumulation of holes/electrons to be reduced [2,3,4]. Electrical measurement of both C-V and I-V would provide a more general characterisation of electrical behaviour, particularly with respect to frequency response. Such additional information would enable the improvement of organic semiconductor and OTFT devices for broad application.

It was mentioned that a Statistical Model was used here for the first time to fit the experimental OTFT behaviour. Unlike previous methods, only six or fewer key parameters were required, all of which were optimised simultaneously, and each of which was related to a defined physical effect. Some of

these have not previously been tackled in detail. This new software was developed without any funding; with appropriate funding this model could be improved to enable its use for industrial purposes.

References

[26] Baeseller,H. (1993) 'Charge transport in disordered organic photoconductors a Monte Carlo simulation', *Phys. Status Solidi B*, **175**(**1**),**15**-**56**, doi: 10.1002/pssb.2221750102.

[2] Castro-Carranza,A.,Estrada,M.,Nolasco,J.C.,et al. (2012) 'Organic thin-film transistor bias-dependent capacitance compact model in accumulation regime' *IET circuits devices & systems*, **6**(**2**),**130**,doi:10.1049/iet-cds.2010.0372.

 [3] Scheinert,S., Zaki, T., Roedel, R., et al. (2014) 'Numerical analysis of capacitance compact models for organic thin-film transistors',*Org. Electron.*,**15**(**7**),**1503**, doi: 10.1016/j.orgel.2014.04.013.

[4] Chung, S.S.S. (1989) 'A charge-based capacitance model of short-channel MOSFET's', *IEEE Trans. Comput.-Aided Des. Integr. Circuits Syst.*,**8**(**1**),**1**,doi: 10.1109/43.21813.